ISBN 82–553–1417–2
ISSN 0801–9940

No. 5
November 2003

Experimental and numerical studies of impact behaviour of GRP reinforced composite sandwich materials

by

Sigve Takle

Supervisor:
Harald Osnes, Alfred Andersen

RESEARCH REPORT IN MECHANICS

UNIVERSITY OF OSLO
DEPARTMENT OF MATHEMATICS
MECHANICS DIVISION

UNIVERSITETET I OSLO
MATEMATISK INSTITUTT
AVDELING FOR MEKANIKK

Experimental and numerical studies of impact behaviour of GFR reinforced composite sandwich materials

Sigve Takle

Supervisor: Haral Osnes , Alfred Andersen

Preface

This thesis is written for the degree Candidatus Scientiarum at the University of Oslo, Mechanics division.

The work is conducted at Sintef in Oslo, at Department of Polymers and Composites. I would like to thank Sintef Materials Technologies for making testing equipment available and ABB Offshore Systems for providing the sandwich specimen. Special thanks to cand. scient. Reidar Friberg for help with the testing equipment and technical discussions. I would also like to thank siv. ing. Rune Gaarder, for providing relevant literature and technical discussions.

The testing part of this thesis is conducted in company with another student, Nils Arne Rakstad, who studie low-velocity impacts onto GRP-laminates. I would like to thank Nils Arne for good cooperation and many constructive discussions throughout the thesis.

I would also like to thank my external teaching supervisor cand. scient. Alfred Andersen, for good guidance throughout the thesis, and my internal teaching supervisor assistant professor Harald Osnes, for good guidance in the final stages of the writing process.

Oslo, 14th November 2003.

Abstract

This thesis consists mainly of two parts; a testing part and a simulation part. Three different tests are performed: *four point bending, static deflection* and *drop weight impact tests.*

The four point bending test is a fast and simple test where a simply supported sandwich beam is loaded at two points. Material properties in the facings and core can be found along with the ultimate stresses in the materials. In the static deflection test, a sandwich plate lying on a quadratic frame is loaded at the centre. Here, the deflection of the plate and the applied load are logged. The data retrieved from this test are then compared with static simulations. In the drop weight tests, sandwich plates are impacted with a projectile. The acceleration of the projectile is logged during the impact. These data reveal much about how the plates respond to the impact. All specimen in the tests are equipped with strain gauges on the facings. They provide strain information during the tests.

The static deflection test is modelled with both an analytical model and ANSYS. Various ANSYS elements have been used, and their restrictions when modelling sandwiches have been investigated. Good agreement between test and simulations have been established. Also, ANSYS has a shell element which uses the same assumptions as our analytical model, and the two models show the very same centre deflection.

The drop weight impact is simulated with AUTODYN. From the acceleration data found in the test, kinetic energy and deflection of the projectile were calculated and are compared with the simulations. The AUTODYN software manage to simulate the impacts very accurately.

List of Symbols

Next comes a list of the notation and symbols used in the text. Symbols not mentioned here are defined where they appear.

Latin symbol	**Description**	**Unit**
D	Flexural rigidity (bending stiffness)	Nmm
$D_0,\ D_f,\ D_c$	Flexural rigidity of components in a sandwich	Nmm
E	Young‘s modulus	N/mm^2 (MPa)
G	Shear Modulus	N/mm^2 (MPa)
M	Bending moment	Nmm
F	Force	N/mm
S	Shear stiffness	N/mm
Q	Transverse force	N/mm
J	Joule	Nmm
$a,\ b$	Sides of sandwich plate	mm
t	Thickness	mm
d	Distance between centroids of the faces	mm
q	Pressure load	N/mm^2 (MPa)
$u,\ v,\ w$	Deformation components in x, y and z-directions	mm
$x,\ y,\ z$	Cartesian coordinate system	mm
$w_b,\ w_s$	Deformation due to bending and shear, respectively	mm

Greek symbol	**Description**	**Unit**
Φ	Spatial displacement function	mm
ϵ	Strain	-
κ	Curvature	mm^{-1}
γ	Transverse shear stiffness	-
γ_0	In-plane shear strain	-
ν	Poisson‘s ration	-
θ	Shear factor	-
ρ	Density	kg/m^3
ρ	Mass per unit surface area	kg/m^2
σ	Direct stress	N/mm^2 (MPa)
τ	Shear stress	N/mm^2 (MPa)

Subscript	**Description**
x,y,z	Cartesian coordinates
1,2,3	Cartesian coordinates
c	Core
f	Face
b	Pure bending
s	Pure shear

Operators	**Description**
d/dx_i	Ordinary differential with respect to variable x_i
$\partial/\partial x_i$	Partial differential with respect to variable x_i
Δ	Laplace operator

Contents

List of Figures

List of Tables

Chapter 1

Introduction

1.1 The concept of Sandwich constructions

Several different suggestions on how sandwiches got their name have been introduced in the literature. One is that John Montagu (1718-1792), 4th Earl of Sandwich asked for bread, cheese and meat to be brought to the table where he was gambling. He held the food with one hand, bread outside and the other ingredients inside while continuing gambling, whereas the other players said to request "the same as Sandwich". A typical sandwich consists of two slices of bread with meat in between, while the sandwich materials discussed in this thesis consist of two thin sheets of glass fibre reinforced plastics (GRP) laminates filled with a low-density material. The American society for testing and materials (ASTM) defines a sandwich structure as follows:

> *A structural sandwich is a special form of a laminated composite comprising of a combination of different materials that are bounded to each other so as to utilize the properties of each separate component to the structural advantage of the whole assembly.*

Historically, the concept of using faces separated by a distance was first discussed in the 1820s by a Frenchman. About 100 years later the concept was first applied commercially. Prior to World War Two some use was made of sandwich panels in small planes, but the World War II Mosquito bomber, designed and built by Haviland Airplane Company is often quoted as the first structure to incorporate sandwich panels. A picture of the plane is shown in Fig. 1.1 The excellent performance demonstrated by this airplane had convinced numerous aircraft designers of the superiority of sandwich structure as a mean to construct more efficient airplanes. The structural efficiency of the concept was now generally accepted.

The process of developing core materials has continued until today to reduce the weight of sandwich panels. Honeycomb core materials, developed primarily for the aerospace industry, began in the late 1940s. Honeycomb cores still provide the highest shear strength and stiffness to weight ratios. However, great care is required in ensuring adequate bonding to the faces. Generally, a hexagonal cell shape as illustrated in Fig. 1.2 is used. Due to high cost, the honeycomb cores are predominantly used in the aerospace industry.

Plastic polyvinyl chloride (PVC) foams was developed in Germany in the early 1940s, but was first commercially used 15 years later. A PVC foam core is used in

Figure 1.1: A Mosquito Bomber from World War Two. Known as the first mass produced airplane using sandwich panels.

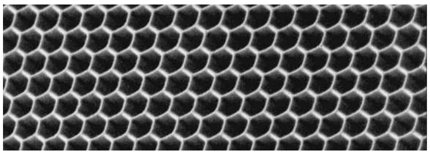

Figure 1.2: Hexagonal honeycomb core material.

the sandwich plates studied in this thesis.

Theoretical analysis of sandwich constructions began after the World War Two on the strength and stability of sandwiches. Significant early works by Reissner [18], Libove and Batdorf [13], Hoff [11] and Mindlin [14] form the basis of two important texts on sandwich constructions published in the 1960s by Plantema [17] and Allen [2]. Most of the sandwich theory presented in this thesis is found in the book *An Introduction to Sandwich Constructions* [24] written by Dan Zenkert. This book summarizes the results of research up till today, and the theory is presented in a unified manner, with coherent system of notation.

For the last twenty years, the finite element method has become the main design tool for panel analysis. Sandwich design problems are usually more accurately analysed by the finite element method than by traditional analytical theories. As a result, little effort has been made on theoretical analysis of sandwich panels. For the last two decades impact resistance, fatigue and fracture have been the main focus of research work on sandwich panels.

One of the best examples on modern sandwich technology is the Visby Corvette shown in Fig. 1.3. This corvette is built with composites and sandwiches using carbon fibre reinforced plastics (CRP) facings.

A sandwich can be compared to an I-beam. The I-beam uses as much as possible of the material in the flanges. Only a sufficient amount of material is left in the connection web to make the flanges work together and to resist shear and buckling. In a sandwich the faces take the place of the flanges and the core takes the place of the web. The faces will act together to form an efficient stress couple counteracting the external bending moment. The core resists the shear and stabilizes the faces against buckling or wrinkling.

Advantages given by the sandwich concept may be summarized as: high stiffness and strength to weight ratios, thermal and acoustic insulation, high energy absorption

Figure 1.3: A Visby stealth corvette. The hull material is a sandwich construction comprising a PVC core with a carbon fibre and vinyl laminate.

capability. Main drawbacks are: production methods, complicated quality control, lack of knowledge on the effect of damage, difficult to repair. However, due to the research and development on these subjects, the difficulties are reduced step by step.

1.2 Specification of the problem

As mentioned above, one of the main area of research on sandwiches has been impact resistance. Due to the brittle behaviour of GRP materials, the facings suffer much damage. Furthermore, low velocity impacts may cause a very complicated pattern of delamination, matrix cracking and fibre failure in the facings. Also, core indentation and the bounding between the core and face are important factors when the impact response of the sandwich material is studied. Comparisons between static and dynamic tests and simulations are of special interest. Much simulation time can be saved if the dynamic impacts can be simulated using static models.

Advanced testing conducted in an instrumented drop-weight rig combined with complex numerical simulations of the behaviour will give a significant contribution to the understanding of these problems. SINTEF Materials Technology has all the necessary equipment, e.g. drop-weight rig, fast-logging desks and software, required.

1.3 Sandwich material studied

The sandwich plates studied are produced by SINTEF in cooperation with ABB Offshore Systems and they are manufactured at Brødrene Aa in Hyen. The sandwich consists of an H-80 core manufactured by Divinycell [10] and $[0,90]_s$ GRP-facings, and it was cut into 4 rectangular plates and two beams according to Fig. 1.4.

1.4 Chapter overview

This thesis is organized as follows:
Chapter 1 gives a brief historical introduction to the sandwich concept. Also, advantages and disadvantages, areas of research and applications where sandwich materials are used are presented. Chapter 2 provides a summary of sandwich theory, and the various simplifications that need to be made, whereas the analytical solutions to

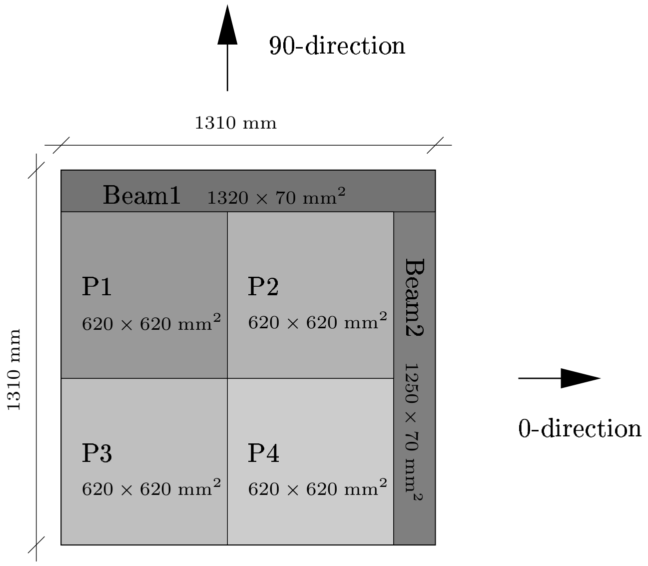

Figure 1.4: One large sandwich plate was cut into smaller parts as shown in the figure.

beams and plates are offered by the chapters 3 and 4, respectively. Chapter 5 describes the various tests conducted. Also the testing equipment used, is presented. In the Chapter 6, 7 and 8, the tests are simulated and the results are compared. Chapter 8 contain comparisons between the static and dynamic plate tests. A summary of the thesis is given along with a conclusion and suggestions to further work in Chapter 9.

Chapter 2

Sandwich theory

2.1 Introduction

Materials consisting of two faces separated by a core is called sandwich materials. The advantages of sandwich materials was first appreciated by aerospace industry, who needed light, strong and stiff materials in their planes. Today sandwich panels are being used in a wide range of structures. The sandwich panels in this thesis consist of Glass Fibre Reinforced Plastic faces and PVC foam cores. Theoretical analysis of sandwich panels are complicated, and some simplifications need to be made. It is virtually the same as engineering beam theory, but now one must account for transverse shear deformations. Another novelty is that different loads will be carried by different parts of the structure.

The theory presented in this section is a brief summary of the work done by Allen [2] and Plantema [17] and is found in [24].

2.2 Flexural Rigidity

A well known problem is a straight beam subjected to a constant bending moment giving the beam a curvature κ_x (inverse of radius of curvature) according to Fig. 2.1. The strain in a fibre situated a distance z from the neutral axis is now

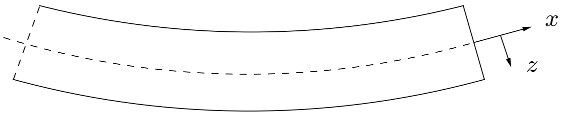

Figure 2.1: A beam subjected to a bending moment.

$$\epsilon_x = \kappa_x z \tag{2.1}$$

ie, linearly varying with z. The applied moment per. unit width may be expressed by

$$M = \int \sigma_x z dz = \int \frac{Ez^2}{R_x} dz, \text{ where } EI = \int Ez^2 dz = D. \tag{2.2}$$

EI is the *flexural rigidity*, from now on denoted D for the following reason: if Young‘s modulus E varies along the z-coordinate then it can not be removed outside the integral in Eq. (2.2), and the definition of the moment of inertia will be lost. Therefore, for a general cross-section, Eq. (2.2) must be used and the flexural rigidity D will be the only property well defined. The general expression for the strain will then be

$$\epsilon_x = \frac{Mz}{D} \tag{2.3}$$

Assuming small deflection theory, the radius of curvature is found to be

$$\frac{1}{R_x} = \frac{d^2w}{dx^2}, \tag{2.4}$$

where w is the displacement along the z-axis. The coordinate system and positive directions are shown in Fig.2.2.

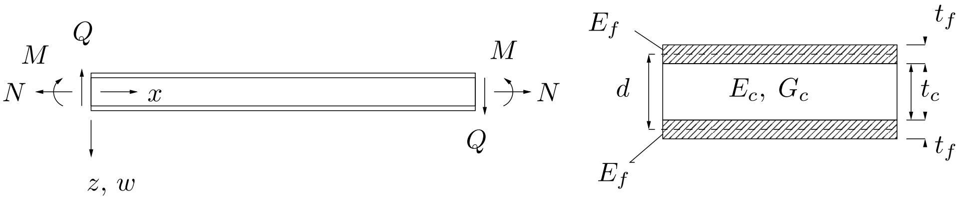

Figure 2.2: Sign convention for sandwich beams

Assuming

- symmetric layup
- faces have the same thickness t_f and are of the same material E_f
- core has thickness t_c and modulus E_c,

the flexural rigidity D per unit width of a cross-section as shown in Fig. 2.2 is then

$$D = \int Ez^2dz = \frac{E_f t_f^3}{6} + \frac{E_f t_f d^2}{2} + \frac{E_c t_c^3}{12} = 2D_f + D_0 + D_c \tag{2.5}$$

where $d = t_f + t_c$ is the distance between the centroids of the faces. The first term of (2.5) corresponds to the flexural rigidity of the faces alone when bending about their individual neutral axes, the second represents the stiffness of the faces associated with bending about the centroidal axis of the entire sandwich and the third term is the flexural rigidity of the core.

2.3 Approximations in the Flexural Rigidity

The faces are usually thin compared with the core, and the first term of Eq. (2.5) is therefore quite small and is less than one percent of the second if

$$3\left(\frac{d}{t_f}\right)^2 > 100 \text{ or } \frac{d}{t_f} > 5.77. \tag{2.6}$$

As a result of materials selection, the core usually has a much lower modulus than the face. Hence, the third term is less than one percent of the second if

$$\frac{6E_f t_f d^2}{E_c t_c^2} > 100. \tag{2.7}$$

Thus, for a sandwich with thin faces, $t_f << t_c$, and a weak core, $E_c << E_f$, the flexural rigidity can be approximated as

$$D = \frac{E_f t_f d^2}{2}. \tag{2.8}$$

For ordinary engineering materials used in sandwich structures, the core/face thickness ratio is commonly 10 to 50 and the face/core modulus ratio between 50 and 1000. It is important to notice that the dominating term in the expression for the flexural rigidity is that of the faces bending about the neutral axis of the entire sandwich. This part is the one originating from a direct tension-compression of the faces, and is called the *sandwich effect.*

The sandwich panels used in this thesis have core/face thickness ratio $25/3 = 8.3$ and face/core modulus ratio $31500/80 = 394$. Our material properties also fulfill the approximation limits in Eqs. (2.6) and (2.7),

$$\begin{aligned} \frac{d}{t_f} &= 28/3 = 9.33 > 5.77 \\ \frac{6E_f t_f d^2}{E_c t_c^2} &= \frac{6 \times 31500 \times 3 \times 28^2}{80 \times 25^2} = 8891 > 100. \end{aligned}$$

Therefore the error will be less than one percent when using the approximations in flexural rigidity.

2.4 Stresses in the Sandwich Beam

From Eq. (2.3), the stresses due to bending are readily found. The face and core stresses are

$$\sigma_f = \frac{MzE_f}{D} \text{ for } \frac{t_c}{2} < |z| < \frac{t_c}{2} + t_f, \qquad \sigma_c = \frac{MzE_c}{D} \text{ for } |z| < \frac{t_c}{2}. \tag{2.9}$$

Hence, the stresses vary linearly within each material, but there is a jump in the stress at the face/core interface.

In the same manner as above, a general definition can also be found for the shear stress. Consider an element dx of a beam as shown in Fig. 2.3. The shear force must balance the change in the direct stress field

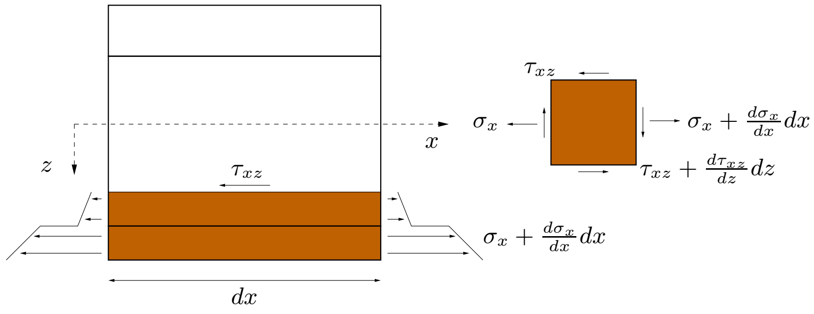

Figure 2.3: Beam section dx defining equilibrium for a sub-area.

$$\frac{d\sigma_x}{dx} + \frac{d\tau_{xz}}{dz} = 0 \Longrightarrow \tau_{xz} = \int_z^{(d+t_f)/2} \frac{d\sigma_x}{dx} dz \tag{2.10}$$

when using that $\tau_{xz}((d+t_f)/2) = 0$. Now, using Eq. (2.9) and $dM/dx = Q$ we get

$$\tau_{xz} = \frac{Q}{D} \int_z^{(d+t_f)/2} Ezdz = \frac{QB(z)}{D} \tag{2.11}$$

where $B(z)$ is the *first moment of area.* In the core material for $|z| \leq t_c/2$ the first moment of area is

$$B(z) = \frac{E_f t_f d}{2} + \frac{E_c}{2}\left(\frac{t_c}{2} - z\right)\left(\frac{t_c}{2} + z\right) \tag{2.12}$$

yielding the shear stress in the core

$$\tau_c(z) = \frac{Q}{D}\left[\frac{E_f t_f d}{2} + \frac{E_c}{2}\left(\frac{t_c^2}{2} - z^2\right)\right] \tag{2.13}$$

and similarly in the faces for $t_c/2 \leq |z| \leq t_c/2 + t_f$

$$B(z) = \frac{E_c}{2}\left(\frac{t_c}{2} + t_f - z\right)\left(\frac{t_c}{2} + t_f + z\right) \Longrightarrow \tau_f(z) = \frac{Q}{D}\frac{E_f}{2}\left(\frac{t_c^2}{4} + t_c t_f + t_f^2 - z^2\right). \tag{2.14}$$

The maximum shear stress appears at the neutral axis, i.e. for $z = 0$

$$\tau_{c,max} = \tau_c(z=0) = \frac{Q}{D}\left(\frac{E_f t_f d}{2} + \frac{E_c t_c^2}{8}\right) \tag{2.15}$$

and the shear stress in the core/face interface becomes

$$\tau_{c,min} = \tau_{f,max} = \frac{Q}{D}\left(\frac{E_f t_f d}{2}\right). \tag{2.16}$$

From Eq. (2.14) it is seen that the shear stress in the outer fibre of the faces is zero which must be the case for a free surface.

2.5 Approximations in the Shear Stress

The difference between maximum and minimum shear stress in the core is less than one percent if

$$\frac{4E_f t_f d}{E_c t_c^2} > 100. \tag{2.17}$$

Inserting for our material properties gives

$$\frac{4E_f t_f d}{E_c t_c^2} = 212 > 100.$$

The error made when assuming that the shear stress in the core equals the shear stress at the core/face interface is thus less than one percent.

2.6 Summary of approximations

Assuming weak core $E_c << E_f$, the stresses can now be written

$$\begin{aligned} \sigma_c(z) &= 0 & \sigma_f(z) &= \frac{MzE_f}{(D_0+2D_f)} \\ \tau_c(z) &= \frac{E_f t_f d}{2(D_0+2D_f)} & \tau_f(z) &= \frac{Q}{D_0+2D_f}\frac{E_f}{2}\left(\frac{t_c^2}{4}+t_ct_f+t_f^2-z^2\right). \end{aligned} \tag{2.18}$$

When the core is weak, $E_c << E_f$, and the faces are thin, $t_f << t_c$, then the formula reduces to the simplest possible form

$$\sigma_c(z) = 0,\ \sigma_f(z) = \pm\frac{M}{t_f d},\ \tau_c(z) = \frac{Q}{d},\ \text{and } \tau_f(z) = 0. \tag{2.19}$$

This simplifies the principal load carrying and stress distribution in a sandwich construction to *the faces carry bending moments as tensile and compressive stresses* and *the core carries transverse forces as shear stresses*, graphically represented in Fig. 2.4.

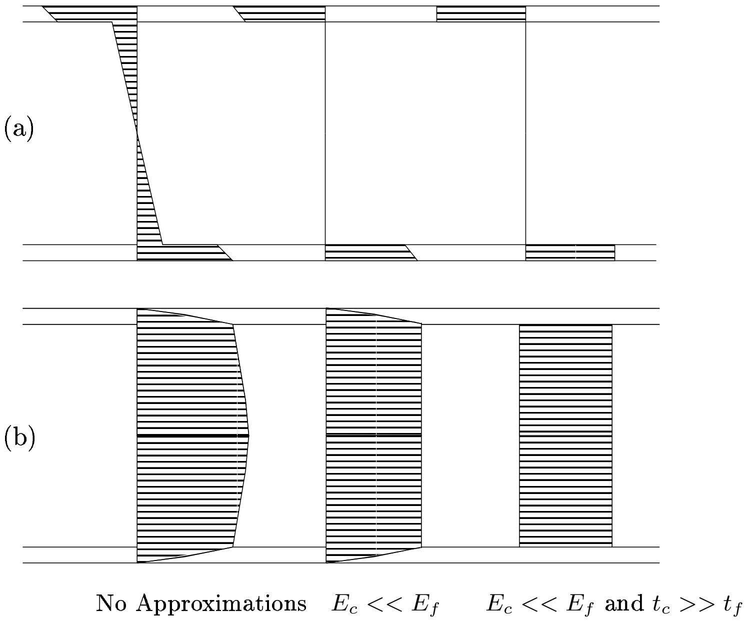

Figure 2.4: Direct (a) and shear (b) stresses for different levels of approximations.

2.7 The Sandwich Effect

Consider a homogeneous beam with a given Young‘s modulus E, and a given strength. Calculate the weight, bending stiffness and strength of the beam and set them to unity. Suppose we now cut the beam in two halves and separate the parts with a core. Calculating the corresponding stiffnesses and strengths of the sandwich beam gives the relative properties given in Fig. 2.5. Hence, by using the sandwich concept, the flexural rigidity and flexural strength can be substantially increased in comparison with a single skin structure without adding much weight.

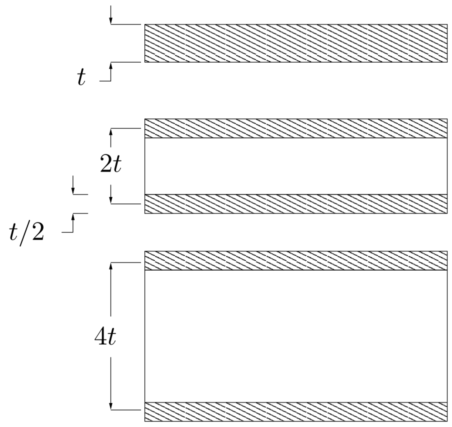

Weight	Flexural rigidity	Bending strength
1	1	1
1	12	6
1	48	12

Figure 2.5: Comparison between homogeneous and sandwich cross-sections.

2.8 Shear Stiffness and Deformations

When a structural element is subjected to shear forces it will deform without volume change. This shear force can be divided into two parts, transverse and in-plane shear force as illustrated in Fig. 2.6.

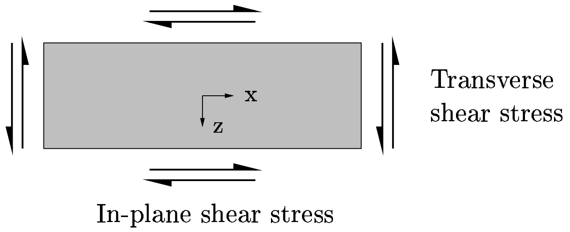

Figure 2.6: Illustration of in-plane and transverse shear forces.

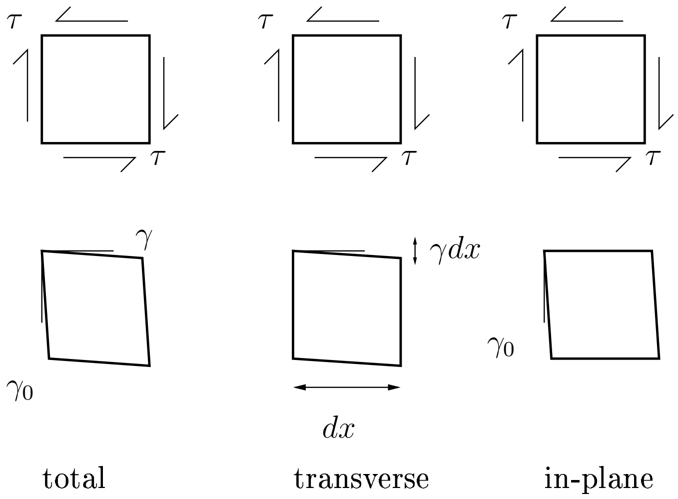

Figure 2.7: Deformations of a structural element subjected to shear forces.

The transverse deformation of an element is according to Fig. 2.7 equal to γdx. To find this, we need to perform an integration over the length of the beam, but first the shear stiffness must be known. For a general cross-section the *shear stiffness* S can be calculated by using an energy balance equation, so that the potential energy of the applied load equals the strain energy of the system. The shear stiffness S is found by calculating the average shear angle of the cross-section, $\frac{dw_s}{dx}$, where w_s is the displacement due to shear as

$$\frac{1}{2}Q\frac{dw_s}{dx} = \frac{1}{2}\int \tau_{xz}(z)\gamma_{zx}(z)dz, \text{ where by definition } \frac{dw_s}{dx} = \frac{Q}{S}. \tag{2.20}$$

Using the approximations for a sandwich with thin faces, weak core and that the shear modulus of the faces are large, it is seen that $\tau_{xz} = Q/d$ and Eq. (2.20) becomes

$$\frac{1}{2}Q\frac{dw_s}{dx} = \frac{1}{2}\int_{-t_c/2}^{t_c/2} \frac{Q}{d}\frac{Q}{G_c d}dz = \frac{Q^2 t_c}{2G_c d^2} = \frac{Q^2}{2S} \Rightarrow S = \frac{G_c d^2}{t_c}. \tag{2.21}$$

The *shear deformation*, divided into transverse and in-plane, is illustrated in Fig. 2.8. It is assumed here that the shear deformations only occur in the core($G_f = \infty$) and that this deformation is linear, $E_c << E_f$, giving a constant core shear stress and a constant shear strain. Denote the transverse shear in the core by γ and the in-plane core shear by γ_0. By studying the geometry, the following relation is found:

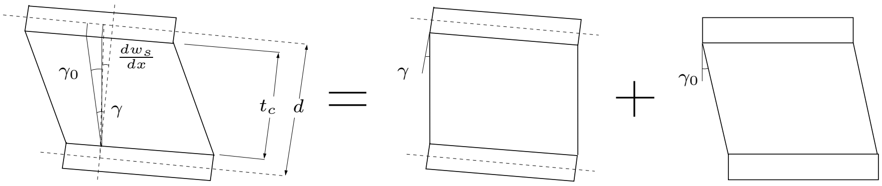

Figure 2.8: Shear deformations of a sandwich element

$$\frac{dw_s}{dx}d = (\gamma - \gamma_0)t_c \Longrightarrow \frac{dw_s}{dx} = \frac{\gamma t_c}{d} - \frac{\gamma_0 t_c}{d}.$$

And using the relations

$$S = \frac{G_c d^2}{t_c} \Rightarrow \frac{t_c}{d} = \frac{G_c d}{S}, \; \tau_c = G_c\gamma \text{ and } Q = \tau_c d$$

gives

$$\frac{dw_s}{dx} = \frac{Q}{S} - \frac{\gamma_0 t_c}{d}. \tag{2.22}$$

Chapter 3

Analytical solutions to sandwich beams

3.1 Introduction

In classical plate theory shear deformations are neglectable compared to the bending deflection. However for short beams or cross-sections with low shear stiffness this deformation must be included. This is usually called Timoshenko beam theory. The deformation consists of two parts

(i) deformation due to bending moments -bending- w_b

(ii) deformation due to transverse forces -shear- w_s

For a sandwich with thin faces the two deformation parts may be superimposed as

$$w = w_b + w_s. \tag{3.1}$$

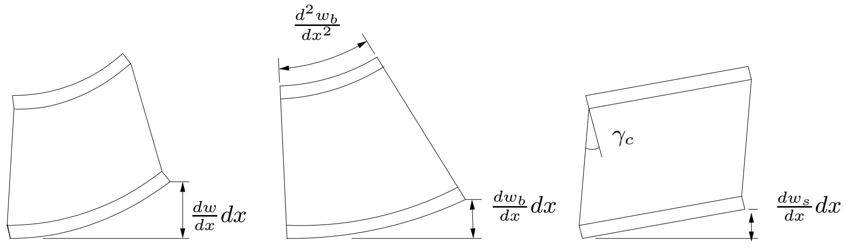

(a) (b) (c)

Figure 3.1: Total, bending and shear deformation.

3.2 Deriving the beam equation

Both Classical and Timoshenko models rest on the assumptions of small deformations and linear elastic isotropic material behaviour. In addition, both models neglect changes in dimensions of the cross sections as the beam deforms. The theory described in this section is mainly based on [24], and supplemented with information from [5]. For simplicity all beams are assumed to have unit width. The beam equation arises from four different subsets of beam theory: *the kinematic, constitutive, force resultant, and equilibrium definition equations*. Combining these parts results in the beam equation.

Kinematic equation

Kinematics describe how the beam's deflections are tracked. We need to make some assumptions on how the cross-section rotates. Classical beam theory or the engineering beam theory accounts for the effects of bending moment upon stresses and deformations. Transverse shear forces are recovered from equilibrium, but their effect on beam deformations is neglected. Its fundamental assumption is that *cross sections remain plane and normal to the deformed longitudinal axis*. This rotation occurs about a neutral axis that passes through the centroid of the cross section. The Timoshenko model corrects the classical beam theory with first-order shear deformation effects. In this theory cross sections remain plane and rotate about the same neutral axis as the classical beam theory, but do not remain normal to the deformed longitudinal axis. The deviation from normality is produced by a transverse shear that is assumed to be constant over the cross section. The *kinematic assumptions* for the in-plane and out-of-plane deformations can be written as

$$u(z) = u_0 + z\psi_x \text{ and } w = w_b + w_s, \tag{3.2}$$

where the in-plane deformation u is thus a linear function in z, and ψ_x is the cross-section rotation which only depends on the bending deformation w_b of the beam (since shear only causes sliding of the cross-section). Thus,

$$\psi_x = -\frac{dw_b}{dx}. \tag{3.3}$$

Constitutive equations

The constitutive equation describes how the direct stress σ and direct strain ϵ within the beam are related. Direct means perpendicular to a beam cross section; if we were to cut the beam at a given location, we would find a distribution of direct stress acting on the beam face. In beam theory we use the simple one-dimensional Hooke‘s equation

$$\sigma_x = E\epsilon_x. \tag{3.4}$$

The faces of our sandwich panels are thin enough to behave like membranes when shear deformation is studied. Thus any transverse shear deformation may take place without being resisted by any bending of the faces about their individual neutral axes. This is equivalent to the concept of *partial deflections*; bending causes in-plane stresses and transverse forces causes shear stresses and deformations. This study only considers stresses and strains arising from the bending moment and transverse forces of the beam, ie. $u_0 = 0$. With the assumptions from Eq. (2.19) the in-plane normal stress is obtained as

$$\sigma_f = -E_f z\frac{d^2 w_b}{dx^2} \tag{3.5}$$

and the transverse shear stress

$$\tau_c(z) = \frac{Q}{d}. \tag{3.6}$$

Force and Moment Resultants

Force resultants are a convenient mean for tracking the important stresses in a beam. If we consider a cross-section of a sandwich beam at a point x, we would find a distribution of direct stresses σ_x (a) and shear stresses τ_{xz} (b) as shown in Fig. 3.2 when the approximations from Eq. (2.19) is applied. The lower figure (c) shows the resultant forces without any approximations. Each portion of direct stress acting on the cross section creates a moment about the neutral plane ($z = 0$). Summing these individual moments over the area of the cross-section we obtain the resultant moment M, definition by

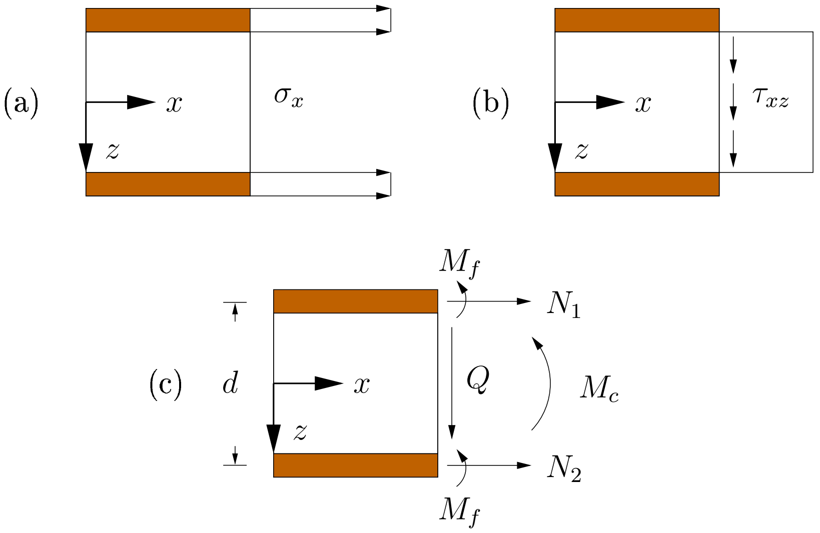

Figure 3.2: The two upper figures shows direct and shear stresses in a sandwich when thin face and soft core approximations are applied. Resultant forces without any approximations are shown in the bottom figure.

$$M = \int\int z\sigma_x dzdy, \tag{3.7}$$

where y is in the direction of the beam width. The sum of the shear stresses on the cross-section is the definition of the shear resultant Q,

$$Q = \int\int \tau_{xz} dzdy. \tag{3.8}$$

The sum of all direct stresses acting on the cross-section is denoted N,

$$N = \int\int \sigma_x dzdy. \tag{3.9}$$

The resultant force N does not play a role in linear beam theory since it does not contribute to the deflection w. The width of the beam is set to unity, so the integral

$\int 1dy$ becomes unity. From Fig. 3.2, the in-plane force in the upper and lower face can be written

$$N_1 = -\int_{t_f/2}^{t_f/2} \left[E_f(z-d/2)\frac{d^2w_b}{dx^2} \right] dz = \frac{E_f t_f d}{2}\frac{d^2w_b}{dx^2} = \frac{D_0}{d}\frac{d^2w_b}{dx^2}$$

$$N_2 = -\int_{t_f/2}^{t_f/2} \left[E_f(z+d/2)\frac{d^2w_b}{dx^2} \right] dz = -\frac{E_f t_f d}{2}\frac{d^2w_b}{dx^2} = -\frac{D_0}{d}\frac{d^2w_b}{dx^2}$$

and the moment due to the in-plane forces becomes

$$M_0 = N_1(-\frac{d}{2}) + (-N_2)\frac{d}{2} = -D_0\frac{d^2w_b}{dx^2}. \tag{3.10}$$

The resultant moment in the core is

$$M_c = -\int_{(d-t_f)/2}^{(d-t_f)/2} \left[E_c(z)\frac{d^2w_b}{dx^2} \right] dz = -\frac{E_c t_c^3}{12}\frac{d^2w_b}{dx^2} = -D_c\frac{d^2w_b}{dx^2} \tag{3.11}$$

and the faces

$$M_f = -\int_{t_f/2}^{t_f/2} \left[E_f z(z-d/2)\frac{d^2w_b}{dx^2} \right] dz = -\frac{E_f t_f^3}{12}\frac{d^2w_b}{dx^2} = -D_f\frac{d^2w_b}{dx^2}. \tag{3.12}$$

The total bending moment is hence

$$M = -(D_0 + D_f + D_c)\frac{d^2w_b}{dx^2} = -D\frac{d^2w_b}{dx^2}. \tag{3.13}$$

The response of the sandwich beam is now described by two constants; the flexural rigidity D and the shear stiffness S from Eq. (2.21),

$$D = -\frac{M}{d^2w_b/dx^2} \text{ and } S = \frac{Q}{dw_s/dx}. \tag{3.14}$$

Using (3.2), the contribution to the curvature becomes

$$\frac{d^2w}{dx^2} = -\frac{M}{D} + \frac{1}{S}\frac{dQ}{dx}. \tag{3.15}$$

Equilibrium equations

The equilibrium equations can be derived using Fig. 3.3 which shows an element dx in its distorted condition with forces acting on it in positive directions. From equilibrium of bending moments, it is found that
$dM/dx = Q$, and by using the definitions of Eq. (3.14) we find a relation between the partial deflections as

$$\frac{dw_s}{dx} = -\frac{D}{S}\frac{d^3w_b}{dx^3} \tag{3.16}$$

and from vertical equilibrium

$$q + \frac{dQ}{dx} + N\frac{d^2w}{dx^2} = 0. \tag{3.17}$$

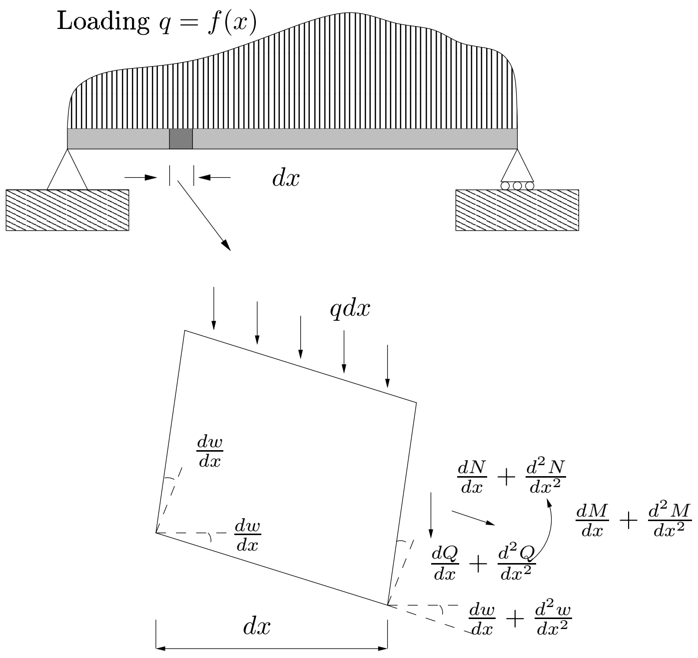

Figure 3.3: Distorted beam element.

Governing Beam Equations

Rewriting Eq. (3.17) gives

$$S\frac{d^2w_s}{dx^2} + N\frac{d^2w}{dx^2} = -q. \tag{3.18}$$

In the case of pure bending or small deformations when N is zero, an equation in w_s only is obtained. Rewriting Eq. (3.18) using Eq. (3.16) gives the governing equation in w_b

$$D + \frac{d^4w_b}{dx^4} - N\frac{d^2w}{dx^2} = q. \tag{3.19}$$

Rewriting this equation using the relation between w_s and w_b the governing equation can be written without the use of partial deflection as

$$D\frac{d^4w}{dx^4} = \left(1 - \frac{D_0}{S}\right)\left(q + N\frac{d^2w}{dx^2}\right). \tag{3.20}$$

This equation will be used to study four-point bending of sandwich beams.

3.3 Analytical solution to four-point bending (FPB)

Four-point bending tests are used to study material properties. The four-point bend specimen is schematically illustrated in Fig. 3.4 along with moment and shear force diagrams. As seen, the transverse force is constant and equal to P between the inner and outer supports. This means that the shear stress in the core is constant over a long part of the beam. Between the inner supports, over a length of L_1, the bending moment is constant and equals $P(L_2 - L_1)/2$ and the shear force is zero.

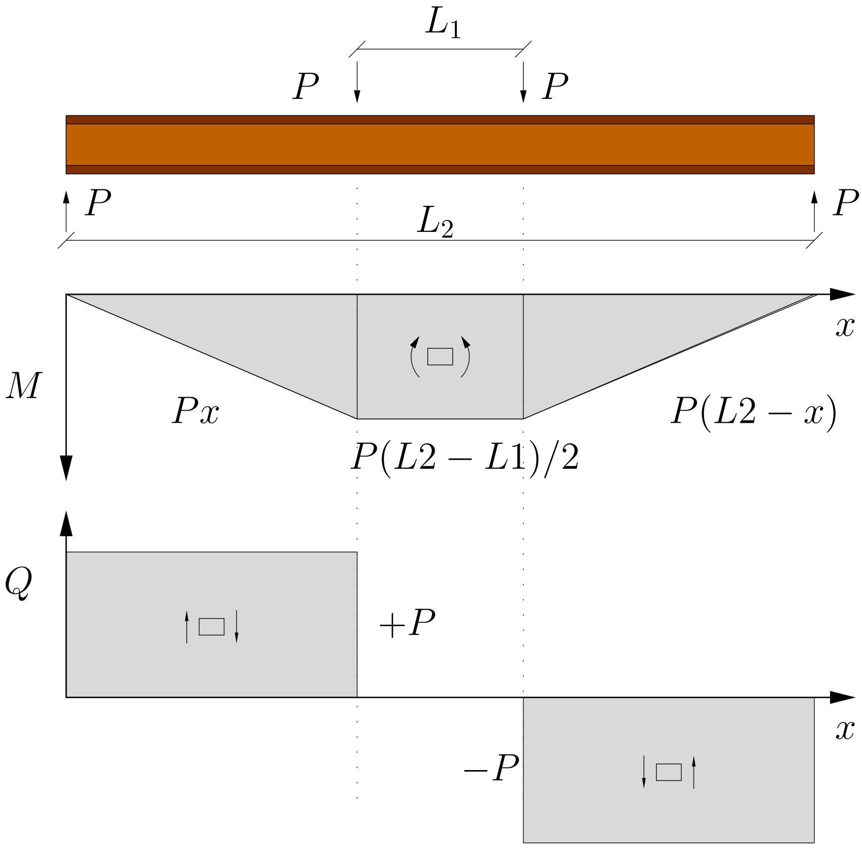

Figure 3.4: Moment and Shear diagram, P = maximum failure load

The deflection of the beam is now easily found from the sandwich theory outlined in the previous chapters.

Boundary conditions

- $w_b(0) = w_s(0) = w_b(L_2) = w_s(L_2) = 0$
- $\frac{dw_b}{dx}(L_2/2) = \frac{dw_c}{dx}(L_2/2) = 0$ symmetri conditions
- continuity at points of loading

The deflection at the points of loading is equal to the displacement of the testing machine. Solving for the bending and shear deflections by superposition one obtains

$$w(\frac{L_2 - L_1}{2}) = \frac{P(L_2 - L_1)^2(L_2 + 2L_1)}{48D} + \frac{P(L_2 - L_1)}{4S}, \tag{3.21}$$

by superposition. The maximum deflection at the centre of the beam can be written

$$w(\frac{L_2}{2}) = \frac{P(L_2 - L_1)(2L_2^2 + 2L_1L_2 - L_1^2)}{96D} + \frac{P(L_2 - L_1)}{4S}. \tag{3.22}$$

The maximum direct stress in the faces appears between the inner supports and the maximum transverse shear stress appears between the outer and inner support. The corresponding values read

$$\sigma_f = \pm\frac{M}{t_f db} = \pm\frac{P(L_2 - L_1)}{2t_f db}, \quad \text{and} \quad \tau_c = \frac{P}{db} \tag{3.23}$$

respectively, where b is the width of the beam. The fact that the transverse forces are zero and the bending forces are constant in the midsection ensures that the bending stiffness can be easily measured. The equations developed in this section will be used in Section 5.6.

Chapter 4

Analytical solutions to sandwich plates

4.1 Introduction

In the following section analytical solutions to plate bending will be developed. The theory is based on small-deformation plate bending analysis by Timoshenko and Woinowsky-Krieger [21] which is extended to account for transverse shear deformation following the work by Libove and Batdorf [13]. It is assumed that the transverse normal stiffness of the core is infinite and thus keeping the distance between the centroids of the faces, d, constant. The theory is developed for orthotropic plates with $x-$ and $y-$axis being the principal axes of orthotropy. This means that the properties of the plate are fully described by seven constants, the flexural rigidities D_x and D_y, the twisting stiffness D_{xy}, the Poisson‘s ratios ν_{yx} and ν_{xy}, and the shear stiffnesses S_x and S_y. An isotropic solution is also found by simplifying the orthortopic solution.

The coordinate system and the positive directions are defined in Fig. 4.1. It is assumed that the shear strain is constant over the cross-section (thin-face approximation) so the in-plane deformations for the classic Reissner/Mindlin kinematics can be used. These are

$$u = u_0 + x_x\psi_x, \;\; v = v_0 + z_y\psi_y \text{ and } w = w_0, \tag{4.1}$$

where subscript 0 refers to the middle plane. ψ_x and ψ_y are defined as the *cross-section rotations* in the $x-$ and $y-$directions, respectively. Assuming strains to be much smaller than unity, the strain-displacement relations are defined as

$$\epsilon_x = \frac{\partial u}{\partial x}, \;\; \epsilon_y = \frac{\partial v}{\partial y} \text{ and } \gamma_{xy} = \frac{\partial u}{\partial y} + \frac{\partial v}{\partial x}, \tag{4.2}$$

for strains much smaller than unity.

4.2 Deriving the plate equation

4.2.1 Governing equations

The bending moments and transverse forces can be written as functions of the displacement field w. The curvatures κ_x and κ_y (inverse of the radius of curvature) and

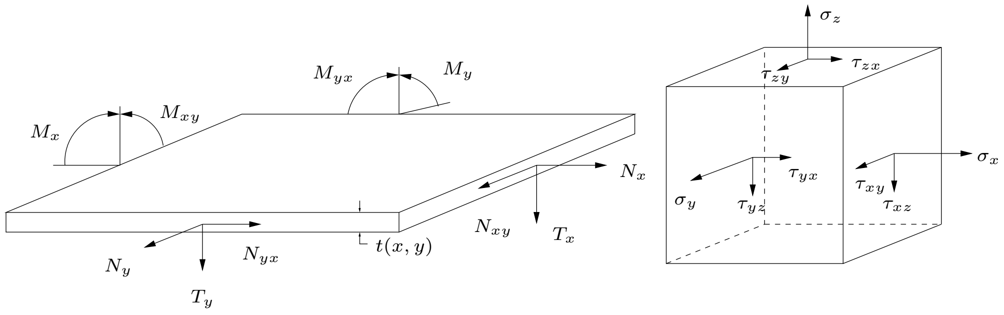

Figure 4.1: Sign convention used in plate analysis

κ_{xy} can be written

$$\kappa_x = -\frac{\partial^2 w}{\partial x^2}, \quad \kappa_y = -\frac{\partial^2 w}{\partial y^2} \text{ and } \kappa_{xy} = -\frac{\partial^2 w}{\partial x \partial y}. \tag{4.3}$$

The component κ_{xy} is a twisting curvature, stating how the x-direction midplane slope changes with y (or equivalently how the y-direction slope changes with x). The Poisson‘s ratios may be expressed by

$$\nu_{xy} = -\frac{\partial^2 w/\partial y^2}{\partial^2 w/\partial x^2} \text{ and } \nu_{yx} = -\frac{\partial^2 w/\partial x^2}{\partial^2 w/\partial y^2}. \tag{4.4}$$

Assuming that only a single load is allowed to act on the plate at a time, the plate equations can be derived by collecting the contributions from each load. This leads to the following equations for the curvatures

$$\frac{\partial^2 w}{\partial x^2} = -\frac{M_y}{D_x} + \nu_{yx}\frac{M_y}{D_y} + \frac{1}{S_x}\frac{\partial Q_x}{\partial x} \tag{4.5}$$

$$\frac{\partial^2 w}{\partial y^2} = -\frac{M_x}{D_y} + \nu_{xy}\frac{M_x}{D_x} + \frac{1}{S_y}\frac{\partial Q_y}{\partial y} \tag{4.6}$$

$$\frac{\partial^2 w}{\partial x \partial y} = -\frac{M_{xy}}{D_{xy}} + \frac{1}{2S_x}\frac{\partial Q_x}{\partial y} + \frac{1}{2S_y}\frac{\partial Q_y}{\partial x}. \tag{4.7}$$

Next, equilibrium equations are defined by studying Fig. 4.2, assuming an increment change in all forces and bending moments over the differential element. and By projecting all forces onto the $z-$axis, the vertical equilibrium is found. As seen in Fig 4.3, the projection of the normal force N_x onto the z-axis gives

$$-N_x\frac{\partial w}{\partial x}dy + (N_x + \frac{\partial N_x}{\partial x}dx)dy(\frac{\partial w}{\partial x} + \frac{\partial^2 w}{\partial x^2}dx) \tag{4.8}$$

and the projection of the shear force N_{xy} is similarly

$$-N_{yx}\frac{\partial w}{\partial x}dx + (N_{yx} + \frac{\partial N_{yx}}{\partial y}dy)dx(\frac{\partial w}{\partial x} + \frac{\partial^2 w}{\partial x \partial y}dx). \tag{4.9}$$

By including the rest of the terms and omitting higher order terms in dx and dy one arrives at

$$\frac{\partial Q_x}{\partial x} + \frac{\partial Q_y}{\partial y} + q + N_x\frac{\partial^2 w}{\partial x^2} + N_y\frac{\partial^2 w}{\partial y^2} + N_{xy}\frac{\partial^2 w}{\partial x \partial y} + N_{yx}\frac{\partial^2 w}{\partial x \partial y} = 0. \tag{4.10}$$

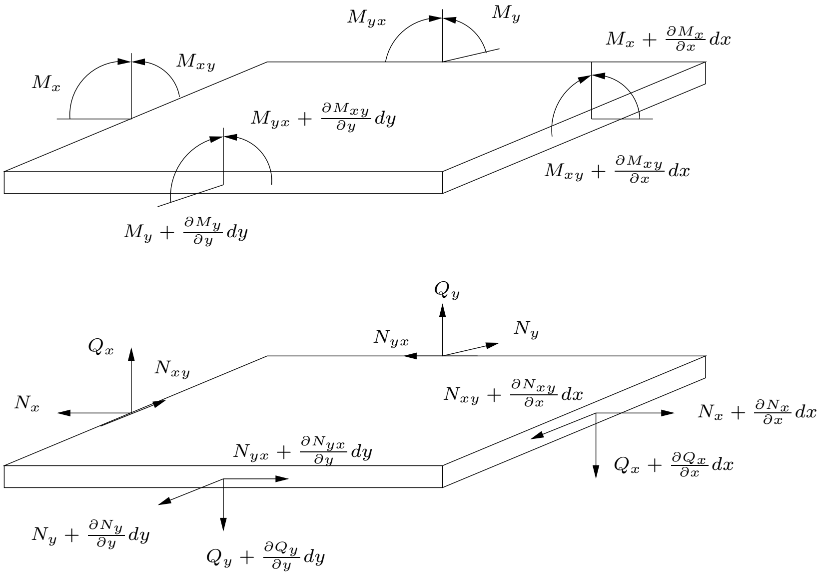

Figure 4.2: Bending moments and forces acting on a differential element.

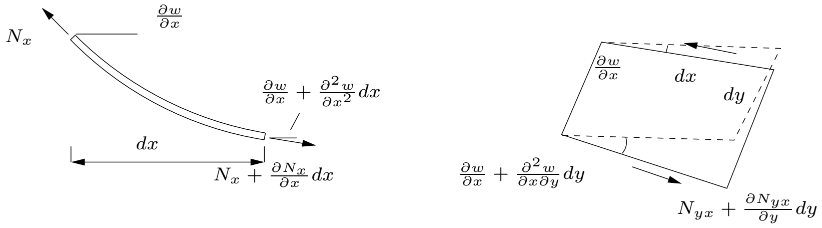

Figure 4.3: Force projections.

From equilibrium of the bending moments about the x-, y- and z-axes the following equations are obtained

$$Q_x - \frac{\partial M_x}{\partial x} - \frac{\partial M_{xy}}{\partial y} = 0 \tag{4.11}$$

$$Q_y - \frac{\partial M_y}{\partial y} - \frac{\partial M_{xy}}{\partial x} = 0 \tag{4.12}$$

$$N_{xy} = N_{yx}. \tag{4.13}$$

Here we have applied the relation $M_{yx}{=}M_{xy}$ since $\tau_{xy} = \tau_{yx}$.

By assuming that the normal forces N are constant throughout the plate and that they do not change as the plate bends the analysis is restricted to small deformations. Inverting the relations above the following expression for the bending moments arise

$$M_x = -\tfrac{D_x}{1-\nu_{xy}\nu_{yx}} \left[\frac{\partial}{\partial x} \left(\frac{\partial w}{\partial x} - \frac{Q_x}{S_x} \right) + \nu_{yx} \frac{\partial}{\partial y} \left(\frac{\partial w}{\partial y} - \frac{Q_y}{S_y} \right) \right] \tag{4.14}$$

$$M_y = -\tfrac{D_y}{1-\nu_{xy}\nu_{yx}} \left[\frac{\partial}{\partial y} \left(\frac{\partial w}{\partial y} - \frac{Q_y}{S_y} \right) + \nu_{xy} \frac{\partial}{\partial x} \left(\frac{\partial w}{\partial x} - \frac{Q_x}{S_x} \right) \right] \tag{4.15}$$

$$M_{xy} = -\tfrac{D_{xy}}{2} \left[\frac{\partial}{\partial x} \left(\frac{\partial w}{\partial y} - \frac{Q_y}{S_y} \right) + \frac{\partial}{\partial y} \left(\frac{\partial w}{\partial x} - \frac{Q_x}{S_x} \right) \right]. \tag{4.16}$$

Now we have six fundamental equations to determine the deflection field, the forces and the bending moments. It might be more convenient to rewrite these equations to obtain equations in one single variable, ie. for the deflection only as a function of the applied loads. Thus, by rearranging Eq. (4.10), one obtains

$$\frac{\partial^2 M_x}{\partial x^2} + 2\frac{\partial^2 M_{xy}}{\partial x \partial y} + \frac{\partial^2 M_y}{\partial y^2} = \frac{\partial Q_x}{\partial x} + \frac{\partial Q_y}{\partial y} = -q^* \tag{4.17}$$

with

$$q^* = q + N_x \frac{\partial^2 w}{\partial x^2} + 2N_{xy}\frac{\partial^2 w}{\partial x \partial y} + N_y \frac{\partial^2 w}{\partial y^2}. \tag{4.18}$$

4.2.2 Partial deflections

Partial deflections due to bending and shear are introduced by assuming only one mode of deformations at a time, and that we can separate the displacement fields due to bending w_b, and transverse shear w_s. The total deflection is then found by superimposing these contributions. We also introduce a specific relation between the transverse forces and the shear part of the deformations as

$$w = w_b + w_s, \; Q_x = S_x \frac{\partial w_s}{\partial x}, \; \text{ and } \; Q_y = S_y \frac{\partial w_s}{\partial y}. \tag{4.19}$$

The two field variables Q_x and Q_y have now become linked to a single variable w_s, and this is in essence the simplification. It also means that the bending moments will be independent of the transverse force field and vice versa. This assumption will only be correct for isotropic plates but will be a very good approximation for plates that have equal rigidities in both x- and y-directions, or rather for cross-sections shearing the same neutral axis. Most sandwiches used in practical applications are quite close to this condition. But with these simplifications, the very complex governing equations can be transformed into much simpler equations to be solved for the bending and shear separately.

Assuming that $z_x = z_y = z$ are measured from the geometric middle plane of the plate, we get the following approximate set of cross-section rotations

$$\psi_x = -\frac{\partial w_b}{\partial x} \text{ and } \psi_y = -\frac{\partial w_b}{\partial y}. \tag{4.20}$$

By letting $u_0 = v_0 = 0$ one may then obtain

$$\begin{aligned} &u = -z\frac{\partial w_b}{\partial x}, \quad v = -z\frac{\partial w_b}{\partial y} \\ &\Rightarrow \epsilon_x = -z\frac{\partial^2 w_b}{\partial x^2}, \; \epsilon_y = -z\frac{\partial^2 w_b}{\partial y^2} \text{ and } \gamma_{xy} = -2z\frac{\partial^2 w_b}{\partial x \partial y}. \end{aligned} \tag{4.21}$$

Equations (4.14), (4.15) and (4.16) can now be transformed to

$$\begin{gathered} M_x = -\frac{D_x}{1-\nu_{xy}\nu_{yx}}\left[\frac{\partial^2 w_b}{\partial x^2} + \nu_{yx}\frac{\partial^2 w_b}{\partial y^2}\right], \; M_y = -\frac{D_y}{1-\nu_{xy}\nu_{yx}}\left[\frac{\partial^2 w_b}{\partial y^2} + \nu_{xy}\frac{\partial^2 w_b}{\partial x^2}\right], \\ M_{xy} = -D_{xy}\frac{\partial^2 w_b}{\partial x \partial y}, \; Q_x = S_x\frac{\partial w_s}{\partial x} \text{ and } Q_y = S_y\frac{\partial w_s}{\partial y}. \end{gathered} \tag{4.22}$$

It is now seen that the partial deflection w_b represents the classical plate bending deformation. Since the shear deflection does not rotate the cross-section, all bending moments will depend solely on w_b. The relation between w_b and w_s is found by substituting the above equations into Eq. (4.11) and (4.12), which yield

$$\begin{aligned} S_x\frac{\partial w_s}{\partial x} &= -\frac{D_x}{1-\nu_{xy}\nu_{yx}}\left[\frac{\partial^3 w_b}{\partial x^3}+\nu_{yx}\frac{\partial^3 w_b}{\partial x\partial y^2}\right]-D_{xy}\frac{\partial^3 w_b}{\partial x\partial y^2} && (4.23)\\ S_y\frac{\partial w_s}{\partial y} &= -\frac{D_y}{1-\nu_{xy}\nu_{yx}}\left[\frac{\partial^3 w_b}{\partial y^3}+\nu_{yx}\frac{\partial^3 w_b}{\partial x^2\partial y}\right]-D_{xy}\frac{\partial^3 w_b}{\partial x^2\partial y}. && (4.24)\end{aligned}$$

By differentiating the above equation, using Eq. (4.22) and inserting into the equilibrium equation (4.17) we get

$$S_x\frac{\partial^2 w_s}{\partial x^2}+S_y\frac{\partial^2 w_s}{\partial y^2}=-q^*. \tag{4.25}$$

Using (4.23) and (4.24) the equilibrium equation above may be expressed by

$$\frac{D_x}{1-\nu_{xy}\nu_{yx}}\frac{\partial^4 w_b}{\partial x^4}+\left[\frac{\nu_{yx}D_x+\nu_{xy}D_y}{1-\nu_{xy}\nu_{yx}}+2D_{xy}\right]\frac{\partial^4 w_b}{\partial x^2\partial y^2}+\frac{D_y}{1-\nu_{xy}\nu_{yx}}\frac{\partial^4 w_b}{\partial y^4}=q^* \tag{4.26}$$

which is the differential equation in pure bending of an ordinary orthotropic plate. If we accept the concept of partial deflections, we can now assume Eq. (4.25) to be valid for the case when the bending stiffnesses goes to infinity. Then all components in q^* takes the value of w_s so that Eq. (4.25) is truly an equation in w_s only. In the same manner, Eq. (4.26) can be solved with respect to w_b by setting the deflection components on the right hand side equal to w_b. The two solutions do not depend on each other and the total solution can be obtained by superposition.

4.3 Solving the plate equation, isotropic facings

Fourier solutions to the differential equations governing plate deflections, assuming isotropic facings are presented in this section. The equations are implemented in a computer using MAPLE in Section 6.2.4 where the deflections are compared with the static compression test described in Section 5.5.

4.3.1 Simplifications

For isotropic sandwich plates we have

$$D_x=D_y=D,\ \nu_{xy}=\nu_{yx}=\nu,\ S_x=S_y=S,\ \text{and}\ D_{xy}=\frac{D}{1+\nu}. \tag{4.27}$$

The concept of partial deflections introduced here, will now be exact. By using (4.27) the expressions relating w_b to w_s in Eqs. (4.23) and (4.24) reduces to the simple form

$$\Delta w_s=-\frac{D}{S(1-\nu^2)}\Delta^2 w_b \tag{4.28}$$

while the governing equation in Eq. (4.26) reduces to

$$\frac{D}{1-\nu^2}\Delta^2 w_b=q^*. \tag{4.29}$$

Here Δ is the Laplacian operator. In general, Eq. (4.28) can not yield edge values $w_s = 0$ since Δw_b will vary along the edge. Thus, w_b and w_s will not vanish separately on the boundary but only their sum will equal zero. By combining Eqs. (4.28) and (4.29) we can make the partial deflections vanish and we arrive at an equation for the total deflection

$$\frac{D}{1-\nu^2}\Delta^2 w = \left[1 - \frac{D\Delta}{S(1-\nu^2}\right] q^*. \tag{4.30}$$

4.3.2 Equations

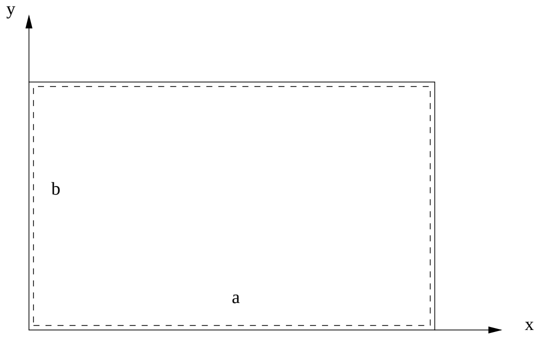

Figure 4.4: Rectangular simply supported plate

The boundary conditions for a simply supported plate is

$$w = 0,\ M_x = 0 \text{ at } x = 0 \text{ and } x = a$$
$$w = 0,\ M_y = 0 \text{ at } y = 0 \text{ and } x = b.$$

The deflection can be represented by a double Fourier sine serie

$$w = \sum_{n=1}^{\infty}\sum_{m=1}^{\infty} w_{mn} \sin\frac{m\pi x}{a} sin\frac{n\pi x}{b} \tag{4.31}$$

which satisfies all the boundary conditions. A transverse load can in a general form be written as

$$q = \sum_{n=1}^{\infty}\sum_{m=1}^{\infty} q_{mn} \sin\frac{m\pi x}{a} sin\frac{n\pi x}{b} \tag{4.32}$$

where q_{mn} are the Fourier coefficients that are determined by

$$q_{mn} = \frac{4}{ab}\int_0^a\int_0^b q(x,y)\sin\frac{m\pi x}{a}\sin\frac{n\pi x}{b}dxdy \tag{4.33}$$

for a prescribed surface load $q(x,y)$.

For a concentrated load Q acting in the centre of the plate the coefficients are obtained by expressing the pointload as the Dirac delta function. Let p be the intensity of a load uniformly distributed over a small square with sides c parallel to those of the plate. Set the point load $Q = pc^2$. Then

$$q_{mn} = \frac{4}{ab}\int_{\frac{a-c}{2}}^{\frac{a+c}{2}}\int_{\frac{b-c}{2}}^{\frac{b+c}{2}} \frac{Q}{c^2}\sin\frac{m\pi x}{a}\sin\frac{n\pi y}{b}dxdy \tag{4.34}$$

for odd values of n and m. Eq. (4.34) was approximated as

$$q_{mn} = \frac{4Q}{ab} \sin \frac{m\pi}{a} \sin \frac{n\pi}{b} \tag{4.35}$$

in [24] which is obiously wrong when solving Eq. (4.34). The correct approximated expression for the concentrated load is

$$q_{mn} = \frac{4Q}{ab} \sin \frac{m\pi}{2} \sin \frac{n\pi}{2}. \tag{4.36}$$

When substituting into Eq. (4.30) we get

$$\begin{aligned} &\frac{D}{1-\nu^2}\left[(\frac{m\pi}{a})^2 + 2(\frac{m\pi}{a})(\frac{n\pi}{b}) + (\frac{m\pi}{b})^2\right] w_{mn} \\ &\qquad = \left[1 + \frac{D}{1-\nu^2}((\frac{m\pi}{a})^2 + (\frac{n\pi}{b})^2)\right] q_{mn} \end{aligned} \tag{4.37}$$

which gives

$$w_{mn} = \frac{q_{mn}(1-\nu^2)}{D} \frac{1 + \frac{D}{S(1+\nu^2)}\left[(\frac{m\pi}{a})^2 + (\frac{n\pi}{b})^2\right]}{\left[(\frac{m\pi}{a})^2 + (\frac{n\pi}{b})^2\right]^2}. \tag{4.38}$$

The entire solution becomes

$$w = \sum_{n,m=1}^{k} \frac{q_{mn}(1-\nu^2)}{D} \frac{1 + \frac{D}{S(1+\nu^2)}\left[(\frac{m\pi}{a})^2 + (\frac{n\pi}{b})^2\right]}{\left[(\frac{m\pi}{a})^2 + (\frac{n\pi}{b})^2\right]^2} \sin \frac{m\pi x}{a} \sin \frac{n\pi x}{b}. \tag{4.39}$$

This expression can now be divided into the partial deflections as follows

$$w_b = \sum_{n,m=1}^{k} \frac{q_{mn}(1-\nu^2) \sin \frac{m\pi x}{a} \sin \frac{n\pi x}{b}}{D\left[(\frac{m\pi}{a})^2 + (\frac{n\pi}{b})^2\right]^2}, \text{ and } w_s = \sum_{n,m=1}^{k} \frac{q_m n \sin \frac{m\pi x}{a} \sin \frac{n\pi x}{b}}{S\left[(\frac{m\pi}{a})^2 + (\frac{n\pi}{b})^2\right]}. \tag{4.40}$$

When solving for the deflection, k must be taken large enough to give accurate results.

4.4 Solving the plate equation, orthotropic facings

To find expressions for the deflection for sandwich plates with orthotropic facings the full solution must be used. In short, by introducing the field assumptions from Eqs. (4.31) and (4.32) into Eq. (4.10) the relation between the unknown coefficients W_{mn}, T_{xmn} and T_{ymn} can be derived. The Fourier representation of the load q_{mn} is the same as used for isotropic facings in Eq. (4.34).

The cross-section properties are now calculated for the directions of orthotrophy. D_x, the relation between the bending moment M_x and the corresponding curvature $\partial^2 w/\partial x^2$ is defined in the same manner as for the beam;

$$D_x = \int E_x z^2 dz \approx \frac{E_x t_f d^2}{2}.$$

Similarly, D_y may be defined as follows

$$D_y = \int E_y z^2 dz \approx \frac{E_y t_f d^2}{2}.$$

An exact expression for the torsional stiffness D_{xy} is more difficult to assess. However, through use of Eqs. (4.21) and (4.22) we can write

$$M_{xy} = \int \tau_{xy} dz = \frac{\partial^2 w}{\partial x \partial y} \int 2z^2 G_{xy} dz \Rightarrow D_{xy} = \int 2z^2 G_{xy} dz \approx G_{xy} t_f d^2$$

assuming thin faces and weak core [24]. The shear stiffnesses S_x and S_y are calculated in the same manner as for the beam, ie.

$$S = S_x = S_y = \frac{G_c d^2}{t_c}$$

since the core is isotropic.

4.4.1 Equations

The field assumptions are now

$$\begin{aligned} w &= \sum_{n=1}^{\infty}\sum_{m=1}^{\infty} -\frac{W_{mn} q_{mn}}{Z_{mn}} \sin\frac{m\pi x}{a} \sin\frac{n\pi x}{b} \\ Q_x &= \sum_{n=1}^{\infty}\sum_{m=1}^{\infty} \frac{X_{mn} q_{mn}}{Z_{mn}} \sin\frac{m\pi x}{a} \sin\frac{n\pi x}{b} \\ Q_y &= \sum_{n=1}^{\infty}\sum_{m=1}^{\infty} \frac{Y_{mn} q_{mn}}{Z_{mn}} \sin\frac{m\pi x}{a} \sin\frac{n\pi x}{b} \end{aligned} \tag{4.41}$$

where the coefficients are

$$\begin{aligned} W_{mn} = &-\frac{1}{S_x S_y}\left[\frac{1}{2}D_{xy}\left\{\left(\frac{m\pi}{a}\right)^4 \frac{D_x}{1-\nu_{xy}\nu_{yx}} - \left(\frac{m\pi}{a}\right)^2\left(\frac{n\pi}{b}\right)^2 \frac{\nu_{xy}D_x + \nu_{yx}D_y}{1-\nu_{xy}\nu_{yx}}\right.\right. \\ &\left.\left.+ \left(\frac{n\pi}{b}\right)^4 \frac{D_y}{1-\nu_{xy}\nu_{yx}}\right\} + \left(\frac{m\pi}{a}\right)^2\left(\frac{n\pi}{b}\right)^2 \frac{D_x D_y}{1-\nu_{xy}\nu_{yx}}\right] - \left[\left(\frac{m\pi}{a}\right)^2 \frac{D_x}{S_x(1-\nu_{xy}\nu_{yx})}\right. \\ &\left.+ \left(\frac{n\pi}{b}\right)^2 \frac{D_y}{S_y(1-\nu_{xy}\nu_{yx})}\right] - \frac{1}{2}D_{xy}\left[\frac{1}{S_x}\left(\frac{m\pi}{a}\right)^2 + \frac{1}{S_y}\left(\frac{n\pi}{b}\right)^2\right] - 1 \end{aligned} \tag{4.42}$$

$$\begin{aligned} X_{mn}S_y = {} & \frac{1}{2}\left(\frac{m\pi}{a}\right)^5 \frac{D_x D_{xy}}{1-\nu_{xy}\nu_{yx}} + \left(\frac{m\pi}{a}\right)^3 \left(\frac{n\pi}{b}\right)^2 \Bigg[\frac{D_x D_y}{1-\nu_{xy}\nu_{yx}} \\ & - \frac{D_{xy}(\nu_{xy}D_x + \nu_{yx}D_y)}{2\Bigg(1-\nu_{xy}\nu_{yx})}\Bigg] - \frac{1}{2}\left(\frac{m\pi}{a}\right)\left(\frac{n\pi}{b}\right)^4 \frac{D_y D_{xy}}{1-\nu_{xy}\nu_{yx}} \\ & + S_y\left(\frac{m\pi}{a}\right)\left[\left(\frac{m\pi}{a}\right)^2 \frac{D_y}{1-\nu_{xy}\nu_{yx}} + \left(\frac{n\pi}{b}\right)^2 \left(D_{xy} + \frac{\nu_{xy}D_x}{1-\nu_{xy}\nu_{yx}}\right)\right] \end{aligned} \tag{4.43}$$

$$\begin{aligned} Y_{mn}S_x = {} & \frac{1}{2}\left(\frac{n\pi}{b}\right)^5 \frac{D_y D_{xy}}{1-\nu_{xy}\nu_{yx}} + \left(\frac{m\pi}{a}\right)^2 \left(\frac{n\pi}{b}\right)^3 \Bigg[\frac{D_x D_y}{1-\nu_{xy}\nu_{yx}} \\ & - \frac{D_{xy}(\nu_{xy}D_x + \nu_{yx}D_y)}{2\Bigg(1-\nu_{xy}\nu_{yx})}\Bigg] + \frac{1}{2}\left(\frac{m\pi}{a}\right)^4\left(\frac{n\pi}{b}\right) \frac{D_x D_{xy}}{1-\nu_{xy}\nu_{yx}} \\ & - S_x\left(\frac{n\pi}{b}\right)\left[\left(\frac{n\pi}{b}\right)^2 \frac{D_y}{1-\nu_{xy}\nu_{yx}} + \left(\frac{m\pi}{a}\right)^2 \left(D_{xy} + \frac{\nu_{xy}D_y}{1-\nu_{xy}\nu_{yx}}\right)\right] \end{aligned} \tag{4.44}$$

$$Z_{mn} = \left(\frac{m\pi}{a}\right)X_{mn} - \left(\frac{n\pi}{b}\right)Y_{mn} \tag{4.45}$$

Eq. (4.44) was found to have a few typing errors, but these are corrected here.

The deflection of a sandwich plate with orthotropic facings can now be found by implementing the above equations in a computer code. This is done in Section 6.2.4.

Chapter 5

Testing

5.1 Introduction

Materials are classified by how they behave when loads are applied. Material properties such as the elastic modulus and the shear modulus are found by loading the materials in the appropriate directions and studying the load-reaction curve from the test. In this thesis low-velocity impacts onto sandwich plates are studied and complex reactions such as delamination in the facings and crushing of the core strongly dictate the behaviour of our plates. Such complex behaviour is hard to predict and thorough testing is therefore necessary.

The tests in this Chapter is performed together with another student who studies low-velocity impacts onto glass-fibre reinforced plastics (GFRP) laminates.

5.2 Instrumentation

5.2.1 Introduction

A description of the instruments used to retrieve data from our tests and how they are used is presented here. Instrumentation of the test specimens and use of the logging equipment are done under supervision by scientists at SINTEF Materials technology.

5.2.2 Strain Gauges

The use of strain gauges is based on the fact that the resistance of a conductor changes when the conductor is subjected to strain. The relationship between strain and resistance variation is almost linear, and the constant of proportionately is known as the "sensitivity factor", or the "K factor" [15]:

$$K = \frac{\Delta R/R}{\Delta L/L}$$

where

R : gauge resistance
ΔR : resistance change due to strain
L : original length
ΔL : variation due to external forces

Quality of the data acquired from the strain gauges depend strongly on the skills of the engineer. Extreme accuracy are imperative for the data to be usable. Testing is also very expensive, and time and money are wasted while redoing tests because a strain gauge failed to deliver any results. Next comes a "cookbook" on how to mount strain gauges:

1. Inspection the strain gauge visually. Filter out useless gauges at an early start.
2. Measuring the resistance before mounting the strain gauges gives a clear indication if the gauge are working properly. The strain gauges used in this thesis have a resistance 120 Ω.
3. Where to place the gauges depend on what you want to measure. They must not be placed so they get crushed in the impact. Mark where and in what direction the gauges are to be placed. Rub with a fine sandpaper and clean with spirit. Make sure that the surface is smooth.

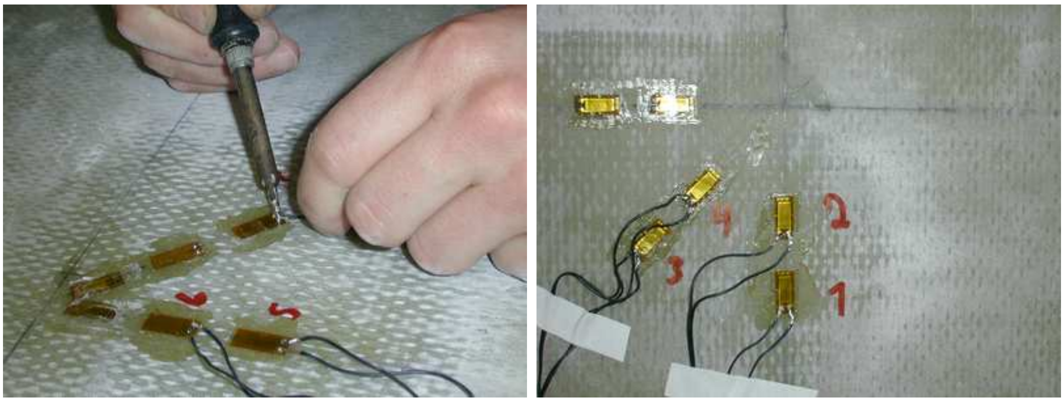

Figure 5.1: Solding wires onto the strain gauges

4. Gluing the gauges onto the specimen must be done with great care. If the strain gauges are not correctly aligned, the data obtained are not the data we are looking for. Place the gauge onto an adhesive tape with a pincette and mount the tape so the gauge will be in the right place. Put super glue onto the gauge and press down for 20-30 second using a Teflon strip (super glue will not stick to Teflon). Remove the adhesive tape and the gauge should be securely mounted.
5. Scrape the contact points on the gauge with a scalpel and clean with spirit to assure good contact. Solder cables onto the gauges, and measure the resistance. Always number the cables in both ends.

6. Attach the cables onto the sample with tape. Make sure that the cables will not stretch and tear off the strain gauges during the impact.

5.2.3 Accelerometer

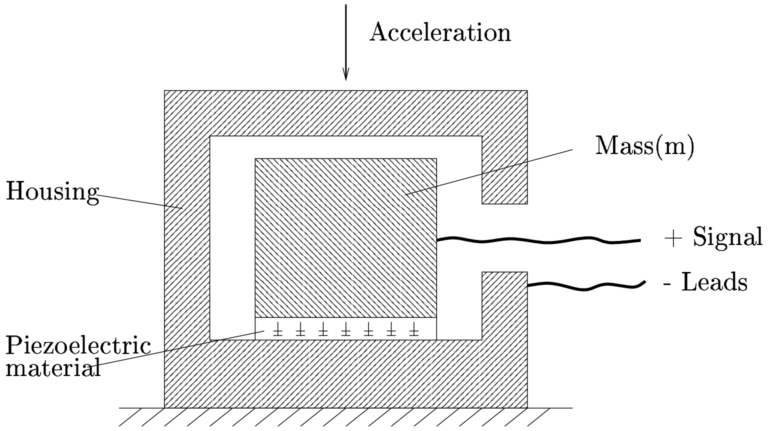

Figure 5.2: Illustration of accelerometer.

The impactor is equipped with an FGP FA 101 ± 500g piezoelectric accelerometer, shown in Fig. 5.2. Piezoelectric accelerometres rely on the piezoelectric effect of quartz or ceramic crystals to generate an electrical output that is proportional to applied acceleration. In an accelerometer, the stress on the crystals occurs as a result of the seismic mass imposing a force on the crystal. Over its specified frequency range, this structure approximately obeys Newton's law of motion, F=ma. Therefore, the total amount of accumulated charge is proportional to the applied force, and the applied force is proportional to acceleration. The electric charge can be measured by the fast logging equipment described in Section 5.2.4.

5.2.4 Fast logging

The stain gauges and accelerometer are connected to the Switching Box as seen in Fig. 5.3. The signals are sent from the Switching Box to the Strain Gauge Amplifier. Here the signal is filtered and amplified. The data is then transformed to digital data in the Digital/Analog Converter (DAC) and finally recorded on the computer.

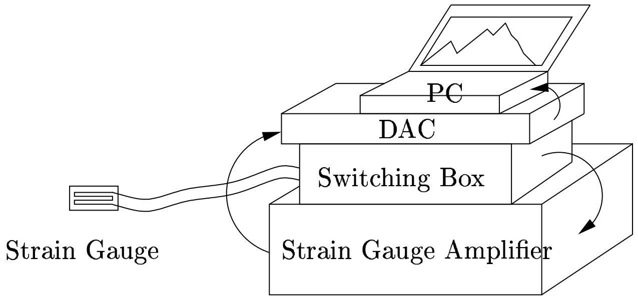

Figure 5.3: Illustration of the fast logging equipment

The Switching box is set up for 8 channels. With the Strain Gauge Amplifier we can adjust all parameters, but this is done more conveniently with the software on the computer. Beneath each contact on the Switching Box there is a button used to reset the resistance measured in the strain gauge and accelerometer to zero. These buttons should be pressed right before the test is about to begin so the signals is zeroed out.

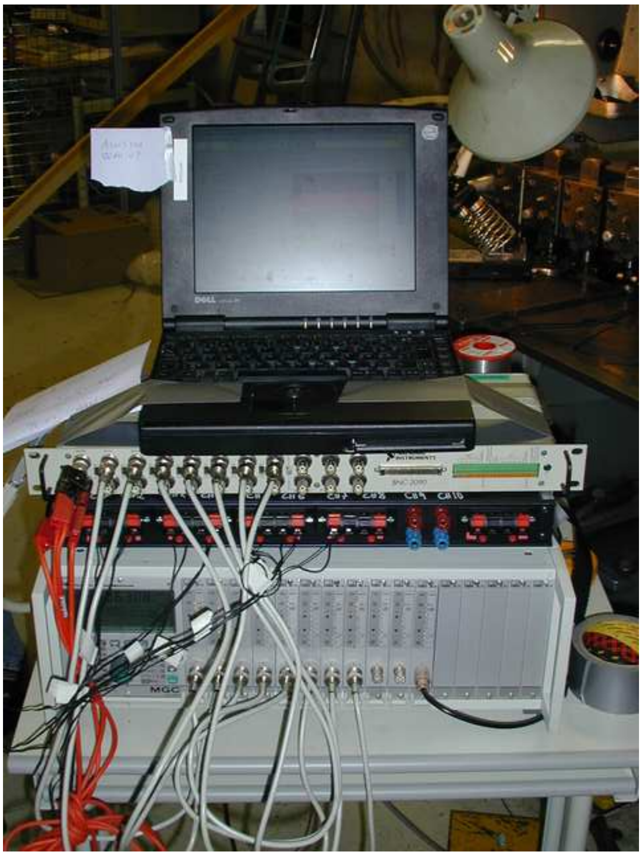

Figure 5.4: Picture of the fast logging station

Calibrate the strain gauge amplifier so that 10 Volt equals maximum strain measured by the strain gauges. Maximum strain likely to occur during the test can be found from a simulation or results from previous tests. Best accuracy is achieved when the full scale are used as illustrated in Fig. 5.5. The accelerometer is calibrated so that 10 V equals 500 g. The next step is to set up the correct logging frequency. Each channel can log maximum 40000 points in each test. With logging frequency 10000 Hz the time period logged is

$$\frac{40000}{10000\frac{1}{\mathrm{s}}} = 4\mathrm{s}$$

But the entire impact lasts only about 10 ms. Thus it is important to set the right logging frequency and number of points measured to assure reasonable accuracy during the impact. The logging starts when a pretrigger value set on one of the channels is reached. In our tests a pretrigger value 1/10 the maximum voltage was

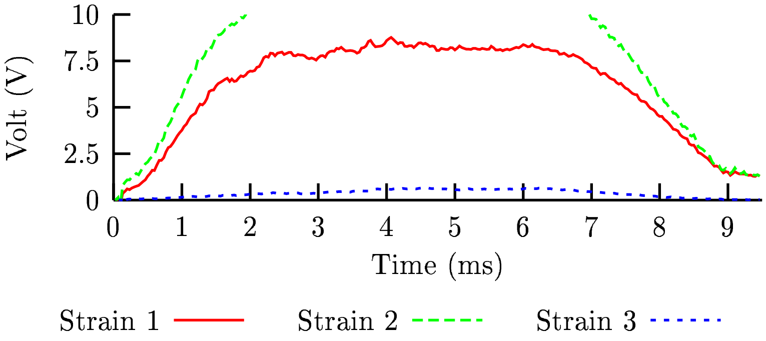

Figure 5.5: The figure shows volt signals from strain gauges for different scalings. Strain 1: scaled correct and uses the whole scale. Strain 2: maximum strain is higher in the test than predicted and data is lost. Strain 3: maximum strain is much lower than predicted and the accuracy is poor.

used on the acceleration channel and the logging started therefore when 1 V was reached.

To get the best quality data, a low-pass Bessel hardware filter in the amplifier is used in our tests, allowing only the signal below our cutoff value to pass. The purpose is to remove as much of the obscuring components of the signal as possible, without compromising the desired signal.

5.2.5 Rosand instrumented falling weight impactor

The Rosand instrumented falling weight impactor allows us to control all parameters from the computer. The software takes energy, velocity or height as input, and adjusts the impactor so it is dropped from the correct height. This assures accurate input values and a reliable and reproducible testing environment. The machine can catch the impactor so there will not be a second strike on the test specimen. A chamber covering the test specimen makes temperatures from $-40\,°\mathrm{C}$ to $+200\,°\mathrm{C}$ possible.

A force sensor is attached to the impactor logging the force felt on the impactor during the impact. From the force vs. time trace the computer software calculates acceleration, velocity, energy and deflection during the impact.

Unfortunately, our sandwich plates are to large to fit in this machine and the maximum energy level possible is to low for the sandwich impact tests. A larger test rig is therefore constructed for our tests. However, the Rosand instrumented impact machine is used while calibrating the accelerometer and learning to use the fast logging instruments.

5.3 Calibrating the accelerometer

5.3.1 Introduction

To get the same information from our tests as from the Rosand impact machine, we equipped the projectile in our constructed drop weight test rig with an accelerometer. Before using the accelerometer in our tests, we had to calibrate and test it to make sure that it was working correct. A common way to test and verify an accelerometer

Figure 5.6: Picture of the Rosand impact machine.

is to attach it to an oscillator. However, in lack of a oscillator, we had to use a different, but equally good, approach with the equipment available to us.

5.3.2 Test setup and specifications

The Rosand instrumented drop weight machine has a force sensor in the impactor. Thus, it can calculate the acceleration in the impactor during the impact. Our accelerometer is taped onto the impactor and connected to the fast logging equipment described in Section 5.2.4. The acceleration from our accelerometer is now directly comparable with the acceleration from the Rosand impact machine. Two GRP plates were used in the impact tests. Each plate was impacted twice. In the first two tests we used impact energy 10 J while 20 J impact energy was applied in the last two tests.

5.3.3 Test results

The results from the calibration are shown in Fig. 5.7. As seen the accelerometer oscillates much more than the Rosand acceleration. These oscillations are most likely due to the weak mounting of the accelerometer which allows the accelerometer to move independently of the impactor. At about one ms the accelerometer curves show a distinct drop in all the tests. This is due to the wire connected to the accelerometer pulling the accelerometer. Apart from the fluctuations are the results from

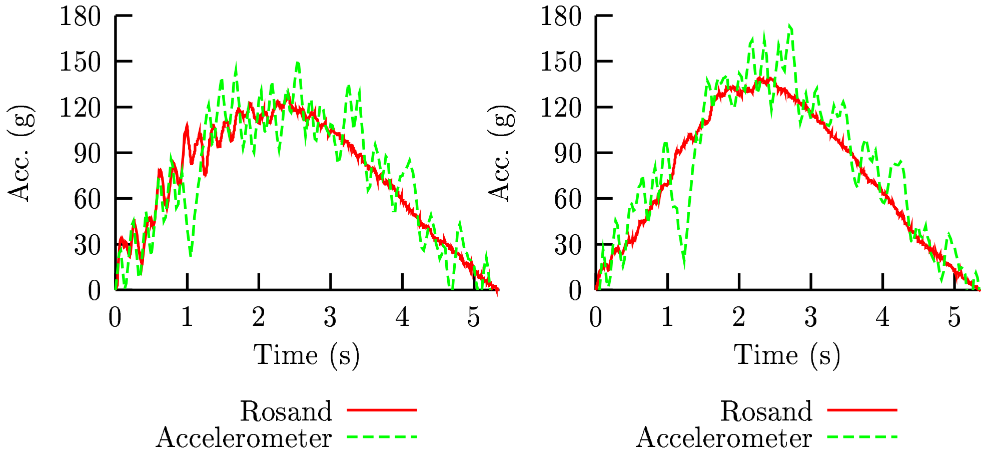

(a) Test 1 and 2 are done with impact energy 10 J.

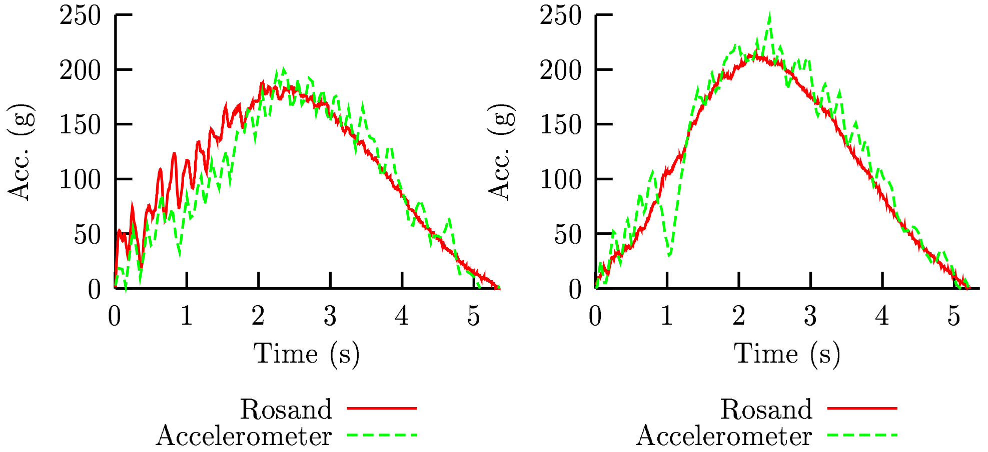

(b) Test 3 and 4 are done with impact energy 20 J.

Figure 5.7: Plot of acceleration vs. time (g/ms)

the accelerometer and from the Rosand impact machine in very good agreement. The accelerometer are therefore ready for further use in impact experiments.

The second strike on each plate (Test 2 and 4) shows less oscillations in the first part of the impact. The plate is now softer due to delamination from the first impact. This gives lower accelerations and less oscillations when the impactor hits the plate. The second impact on each plate also shows slightly higher maximum acceleration. Thus from Newton‘s 2nd law $F = ma$, slightly higher force is observed by the impactor. This is because less energy is used to delaminate the plate and the projectile is not slowed down so gradually resulting in higher accelerations.

5.4 Drop Weight Impact Tests

5.4.1 Introduction

Structures may respond differently when subjected to dynamic rather than static loads. The ability of sandwich plates to withstand dynamic loads depend on the properties of the core and faces and how they behave together as a sandwich construction. Understanding how the energy is absorbed in the core and faces during impact is important when studying the dynamic behaviour in our sandwich plates. Impact tests are therefore necessary in order to fully understand the dynamic response of our plates.

Three sandwich plates are tested in a drop weight test rig and the results are discussed later in this Section. The data from the tests also give valuable information when calibrating and understanding the behaviour of our dynamic simulations.

5.4.2 Drop weight impact setup

The test rig is schematically illustrated in Fig. 5.8. It consists mainly of a 4 m long Perspex tube holding the projectile and a frame supporting the sandwich plates. Vibrations are reduced to a minimum during the impact by securely mounting the tube to the rig, while the rig is adjusted carefully to keep the tube perpendicular. Furthermore, the tube is ventilated to avoid turbulence giving rise to undesired vibrations in the accelerometer data. This will be explained later. A quadratic frame with light opening 570 mm x 570 mm supports the sandwich plates. The frame is made from steel pipes with diameter 40 mm which are welded together at the corners. Steel u-beams placed on Leca-blocks support the frame. Leca-blocks are used to prevent the plate from reaching the floor during impact. Both the frame and the u-beams are strapped onto the Leca blocks so the frame is kept steady and rigid.

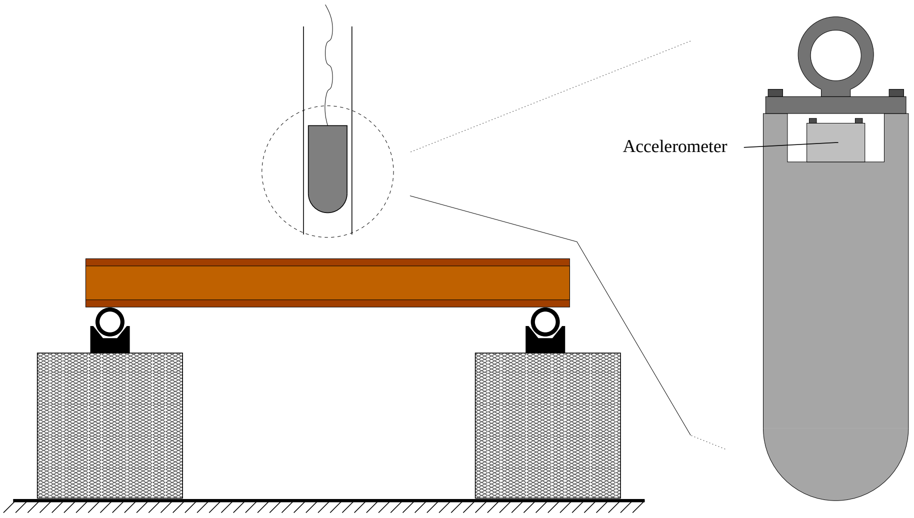

Figure 5.8: Drop weight rig and projectile with accelerometer attached.

Our projectile, which is made of steel, has a mass 6.2 kg and diameter 75 mm. At the top of the projectile the accelerometer is mounted as illustrated in Fig. 5.8. The second impact is prevented with a thick rubber plate.

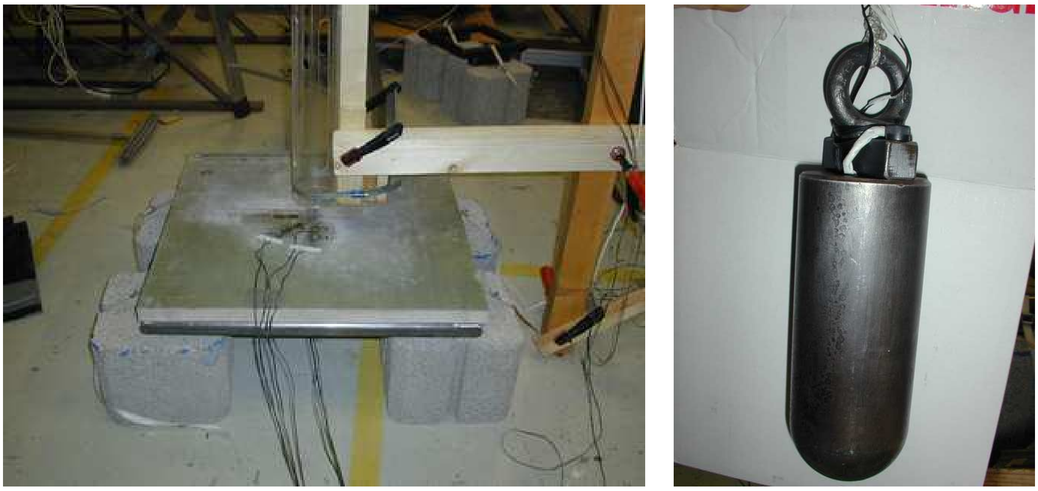

(a) Frame supporting the sandwich plate. (b) Projectile with accelerometer

Figure 5.9: Test rig and projectile.

5.4.3 Difficulties with the test rig setup

A lot of impacts onto test specimens were conducted prior to the final impacts onto our sandwich plates. The first results from the accelerometer did not offer significant insight into the impact behaviour of the plate, resulting in a long and instructive road towards obtaining reasonable data.

The main part of the noise in our data came from to the air flow in the tube. Due to the relative high speed of the projectile, a lot of air had to be pressed away during the impact. This caused the projectile to vibrate as air was flowing between the tube wall and the projectile, giving rise to major oscillations in our acceleration data. The problem was solved by drilling several long holes in the tube, allowing the air to flow out of the tube during the impact.

In our early attempts, the rope used to hoist the projectile into position was pulled after the projectile when the projectile fell towards the plate. The pull from the rope disturbed the acceleration of the projectile and made the acceleration results unusable. This was solved by hoisting the projectile into position with the rope and then cut it, allowing the projectile to fall free.

The wires connected to the accelerometer could also disturb the results by pulling the projectile during the impact. This was prevented by curling up the wire above the projectile, allowing the projectile to fall without the extra pull from the wire.

Due to the drilled holes in the tube, the accelerometer wire was cut or damaged as the projectile bounced back up the tube after the impact. The damaged parts had to be cut of, and new wires solded on for each test. Along with the cutting of the rope, this made the preparations for each test very time consuming. However, our test results were now reproducible and reliable.

5.4.4 Mechanical filters in the amplifier

The amplifier in the fast logging setup has a built in mechanical filter. Some of the acceleration data were corrupted because a wrong filter frequency was applied. Fig.

(a) Air holes in the tube, allowing the air to flow out of the tube during impact.

(b) Projectile and wire ready for the next impact test

Figure 5.10: Pictures of the drilled air channels in our tube and the projectile ready for the next impact.

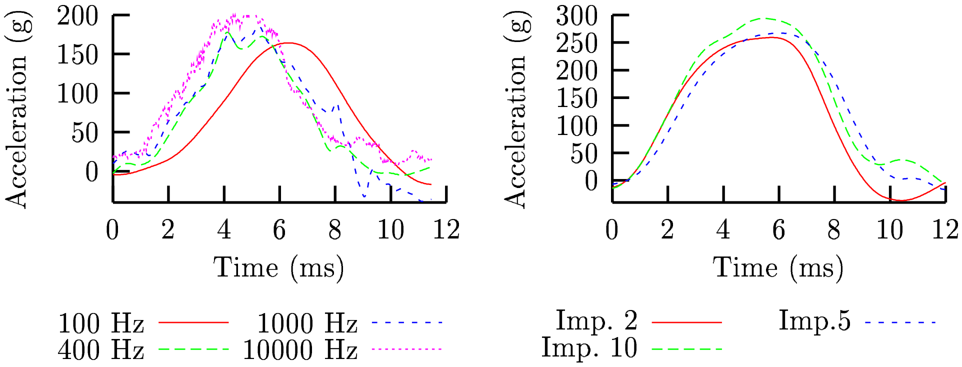

(a) Acceleration vs. time with different filters.

(b) Accelerations from the second, fifth and tenth impact on the same plate filtered through 100 Hz.

Figure 5.11: Accelerations with different filters applied.

5.11(a) shows how the acceleration varies with different filters. The first acceleration data were filtered through 100 Hz, and the data where therefore smoothed too much. Although the curves are fairly similar the acceleration starts a bit too late and the maximum acceleration is a bit too small compared to the less filtered curves. According to the amplifier manual [12], are the signal delayed with about 1.8 ms when using the 100 Hz filter and 0.03 ms when the 10000 Hz filter is applied.

Our third plate was impacted 10 times. Fig. 5.11(b) shows the acceleration filtered with 100 Hz for impact 2, 5 and 10. According to the figure, the acceleration does not change significantly as the plate is impacted several times. When calibrating the accelerometer two impacts were conducted on each GRP-laminate as shown in Fig. 5.7. The differences between the first and second strike are very small according to the deflection-acceleration curves. As explained later the acceleration data will be processed further calculating the velocity, kinetic energy and deflection by numerical integration. Any differences will be further reduced as illustrated in Fig. 5.12. Encouraged by this results, sandwich plates 1 and 2, which had been subjected to a simple impact each, were now impacted a second time using the 10000 Hz filter on the acceleration. The acceleration data from the second strikes onto sandwich plates 1 and 2 are therefore used further in this thesis.

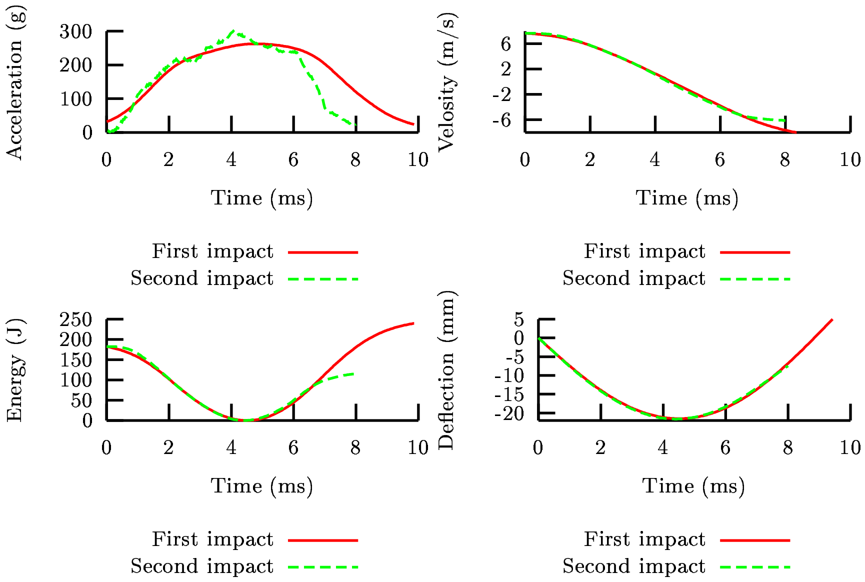

Figure 5.12: The acceleration data from the first and second strike onto plate 1. As seen the differences in the acceleration data is reduced as the velocity, energy and deflection is calculated.

All strain data from the test were filtered with the right frequency and was not inflicted by the problems described above.

5.4.5 Test specifications and instrumentation

Three sandwich plates with equal properties and dimensions are tested in the drop weight rig. The plate dimensions are shown in Fig. 5.13. Two different drop heights are used; 3.0 m and 3.5 m. Due to the preparations described in Section 5.4.3, friction and air resistance are neglected and the energy of the projectile as it reaches the plate is calculated from $E = mgh$, giving impact energies $E_1 = 182$ J and $E_2 = 213$ J.

The test plates are instrumented with strain gauges, and the gauges are placed in a way to register both local and global strains. Seven gauges were mounted on each plate. The position of the gauges are illustrated on the strain figures. A FGP FA 101 ± 500 g accelerometer is bolted in silicone to the 6.2 kg projectile [8].

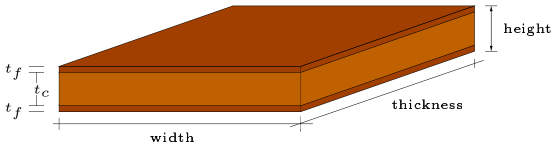

width:	620	(mm)
thickness:	620	”
height:	31	”
t_f	3	”
t_c	25	”

Figure 5.13: Geometric properties of the sandwich plates.

5.4.6 Accelerometer results

One of the impacts were filmed with a digital camera. Fig. 5.14 shows some pictures of the sandwich plate during the impact. The rubber plate used to catch the second strike can also be seen, along with the projectile.

(a) Ready for impact

(b) The projectile on the way down the tube right above the plate

(c) Right after the impact. The projectile is bouncing back up the tube. The sandwich plate is lifted off the frame.

(d) The rubber plate is placed between the tube and plate right after the impact to prevent the projectile to cause and damage on the second strike.

(e) The projectile hits the rubber plate without causing damage to the sandwich plate

(f) The impact is over.

Figure 5.14: Impact onto a sandwich plate

Plate 1 was hit from 3.0 m, while plate 2 and 3 were hit from 3.5 m. Due to the problem described in Section 5.4.4, were plate 1 and 2 rehit with the correct filter on the acceleration data. The resulting accelerometer vs. time curves are plotted in Fig. 5.15. As seen, the curves show exactly the same behaviour. At about 2.3 ms the indentator and plate lose contact with each other. At 4 ms, the indentator reaches maximum acceleration. After about 10 ms the indentator leaves the plate and the impact is over. The projectile might hit the tube walls and cause some distortions in the acceleration data while it goes back up the tube at the end of the impact.

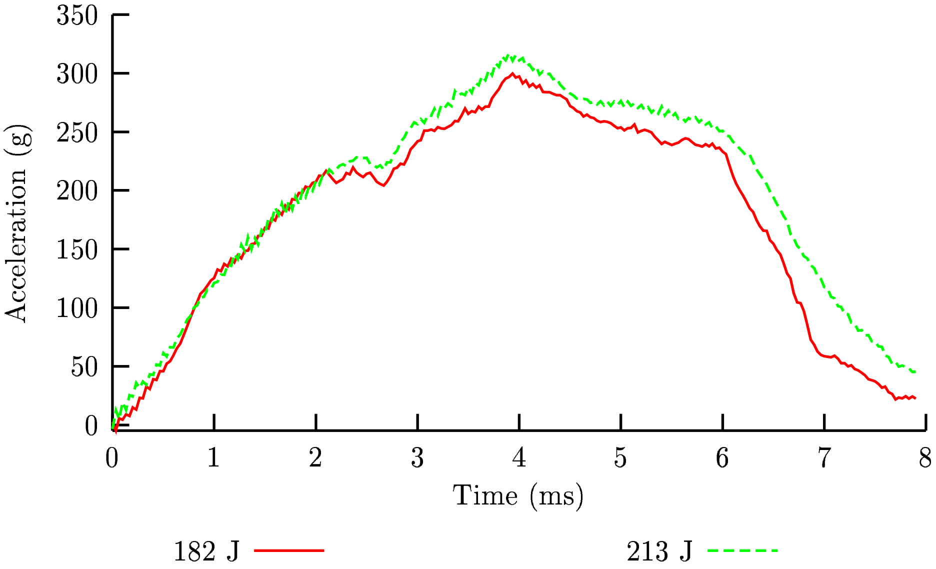

Figure 5.15: Acceleration vs. time curves for plate one and two. The first plate was impacted from 3.0 m and the second from 3.5 m.

The accelerometer data can be further examined, giving valuable information about the material tested. By integrating the acceleration, the velocity of the projectile during the impact can be found, and thus also the kinetic energy given by $E_k = \frac{1}{2}mv^2$. Integrating the velocity, gives the deflection of the projectile during the impact. Finding the kinetic energy is also necessary when comparing the simulations with the test results. The trapezoidal integration scheme defined by

$$\int_a^b f(x)dx = h\left(\frac{f(a)+f(b)}{2} + \left(\sum_{k=1}^{n-1} f(a+ik)\right)\right),$$

is applied. Here, $h = \frac{b-a}{n}$ is the step size. The integration scheme was coded using MAPLE, and the programme can be found in Appendix B.2.

The load applied on the plate is found from $F = ma$. In Fig. 5.16, the load-time and energy-time traces are plotted. The available energy E_0 is 213 J. The energy-time trace is found from $E = E_0 - E_k$. At point 1 the energy absorbed by the specimen is 69 J. Oscillations in the load-time trace at this point indicate visible incipient damage. At point 2 there is loss of contact between the indentator and the plate. Between point 2 and 3, at approximately 15000 N a change in the gradient of the trace takes place. This change in the loading rate is believed to represent specimen relaxation as damage occurs. At peak load (point 3) the absorbed energy is 207 J. The absorbed energy at point 4 is 213 J, which is equal to the initial impact energy. The indentator is stopped at this point, and the specimen has incurred damage. At point 5 the absorbed energy is 63 J. This result indicates that 150 J, the difference between the available impact energy E_0 and the final absorbed energy, has been returned to the indentator.

From the force-time traces, several important impact mechanisms can be examined. The force-time curves reflect the damage inflicted on the specimen, and changes in the gradient reflect changes in the deformation mechanism. More information on studying force-time traces can be found in [22].

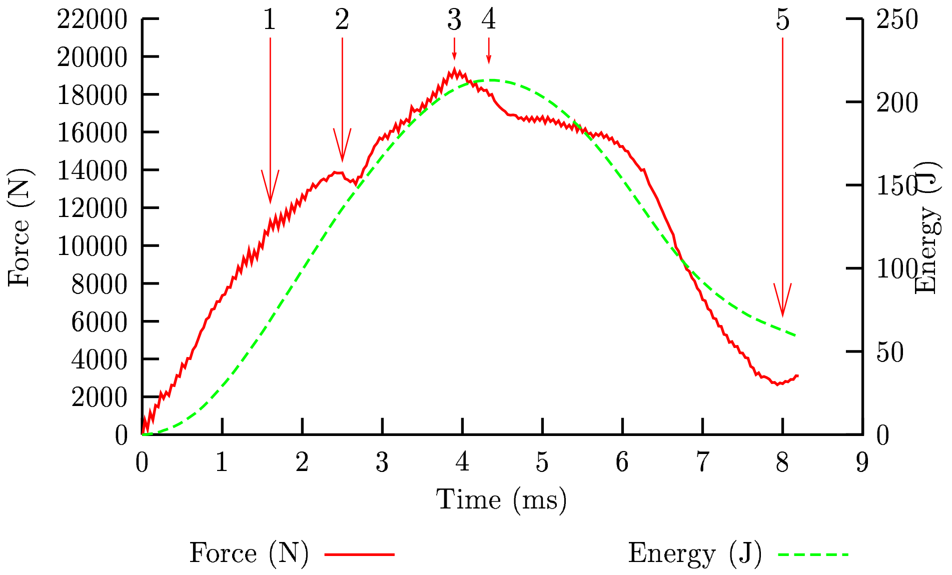

Figure 5.16: Plot of the acceleration and kinematic energy for the projectile found for plate 2. The numbers 1, 2, 3, 4 and 5 are explained in the text.

5.4.7 Strain gauge results

Each plate was instrumented with seven strain gauges. The strain gauges were placed so that they would bring results from both local and global strain in the sandwich facings. Each gauge was oriented in either the 0 or 90 fibre direction or in between at 45 degrees. The placing of the strain gauges on each plate are indicated on the time-strain traces for each plate. Due to symmetry, only 1/4 of the plate was instrumented. On the top-face, the strain gauges were placed close to the point of impact to retrieve information on local effects due to indentation of the core. The gauges on the bottom face bring results on the global deflection of the plate. Strain gauges are very fragile and easily broken, and gauges situated on areas where matrix-cracks appears during the impact, are likely to break due to the matrix cracking. When using the rubber plate to prevent the second strike from the projectile, the strain gauges might suffer damage and stop working.

Fig. 5.17 show the strain gauge traces for the first impact onto plate 1. Strain gauge 2 and 6 broke during the impact, and are not plotted in the figure. The largest strains take place on the top face. Strain gauges 5, 6 and 7 on the bottom face give less than half the strain of the top face. The local deflection due to indentation of the core close to the projectile are therefore greater than the more global deflection of the sandwich plate. The strains at points 5 and 7 were expected to be almost equal, but strain 7 is smaller. This behaviour is explained in Section 5.4.8. The maximum observed strain is 1.1 %. This is much lower than the failure strain, $\sigma_f = 3\,\%$ in the face. Therefore, the face sheets are not going to fail due to tensile strain in our tests.

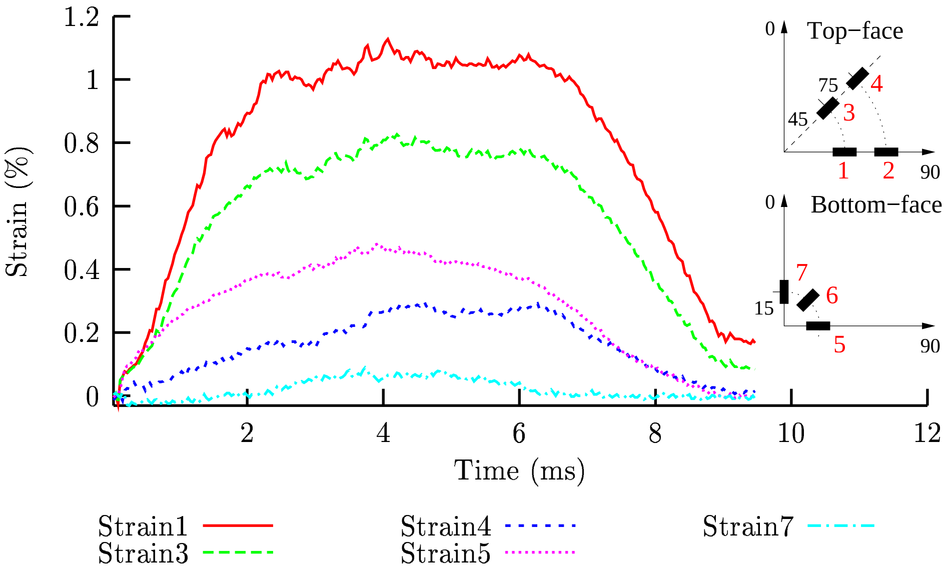

Figure 5.17: Strain gauge traces for plate 1

Fig. 5.18 show the strain gauge results from the first impact onto plate 2. All our strain gauges worked properly in this test. Strains at the points 1 and 2 are now in the 0 direction, while being in the 90 direction for plate 1. As seen, the strain in the 0-direction is smaller than in the 45-direction, indicating higher strains in the 90-direction than in the 0-direction. When comparing gauges that lies on the same place on each side, i.e. gauge 1 and 5, 2 and 6 and 3 and 7, it is clear that the deflection on the top face is largest.

Due to an interference problem with other electrical equipment, the pretrigger value was reached to early, and the first impact onto plate three was not logged. Fig. 5.19 shows therefore the strain gauge results from the second impact onto plate 3. Strain gauge 4 and 5 broke during the impact, and the results from these gauges are therefore not plotted in the figure. The results clearly follow the trend that the strains are largest in the 90 direction, and lowest in the 0 direction.

Comparing the strain from gauge one on plate 1 and 3, shows that the strain is about 0.2% higher on plate 1. The largest strain values were expected in plate three since this plate was impacted with higher energy. However, since the data from plate 3 is from the second impact onto the plate, the first impact has crushed the core and reduced the strains at the points where the gauges were placed as illustrated in Fig. 5.20.

5.4.8 Differences in the 0- and 90 direction

When symmetric laminates are tested in uniaxial stress, the 0 and 90 directions show the same strength. The results from our tests show that the strain is largest in the 90 direction. Fig. 5.21 illustrates the bending of the face close to the indentator in the 0 and 90 direction. The effect of the core supporting the face is neglected along

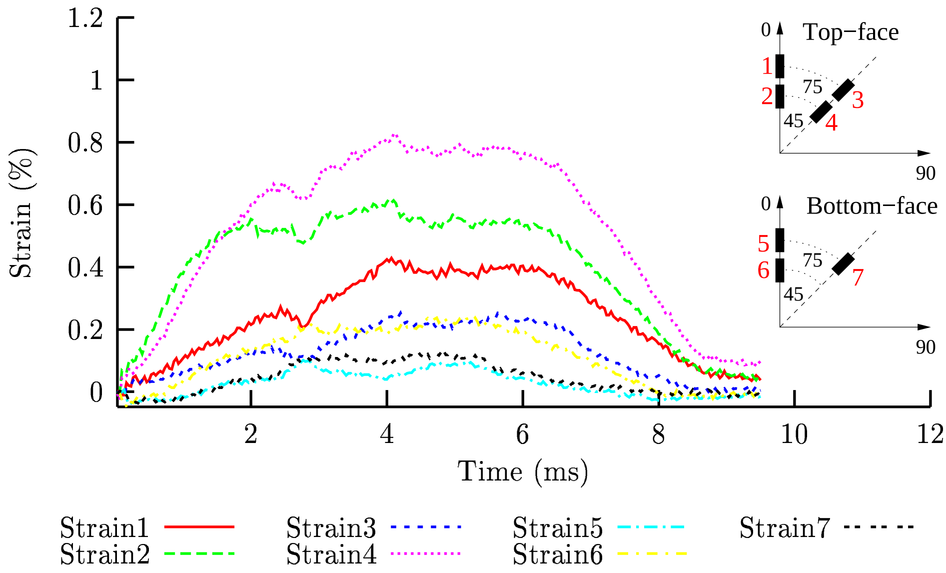

Figure 5.18: Strain gauge traces for plate 2

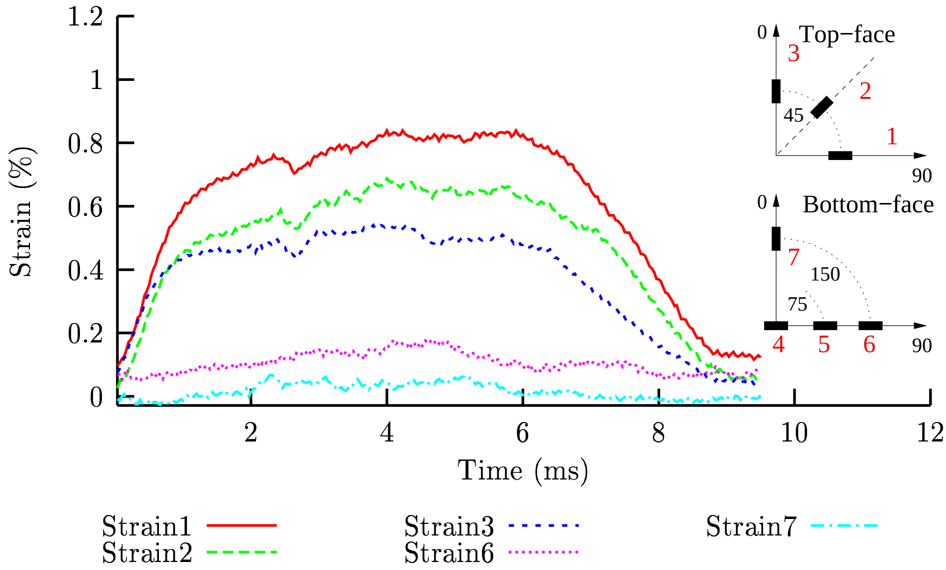

Figure 5.19: Strain gauge traces for plate 3

with the contribution from the fibres lying parallel to the bending axis. Assuming pure bending of the face the flexural rigidity for the 0 and 90 direction becomes

$$D_0 = \frac{E_f t_f h_0^2}{2} \quad \text{and} \quad D_{90} = \frac{E_f t_f h_{90}^2}{2}, \tag{5.1}$$

where

$$h_0 = 1.5\frac{t_f}{4} \quad \text{and} \quad h_{90} = 0.5\frac{t_f}{4}. \tag{5.2}$$

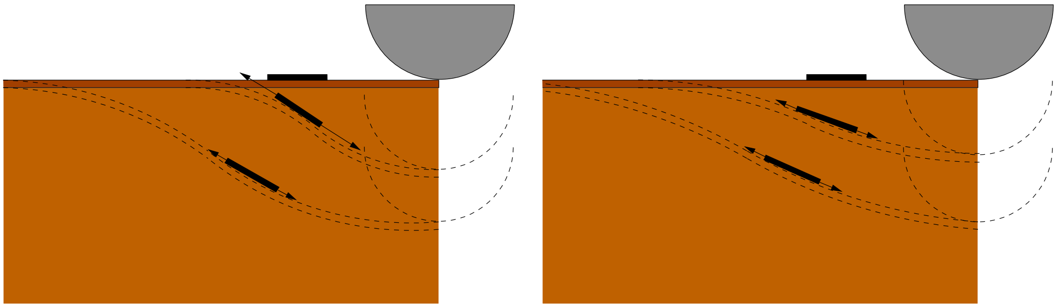

(a) First impact onto the plate. The strain in the face close to the projectile is high.

(b) Second impact onto the plate. The core under the impact area is crushed from the first strike resulting in lower strains close to the projectile because less bending action take place.

Figure 5.20: Illustration of first and second impact onto a sandwich plate. The first impact crushes the core, resulting in lower strains in the face during the second impact.

The strains in the fibres in the 0 and 90 direction becomes

$$\epsilon_0 = \frac{Mh_0}{2D_0} \quad \text{and} \quad \epsilon_{90} = \frac{Mh_{90}}{2D_{90}}. \tag{5.3}$$

Dividing ϵ_{90} by ϵ_0 shows that the strain is 3 times larger in the 90 direction than in the 0 direction. This explains why our test results show largest strains in the 90 direction.

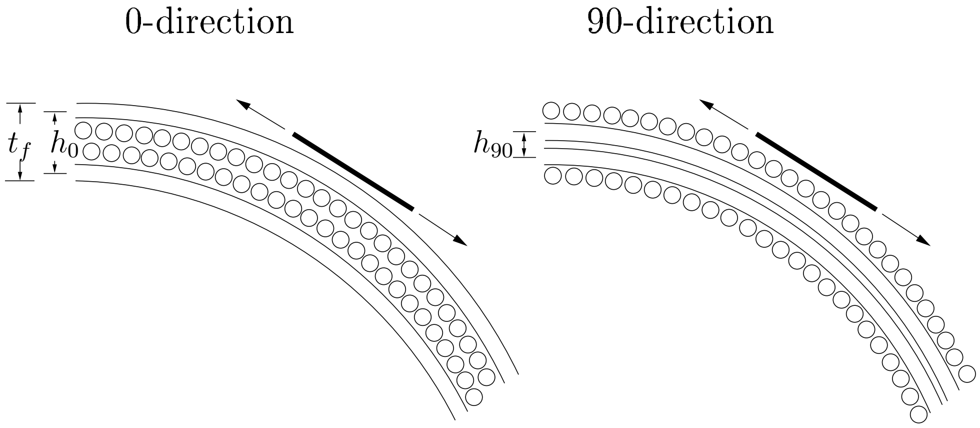

Figure 5.21: Illustration of the fibres in the top face close to the indentator in both 0 and 90 direction along with the strain gauge glued to the surface.

All three plates have one gauge placed 45 mm from the centre at 45 degrees on the top face. The data from these gauges are plotted in Fig. 5.22. The strain values in plate 2 were expected to be larger than the strain values in plate 1 for the top face gauges, since the impact energy was higher in plate 2. Plate 3 has the lowest strains in the top face. This is because the data is from the second strike on the plate as illustrated in Fig. 5.20. The first strike has crushed the face and softened the sandwich, resulting in lower strains.

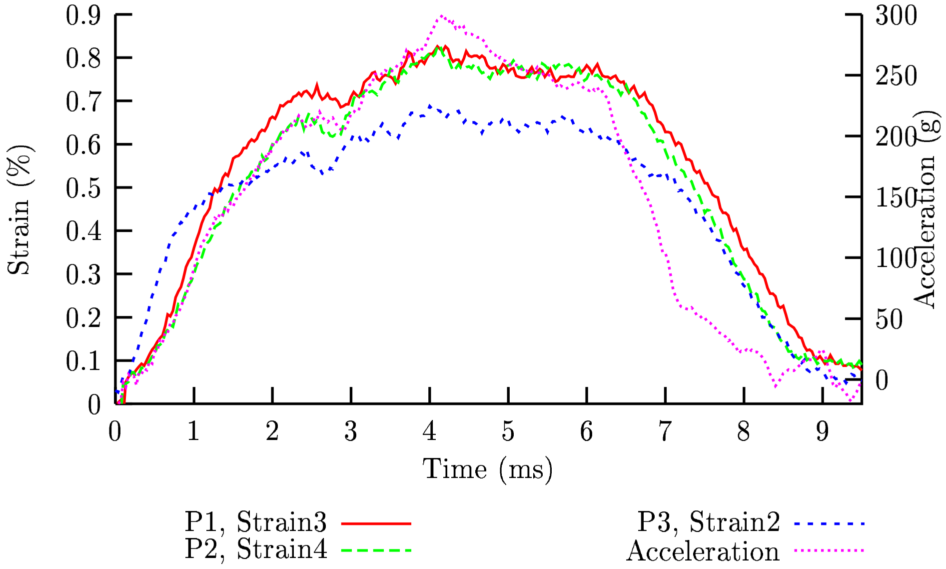

Figure 5.22: Comparing strains from a strain gauge placed 45 mm from the centre and at 45 degrees.

At about 2.5 ms, the loss of contact between the projectile and facing was found from studying the acceleration data. As seen in Fig. 5.22, the loss of contact is also clearly visible in the data from the top face gauges.

At about 9 ms, the acceleration goes towards zero and the projectile leaves the plate. Then the strain data stabilize and the impact is over.

5.4.9 Visual inspection

Fig. 5.23 show plate one after being subjected to two impacts. Visible damages are only observed within a small circle of radius 20 mm.

Plate two was cut so the internal damage could be studied. Fig. 5.24(a) shows the upper facing close to the point of impact. Matrix cracks are clearly visible in the 0-direction. Also, delamination takes place in the facing under the point of impact. This can be seen in Fig. 5.24(b), where the lower 0-lamina is clearly separated from the 90-layer above.

There is no visible damage in the core and bottom face. However, when pressing down on the point of impact, the sandwich flex a lot. This is not possible in the other corners. The residual stiffness is therefore reduced due to the impact.

5.5 Static deflection of sandwich plates

5.5.1 Introduction

By applying static loads on our test specimens, a lot of information on the behaviour and performance of the plates can be found. One sandwich plate is therefore tested

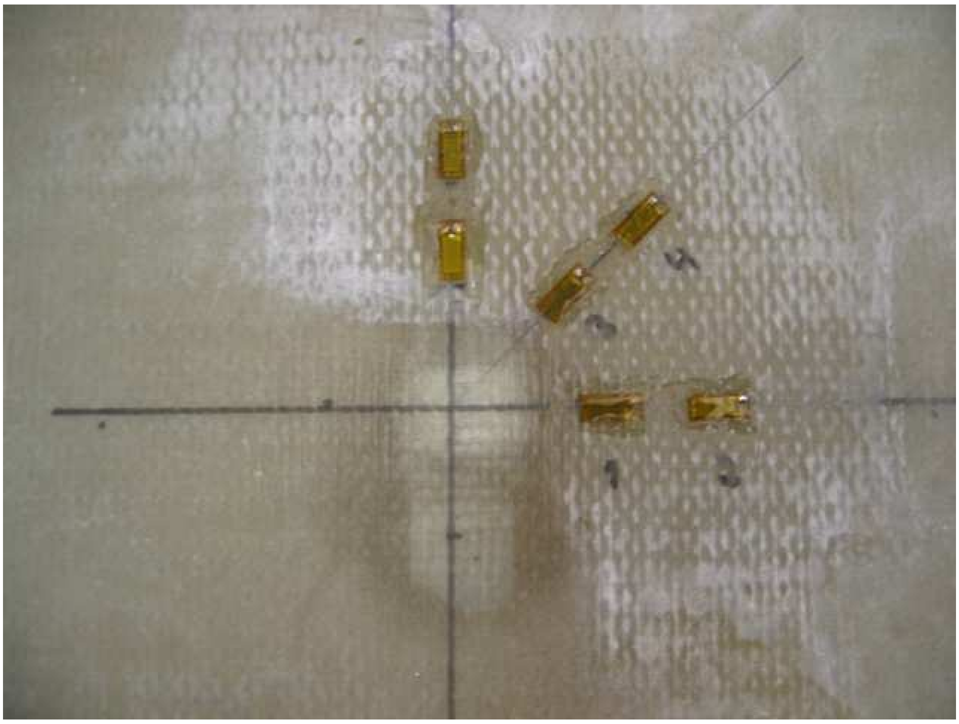

Figure 5.23: Picture of upper facing of plate one after impact.

in static compression.

5.5.2 Test specifications

One sandwich plate was tested in static compression in a Schenck TREBEL RM100 Electro Hydraulic Strain Machine, which allows loads up to 100 kN. The frame and projectile used in our dynamic impact tests are also used here. The indentator is lowered vertically with a rate of 10 mm/min.

5.5.3 Instrumentation

The plate is instrumented with seven strain gauges as shown in Fig. 5.25. The Schenk test machine logs the deflection of the indentator and the force on the indentator during the test.

5.5.4 Test results

Fig. 5.26 shows the load-deflection trace from the static test. As seen are the load-deflection trace almost linear up to failure. A key question here is; how much of this deflection is due to global deflection of the whole plate and how much is due to indentation of the face? We do not know this exactly, but studying the strain gauge results give a few indications.

Fig. 5.27 shows the strain gauge results plotted against the load. At about 7500 N or 12 mm deflection, some significant changes occurs in the strain curves. Gauge 1 and 4, the two gauges closest to the impactor show less strain, while the strains from

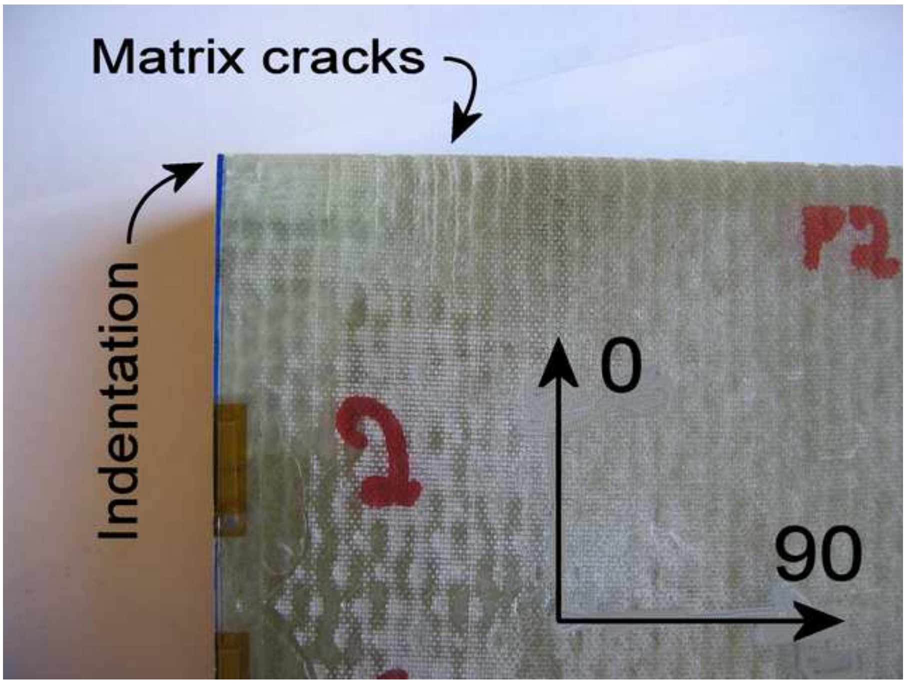

(a) Top face of sandwich plate. Matrix cracks in the 0-direction has occurred.

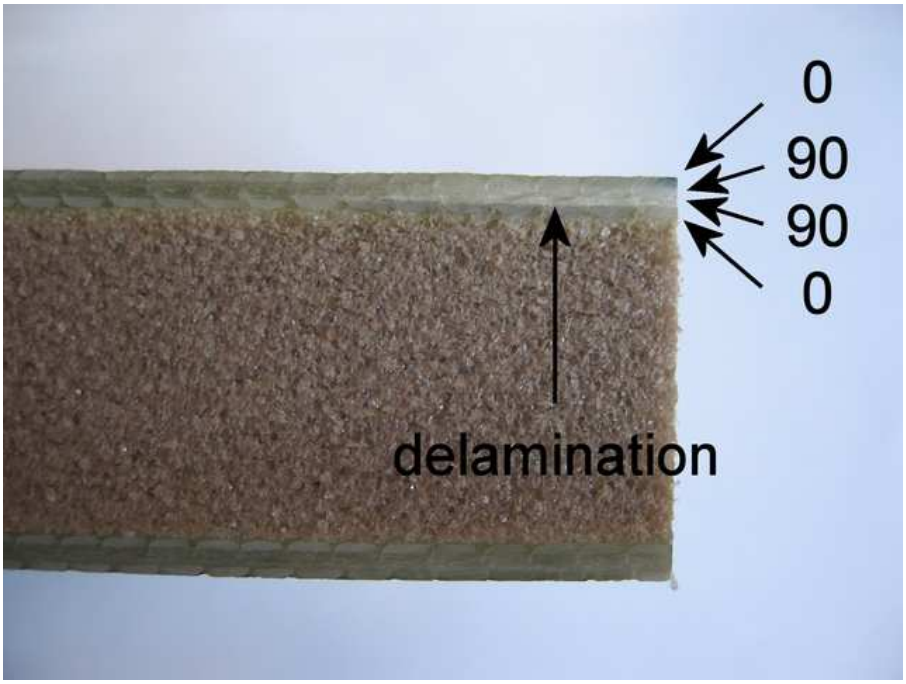

(b) Delamination between the two bottom layers are clearly visible.

Figure 5.24: Pictures of plate two after impact.

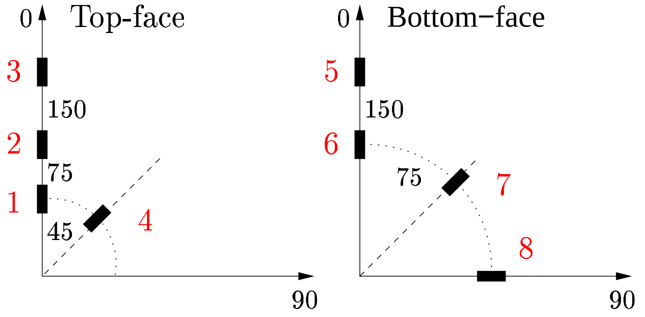

Figure 5.25: Strain gauge placement on the plate.

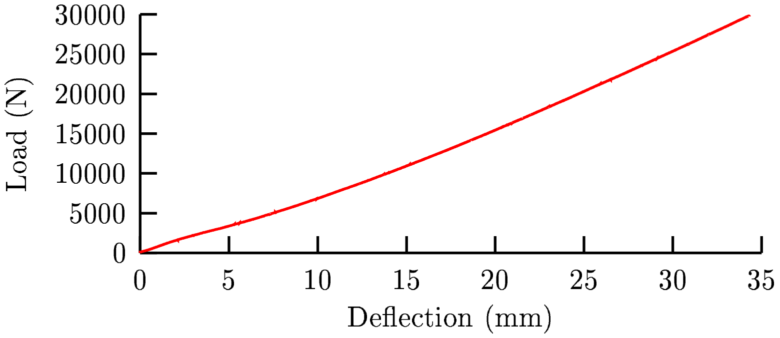

Figure 5.26: Load plotted against deflection of the indentator.

gauge 3 on the top face along with the bottom face gauges starts to increase. This means that the local indentation of the core decreases, while the global deflection of the sandwich starts to increase.

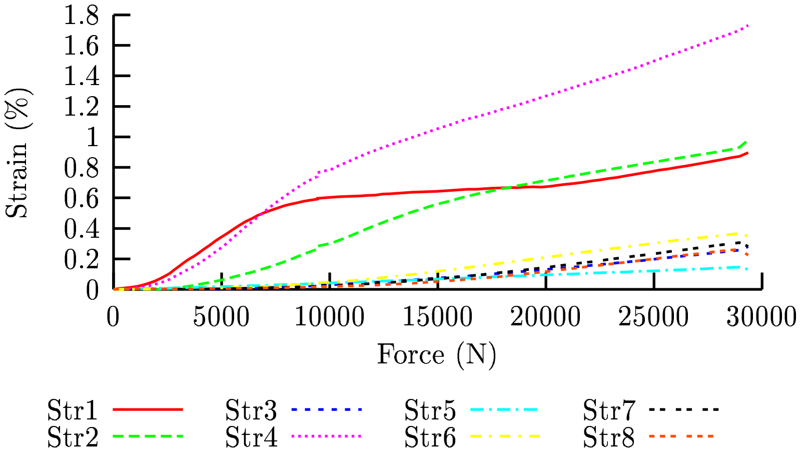

Figure 5.27: Strain results from the test plotted against time.

Gauge 1 and 2 show another interesting mechanism from the test. The strain at gauge 1 increases up to about 0.6 % before stabilizing. The strain at gauge 2, which lies 75 mm away from the centre of contact, starts to increase at about 5000 N and continue to increase during the test. This means that the area where gauge 1 is situated starts to deflect without stretching at about 9000 N, and gauge 2 which lies further away from the indentator starts to stretch. This indicates that the indentator continues to press the face sheet into the core during the entire test.

Static deflection of sandwich plates will be simulated in ANSYS later, and the simulation results will be compared to the load-deflection and strain gauge curves from the test described in this Section.

5.5.5 Visual inspection

Fig. 5.28 shows the top face of the indented sandwich plate. The facings have a $[0, 90]_S$ stacking of the laminaes, and as we have seen, the largest delamination takes place in the 0-direction. As the projectile is pressed into the plate, the upper 0-lamina gets pulled towards centre of the plate. Delamination occurs as the stress between the laminae becomes larger than the ultimate interlaminer shear stress. In the 90-direction, the upper laminae are much softer and thus less stress are introduced between the laminae resulting in little delamination. This behaviour is the same as found from the strain gauge results described in Section 5.4.8.

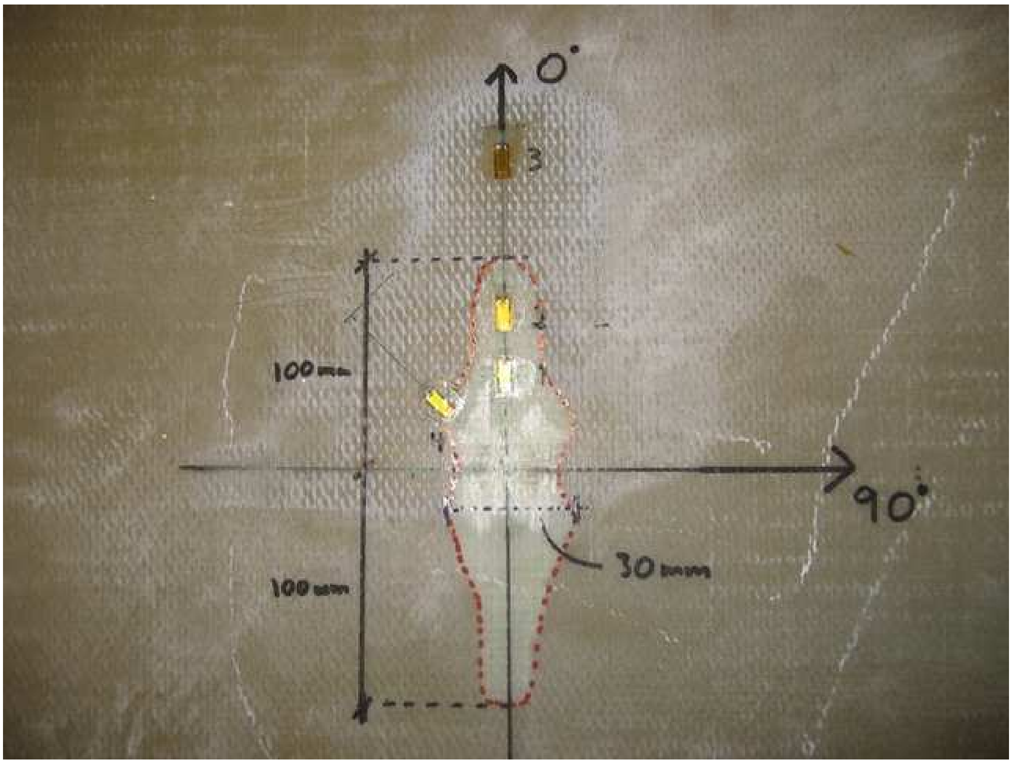

Figure 5.28: Top facing of the sandwich plate subjected to a load applied at centre of the plate. Material directions (Fibre directions) and damage area are shown.

Fibre failure also takes place in the 0-direction close to the contact area. The facing under the load gets stamped into the core, and large bending and tension stresses in the facing results in fibre failure.

5.6 4 point bending of sandwich beams

5.6.1 Introduction

The mechanical properties of the sandwich face and core materials are known from tests performed on each material separately. However, when used together in a sandwich construction, the performance of the sandwich might differ from what we expect according to theory. Therefore mechanical tests of sandwich materials are of great interest.

5.6.2 Test specifications

Two sandwich beams were tested in 4 point bending. A Schenk TREBEL RM100 Electro Hydraulic Strain Machine with 100 kN load cells was used to perform the tests. The tests were conducted according to ASTM C393 standard [20]. From this test the tensile modulus E_f and the ultimate tensile stresses σ_{fu} of the face material and the shear modulus G_c and the ultimate shear stresses τ_{cu} of the core material can be found. The test setup and machine are shown in Fig. 5.29(a). The load bearings are illustrated in Fig. 5.30. The diameter of the bearings were 50 mmand they were lowered with a rate 10 mm/min. Two tests with different spans L_1 were performed:


(a) The sandwich beam and bearings before the load is applied.
(b) The indentation of the core under the load-bearing.

Figure 5.29: Sandwich beam before and during the 4 point bending test.

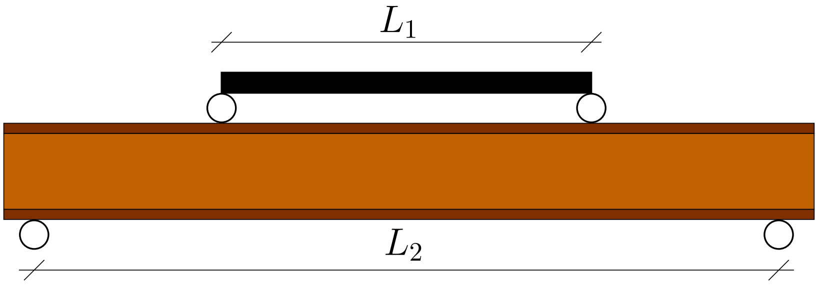

Figure 5.30: Description of the test rig measures L_1 and L_2.

Test 1: $L_1 = 1/2L_2$ and $L_2 = 1000$ mm (Quarter point bending).

Test 2: $L_1 = 1/3L_2$ and $L_2 = 1000$ mm (Third point bending).

The width b of the beams were 70 mm.

5.6.3 Instrumentation

Each beam specimen was instrumented with three 10 mm strain gauges on each facing. Fig. 5.6.3 shows the strain gauges glued to the centre of the beams. The strain gauges were connected to the logging equipment illustrated in Fig. 5.3.

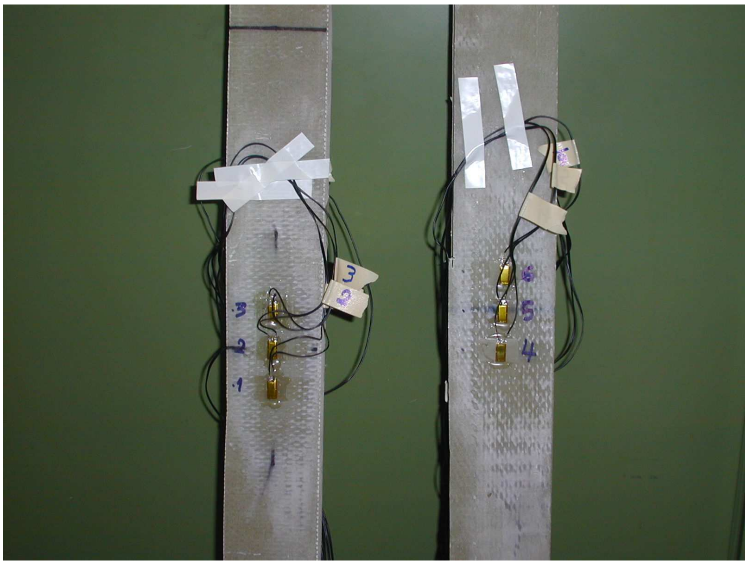

Figure 5.31: The sandwich beams instrumented with strain gauges.

5.6.4 Test results

Unfortunately, the test results were corrupted because the beams broke under the load bearings and not in the middle of the beam as predicted by theory. At an early stage of the tests everything seemed to work fine, but after a while the core was crushed under one of the load bearings. The picture in Fig. 5.29(b) is taken right before the beam broke. It clearly shows the indentation of the core under the load bearing. From Fig. 5.35 we find that the failure load was approximately 4000 N for the Quarter point load and 3000 N for the Third point loading.

A simulation of the sandwich beam in Quarter point load was performed in ANSYS. Taking advantage of symmetry, only one half of the beam was simulated. The sandwich beam is illustrated in Fig. 5.32(a) along with the element division used in the simulation. The Quarter point failure load is applied as a surface load over eight elements as shown in Fig. 5.32(b). The intensity of the surface load is thus

$$\sigma = \frac{P/2}{A} = \frac{2000 \text{ N}}{20 \times 70 \text{ mm}^2} = \frac{20}{14} \text{ N/mm}^2 = \frac{10}{7} \text{ MPa}$$

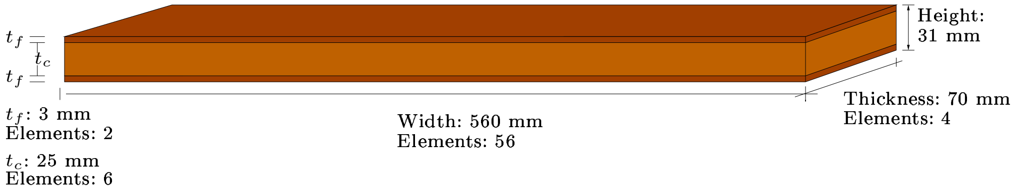

(a) Illustration of the sandwich beam.

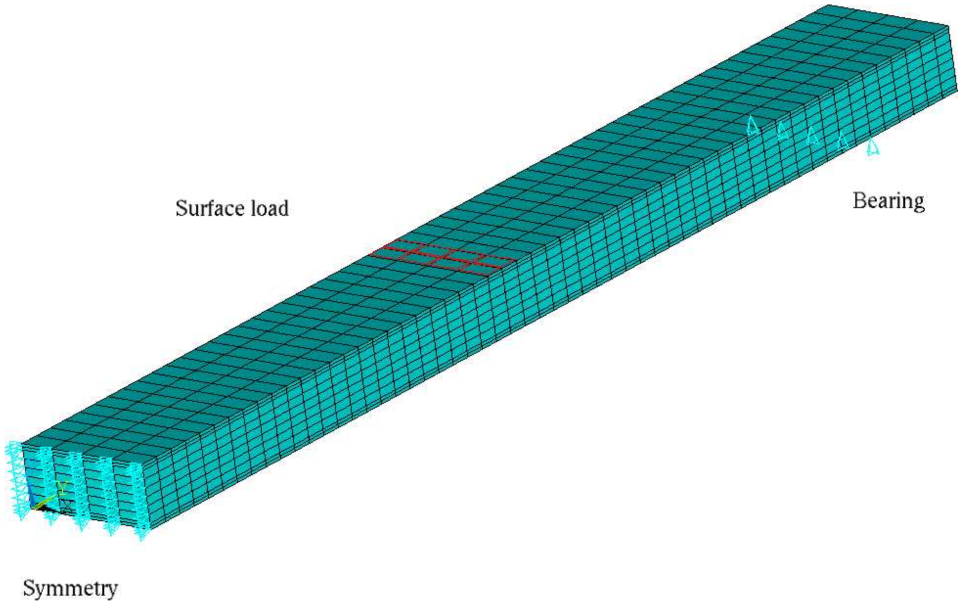

(b) Element grid used in the ANSYS simulation of the sandwich beam in Quarter point bending. Only one half is simulated due to symmetry.

Figure 5.32: Sandwich beam dimensions and mesh used in ANSYS.

The load is applied in small increments using automatic time stepping to ensure that the analysis will follow the structure‘s load-response curve. Both the core and the facings are simulated using the elastic material properties listed in Table 6.3.

From the simulation results the compressive stress in the foam under the load bearings was found to be 1.0 MPa. A plot of the transverse stresses σ_z in the part of the beam under the load bearing is shown in Fig. 5.33(a). The ultimate compressive strength of the core is 1.0-1.2 MPa according to the manufacturer [10]. Thus the simulation results also lead to the conclusion that the crushing of the core under the load bearing caused the early failure of the beam. The ANSYS simulations also showed that the faces had not reached their failure tensile strength. Fig. 5.33(c) shows the shear stresses in the beam which corresponds to the shear diagram in Fig. 3.4. The shear stresses are zero in the centre of the beam between the load bearings and constant on the sides.

The result from the centre top and bottom strain gauges in each test are plotted in Fig. 5.34. Since the gauges were placed in the middle of the beam and not under the load bearings were failure took place, the results does not give any information on maximum failure strain in the facings.

Although the ultimate tensile strength σ_{fu} of the face and the ultimate shear strength τ_{fu} of the core can not be found from the test results, it may be possible to find the tensile modulus E_f in the face and the shear modulus G_c in the core when studying the linear part of the load/deflection curve in Fig. 5.35 before failure.

5.6.5 Face tensile modulus E_f and core shear modulus G_c

From beam theory failure is supposed to take place at the centre of the beam. If we know the deflection at the centre of the beam and the applied force, we can solve the beam equations and find the flexural rigidity D and shear stiffness S as shown in Appendix B.1. The maximum deflection at the centre of the beam in Quarter and Third point bending become

$$\begin{aligned}\Delta_1 &= \frac{11}{768}\frac{P_1L^3}{D} + \frac{1}{8}\frac{P_1L}{S}\\ \Delta_2 &= \frac{23}{1296}\frac{P_2L^3}{D} + \frac{1}{6}\frac{P_2L}{S}\end{aligned} \tag{5.4}$$

and solving for D and S gives

$$\begin{aligned}D &= \frac{7}{1728}\left(\frac{P_1L^3P_2}{3P_1\Delta_2 - 4P_2\Delta_1}\right)\\ S &= \frac{7}{2}\left(\frac{P_1LP_2}{297P_1\Delta_2 - 368P_2\Delta_1}\right)\end{aligned} \tag{5.5}$$

where

P_1 = ultimate load in Quarter point benfing
P_2 = ultimate load in Third point benfing
$L = L2$, length between outer bearings

From Eq. (2.8) and Eq. (2.21) the tensile modulus of the face and the shear modulus of the core may be expressed by

$$E_f = \frac{2D}{d^2t_f} \qquad G_c = \frac{St_c}{d^2} \tag{5.6}$$

where

t_f = face thickness [mm]
t_c = core thickness [mm]
$d = t_f + t_c$, distance between the centre of the faces [mm]

In our tests we do not know the deflection at the centre of the beam, and since the failure took place under one of the load bearings, we calculate the above equations so they use the deflection under the load bearings as input:

$$\begin{aligned}D &= \frac{1}{216}\left(\frac{P_1L^3P_2}{3P_1\Delta_2 - 4P_2\Delta_1}\right)\\ S &= \frac{1}{2}\left(\frac{P_1LP_2}{40P_2\Delta_1 - 27P_1\Delta_2}\right).\end{aligned} \tag{5.7}$$

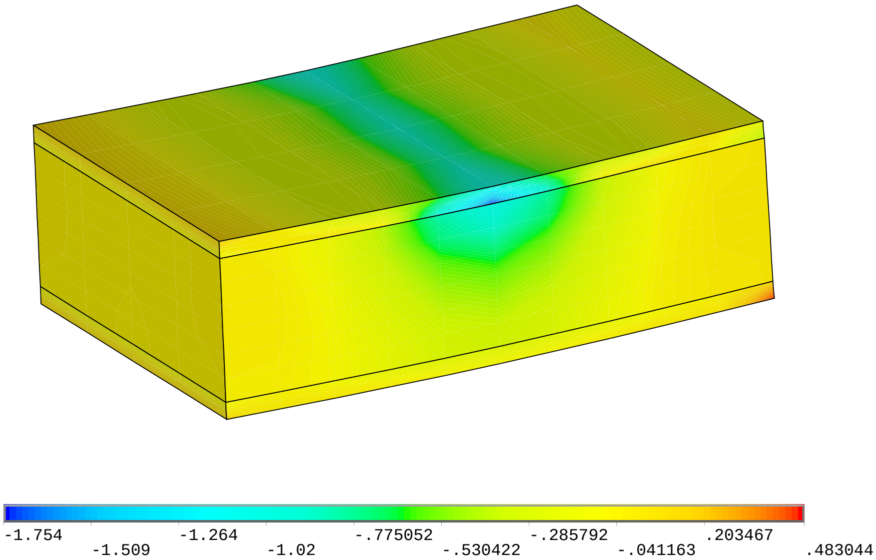

(a) Transverse stress σ_z in a section of the beam under one bearing.

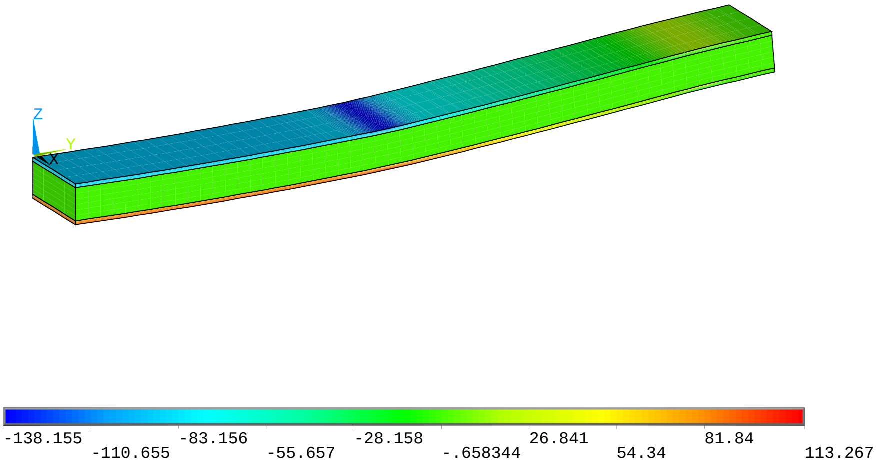

(b) Tension and compression stresses σ_y in the sandwich.

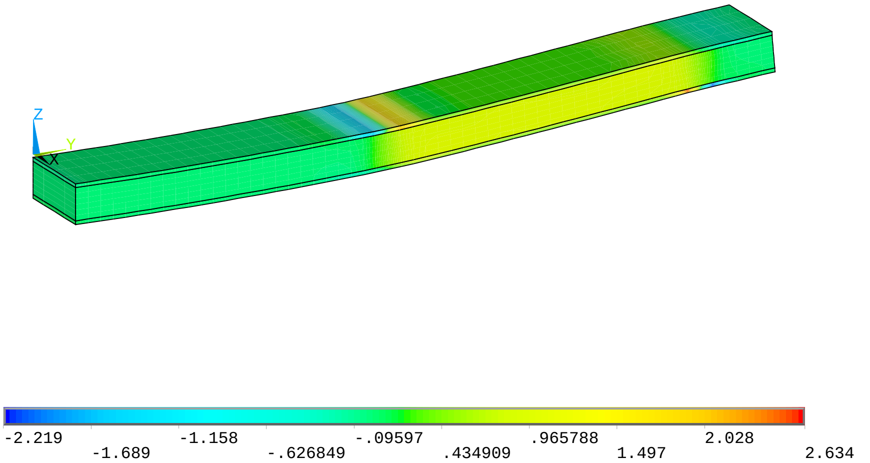

(c) Shear stress τ_{yz} in the sandwich.

Figure 5.33: Stresses in the sandwich beam at failure.

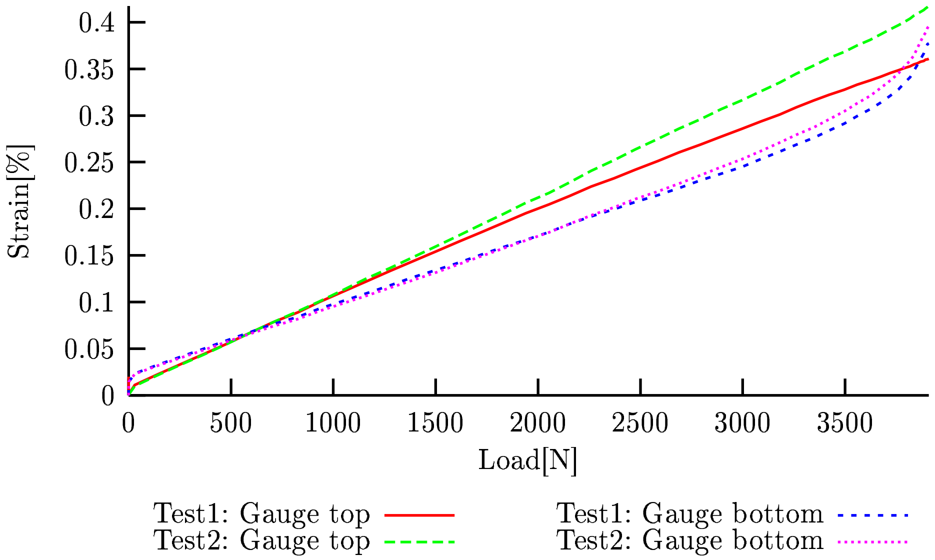

Figure 5.34: Strain vs. load. Plots of the strain in each facing at the centre of the beam.

From the machine log we can get the applied force/time curve, and since the loading velocity is known we find the deflection at the load bearings from the relation $\delta = vt$. This is shown in Fig. 5.35 where the applied load is plotted as a function of the displacement. When selecting values for the loads and deflections from the curves in Fig. 5.35, we need to make sure that the values are accurate and within the linear regime of the test. Studying Fig. 5.35 indicates that values between 18-28

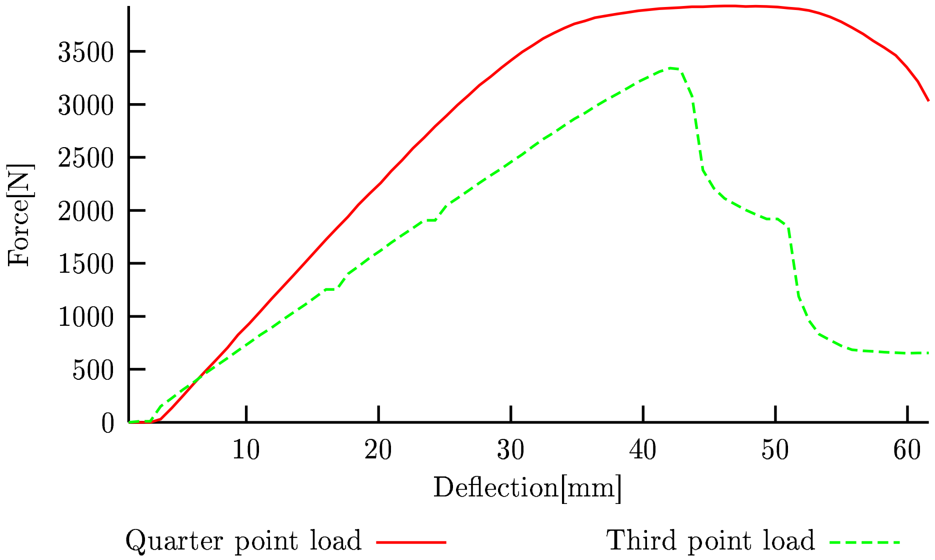

Figure 5.35: Force vs. deflection. As seen, it takes more power to deflect the beam the same distance in Quarter point loading than in Third point loading as the load bearings are closer to the middle of the beam.

mm deflection is usable, and selecting values at 20 mm deflection gives the following loads:

$$\begin{aligned}\Delta_1 = 20.94 \Longrightarrow P_1 &= 2259/b \\ \Delta_2 = 20.53 \Longrightarrow P_2 &= 1621/b.\end{aligned}$$

This gives

$$\begin{aligned}D = 63784098 \qquad &\Longrightarrow E_f = 54238 \text{ [N/mm}^2\text{]} \\ S = 275 \qquad &\Longrightarrow G_c = 9 \text{ [N/mm}^2\text{]}\end{aligned}$$

where b is the width of the beam[1]. From the Nordsandwich report [3] the face tensile modulus E_f is found to be 31500 [N/mm^2] and Divinycell, the manufacturer of the foam provides a shear modulus G_c=31 [N/mm^2]. The errors in our results are therefore

$$e_{E_f} = \frac{54238 - 31500}{31500}100\% = 72\% \qquad (5.8)$$

$$e_{G_c} = \frac{31 - 9}{31}100\% = 65\%. \qquad (5.9)$$

The main reason for these poor results are the very low normal strains in the face of the beam due to the early indentation and failure of the core. The curve inside the circle in Fig. 5.36 illustrates our force/deflection curves, while the large curve illustrates the force/deflection curve from a test without early failure due to core crushing. The measured values become very inaccurate and lead to poor results when calculating the material properties.

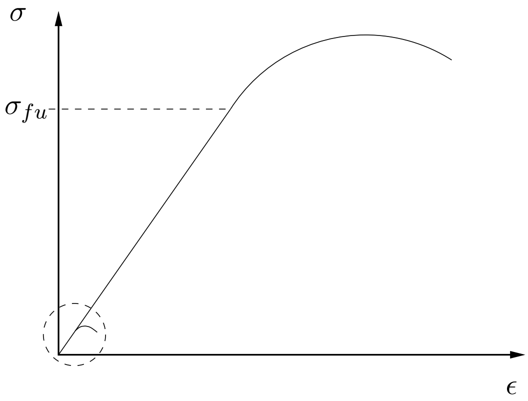

Figure 5.36: Typical σ/ϵ curve. The small part within the circle indicates the curves in Fig. 5.35.

5.6.6 Test procedure

The test outlined above contains a fast and simple procedure for determining sandwich properties based on experience from this test. The steps in the test can be written as

---

[1] Since beam theory assumes unit beam width, we have to divide the applied force with the beam width b.

1. Run numerical simulations to make some predictions on the setup of the test-rig. Try to avoid local failure by adjusting $L1$ and $L2$.

2. Perform two 4 point bending tests of sandwich beams with different spans. Log midpoint deflection and load up to failure.

3. Calculate E_f, G_c, σ_{fu} and τ_{cu} as follows

$$\begin{aligned}
E_f &= \frac{2S}{d^2 t_f} = \frac{2}{216\, d^2 t_f}\left(\frac{P_1 L^3 P_2}{3P_1\Delta_2 - 4P_2\Delta_1}\right) \\
G_c &= \frac{S t_c}{d^2} = \frac{t_c}{2\, d^2}\left(\frac{P_1 L P_2}{40P_2\Delta_1 - 27P_1\Delta_2}\right) \\
\sigma_{fu} &= \pm\frac{M}{t_f d} = \pm\frac{P(L2 - L1)}{2\, t_f d} \\
\tau_c &= \frac{P}{d},
\end{aligned}$$

where P is the failure load.

Chapter 6

Static simulations

6.1 Introduction

The main goal in this thesis is analyzing low velocity impact *dynamics* onto sandwich panels. However, analysis of sandwich panels subjected to *static* loading gives valuable information about stiffness, strength and material properties and is therefore of great interest.

The static simulations are performed with ANSYS, a commercial finite element code used in industry to solve large scale problems. ANSYS is a general-purpose program, meaning that you can use it for almost any type of finite element analysis. The program is used to find out how a given design (ea. car parts) work under operating conditions. Such programs give results cheap and fast compared to testing. You can check out "worst case scenarios" and several "what if‘s" in a short time. But testing is still required to verify the results and for calibrating the input variables in the FEM models. The analytical solutions to sandwich plate deflections derived in Section 4 have been implemented in MAPLE using the same input parameters as the ANSYS simulations, and the results are also presented here.

In this chapter are we going to simulate static deflection of sandwich plates. The sandwich plates are simulated with ANSYS and an analytical solution and the results are compared with the static compression test described in Section 5.5.

6.2 Elements and material models

6.2.1 Introduction

ANSYS provides more than 100 different element types, and each element type has a vide range of parameters and adjustable features. Sandwich panels with GRP-faces and a soft foam core are much more complicated to model than homogeneous isotropic materials such as steel and aluminium.

At first, an isotropic aluminium plate is modelled and the results are compared with an analytical solution. This aluminium plate is modelled to reassure that elements and simulation files works properly. The next step is then to start modelling sandwich plates, which are more challenging with weak core and thin faces. Due to the thin faces, many elements has to be used to maintain a reasonable ratio between the height and width in the element and simulations tend to become very expensive. It is therefore of great interest to examine how layered solid and shell elements, which have only one ore two nodes in the through thickness direction, models sandwich plates.

6.2.2 Element descriptions

A short description of the elements with illustrations in Fig. 6.2.2 and Fig. 6.2.2 are presented in this section [4]:

- SOLID45 - 3-D 8-Node Structural Solid
  - defined by eight nodes and orthotropic material properties
  - three degrees of freedom at each node: translations in the nodal x, y, and z directions
- SOLID46 - 3-D 8-Node Layered Structural Solid
  - layered version of SOLID45
  - defined by eight nodes, layer thickness, layer material direction angles and orthotropic material properties
  - three degrees of freedom at each node: translations in the nodal x, y, and z directions

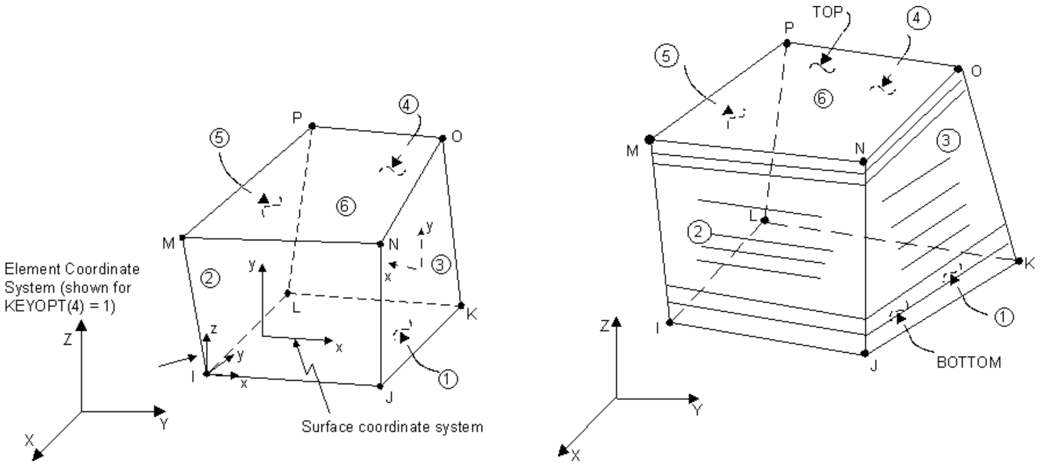

(a) SOLID45 element.

(b) SOLID46 element.

Figure 6.1: Illustration of SOLID45 and SOLID46 elements.

- SHELL91 - 8-Node Layered Structural Shell
  - defined by eight nodes, layer thicknesses, layer material direction angles, and orthotropic material properties
  - six degrees of freedom at each node: translations in the nodal x, y, and z directions and rotations about the nodal x, y, and z-axes
  - sandwich option (explained in detail later in this chapter)

- SHELL181 - 4-Node Finite Strain Layered Shell
  - defined by four nodes, thickness may be defined at each node
  - six degrees of freedom at each node: translations in the x, y, and z directions, and rotations about the x, y, and z-axes
  - models transverse shear deflection using as energy equivalence method

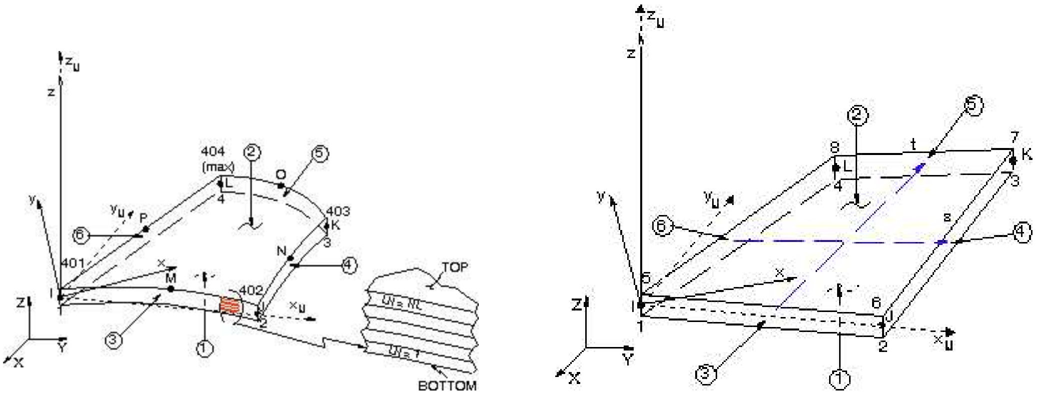

(a) SHELL91 element. As seen does the element have eight nodes.

(b) SHELL181 element.

Figure 6.2: Illustration of SHELL91 and SHELL181 elements.

These elements are used to simulate the aluminium plate described in the next chapter and the sandwich plates used in our static and dynamic tests. Due to symmetry only one quarter of the plates are simulated, as illustrated in Fig. 6.3.

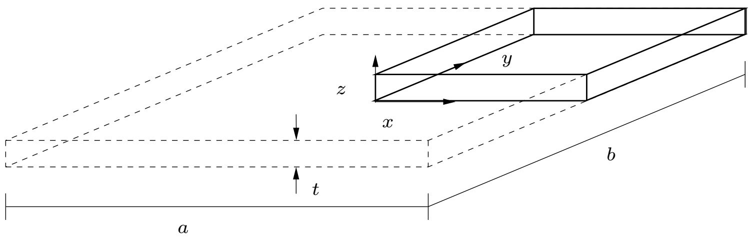

Figure 6.3: Only one quarter of the plates are modelled due to symmetry.

6.2.3 Aluminium plate

Modelling an isotropic aluminium plate subjected to static load in the through thickness direction is relatively simple, and there are only a few parameters to adjust. Table 6.1 shows the material properties and the size of the plate used in our models.

Each element model uses 20 elements in the x- and y-direction. Two elements, ie. 3 nodes are used in the through thickness direction for the SOLID45 element. The

Table 6.1: Properties of the aluminium plate.

Material properties		
Young‘s modulus	E	70000 MPa
Poisson	ν	0.3
Plate size		
Side length	a=b	125 mm
Thickness	t	1.2 mm

model using the layered SOLID46 elements has one element in the through thickness direction, and therefore 2 nodes while the layered SHELL181 and SHELL91 elements has only one node in the vertical direction. The load is applied both as a point load with magnitude 1000 N on one node and as a surface load on one element. The surface load applied becomes

$$\sigma = \frac{F/4}{A} = \frac{F/4}{\frac{a/2}{20}\frac{b/2}{20}} = \frac{1000/4\text{ N}}{(62.5/20)^2\text{ mm}^2} = 25.6\text{ N/mm}^2 = 25.6\text{ MPa}$$

and is applied at the centre of the plate.

Fraulein [9] used a simple analytical model to predict the deflection at the centre of the plate. This model, which can also be found in Roark‘s formulae for stress and strain [23], predicts the maximum deflection of a quadratic plate (a=b) with Poisson‘s ratio $\nu = 0.3$ given by

$$w_{max} = 0.0611F\frac{a^2}{Et^3}. \tag{6.1}$$

The input parameters are the same as for our ANSYS simulation resulting in maximum deflection at centre of the plate:

$$w_{max} = 0.0611 \times \frac{1000\text{ N} \times 125^2\text{ mm}^2}{70000\text{ N/mm}^2 \times 1.2^3\text{ mm}^3} = 7.89\text{ mm}. \tag{6.2}$$

Maximum deflections from each ANSYS simulation are listed in Table 6.2. As seen from the table, all the finite element results agree well with the analytical solution. This shows that our meshes have the necessary fineness and that both the solid and the less expensive shell elements give accurate results. The ANSYS input file used to calculated the element load deflections can be found in Appendix A.1

Table 6.2: Deflection of the aluminium plate.

Element	Degrees of freedom	Point load	Element load	Unit
SOLID45	3969	7.879	7.794	mm
SOLID46	2646	7.912	7.796	"
SHELL181	2646	7.821	7.942	"
SHELL91	7686	7.853	7.952	"

6.2.4 Analytical solution

Analytical models are of great interest when studying sandwich plates. After implemented in a computer, solutions are easy and fast to retrieve. The analytical solutions derived in Chapter 4 are implemented in MAPLE and solved using the same input parameters as the ANSYS simulations.

The point load Q is taken as maximum load applied in the static deflection test, Q=30000 N. This load is expressed as the Dirac delta function where the load is applied as an surface load over a small square with sides $c = a/20 = 28.5$ mm. When using the approximated solution for the load

$$q_{mn} = \frac{4Q}{ab} \sin\frac{m\pi}{2} \sin\frac{n\pi}{2},$$

the solution would not converge. In Fig. 6.4, both convergence traces for the full and the approximated load functions are plotted. The iteration is stopped when the difference between the new and previous solution is less than 0.1 %. With the

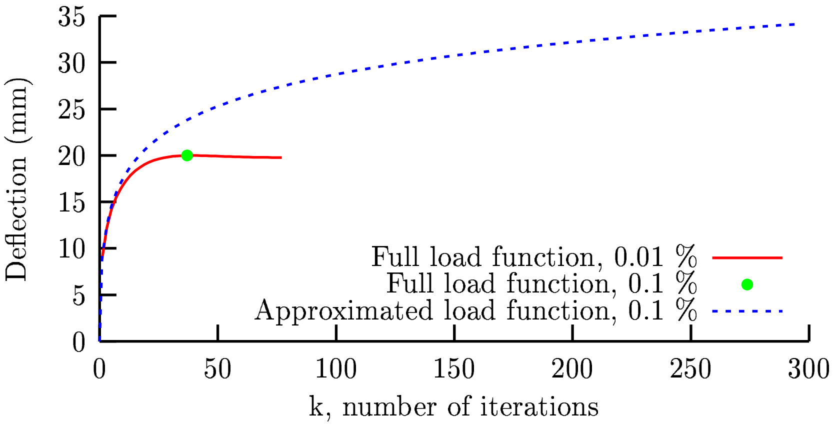

Figure 6.4: Convergence plots of solutions with load applied as an approximated and a full Dirac delta function.

full Dirac delta function used for the load, the solution converges after 37 iterations which took about 10 second to compute, while the approximated solution needed 295 iterations and took 2 hours and 15 minutes to compute. The deflection also becomes too large, and the approximated load function is therefore not used any further. The analytical solutions are compared with the ANSYS simulations in Section 6.2.6.

The MAPLE sheet used to find the deflection for sandwich plates with orthotropic plates is presented in Appendix B.3.

6.2.5 Sandwich plate with isotropic facings

Now we start modelling the sandwich plates studied in this thesis. The sandwich plates are first modelled using isotropic material properties for both the face and core, which are listed in Table 6.3 along with the plate size. The material properties for the core are given by the manufacturer while the face properties are the same used by Feuerlein [9]. According to Section 5.5, the static test is performed by pressing a

Table 6.3: Isotropic material properties and size of the sandwich plate.

Face		
Young‘s modulus	E	31500 MPa
Poissons‘ ratio	ν	0.2
Core		
Young‘s modulus	E	80 MPa
Poisson	ν	0.32
Plate size		
Side length	width	285 mm
Face thickness	t_f	3 mm
Core thickness	t_c	25 mm

hemispheric projectile into the sandwich plate lying on a steel frame. This is simulated by applying a point load and element loads on the sandwich plate modelled with simply supported boundary conditions. Fig 6.5 shows one quarter of the sandwich plate, where the number of elements used in the through thickness direction for the SOLID45 element model is shown.

The SOLID45 model contains 10 elements in the vertical direction, and 20 in the x- and y-directions. This gives 14553 degrees of freedom for the SOLID45 model, while the layered elements SOLID46, SHELL181 and SHELL91 have the same degrees of freedom as for the aluminium model. The material properties for the faces and the core are implemented in the layered element models as follows:

```
!
!T_F=Thickness face, T_C=Thickness core
!
ET,1,SOLID46   !Layered solid element
KEYOPT,1,8,1   !Store data for all layers
R,1,3,1        !Symmetric stacking
RMORE
RMORE,1,,T_F,2,,T_C
!
ET,1,SHELL181  !Layered shell element
KEYOPT,1,8,1   !Store data for all layers
SECTYPE,1,SHELL
SECDATA,T_F,1,,3
SECDATA,T_C,2,,3
SECDATA,T_F,1,,3
!
ET,1,SHELL91,3,1 !Layered shell element
KEYOPT,1,8,1   !Store data for all layers
KEYOPT,1,9,1   !Sandwich option
R,1,3,1        !Symmetric stacking
RMORE
RMORE,1,,T_F
RMORE,2,,T_C
```

The vertical load is applied on the top face as a point load with magnitude 30000

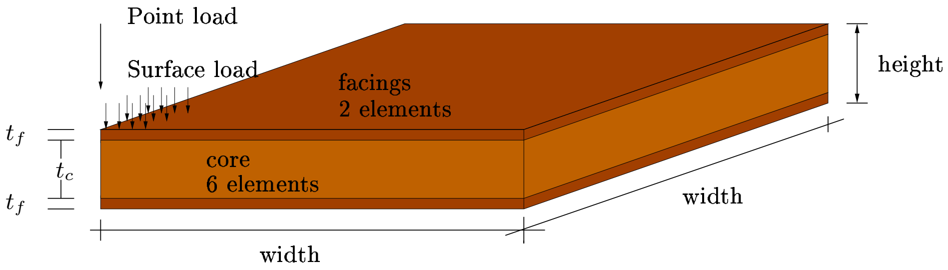

Figure 6.5: Sandwich plate modelled in ANSYS. Two elements are used in the facings and six elements in the core for the SOLID45 model.

N on one node and as a surface load over one element. The surface load becomes

$$\sigma = \frac{F/4}{A} = \frac{F/4}{(\text{width}/20)^2} = \frac{30000/4\ \text{N}}{(285/20)^2\ \text{mm}^2} = 36.93\ \text{N/mm}^2 = 36.93\ \text{MPa}.$$

The loads are applied at the mid-point of the real sandwich plates, which means that they act at the "free" corner of the simulated quarter model. This gives the deflections of the top node at (0,0) as listed in Table 6.4, where SHELL91 is used without the sandwich option. As seen, the deflection related to the point load vary a lot, while the surface load deflections are in good agreement with each other when neglecting the results obtained from the SHELL91 model. When the load is applied on a single node only, high stresses are introduced on a very local area and more elements are needed to get accurate results. Applying the load as a surface load over one element gives almost no difference between the elements. The load is now applied over more nodes, and less local effects are introduced. Fig. 6.6 shows the deflection for SOLID46 when the point load and element load is applied. As seen, the displacements connected to the vertical point load and element load are quite different.

Table 6.4: Deflection of the plate subjected to a point load and a surface load.

Element	Degrees of freedom	Point load	Element load	Unit
SOLID45	14553	22.60	19.93	mm
SOLID46	2646	42.75	21.57	"
SHELL181	2646	30.29	20.19	"
SHELL91	7686	5.02	4.53	"

The SHELL91 element model show very little deflection, which is most likely due to the weak core and that the shear stiffness of the faces dominates. SHELL91 element has an sandwich option that uses the same assumptions as our analytical models. The core is assumed to carry all the transverse shear, the facings none. Conversely, the face plates carry all of the bending load. The deflection of a sandwich beam without and with the sandwich option is illustrated in Fig. 6.7. The sandwich option gives maximum deflection 25.73 mm when the load is applied as a surface load over one element. But the sandwich option demands the core to be at least 5/6 of the total element thickness. This is not fulfilled for our sandwich plates since

$$\frac{t_c}{t_c + 2t_f} = \frac{25}{31} = 0.806 < 5/6 = 0.833,$$

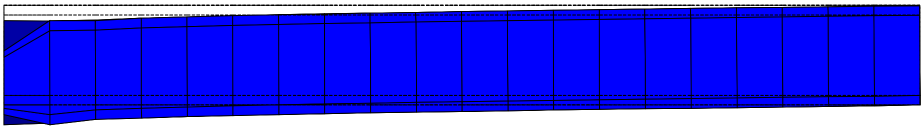

(a) Point load deflection. Large local deflection under the load.

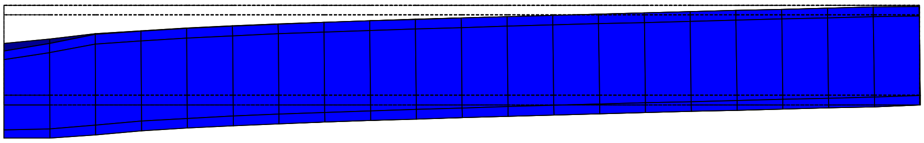

(b) Element load deflection. More global and less local deflection.

Figure 6.6: ANSYS plot of the deflection for elements situated at y=0. High local and less global deflection becomes the result when our SOLID46 element model is loaded with a point load. The surface load applied over one element gives less local indentation and more global deflection of the sandwich plate.

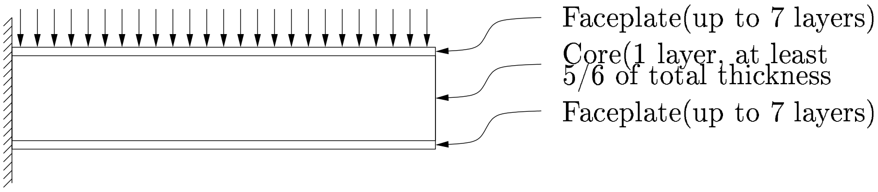

(a) SHELL91, undeformed

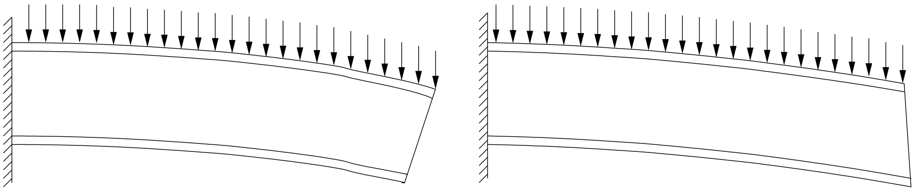

(b) Deformed shape without sandwich option (c) Deformed shape with sandwich option

Figure 6.7: Deformation of SHELL91 without and with the sandwich option. (a) illustrates the layup of a sandwich element. The core must be at least 5/6 of total thickness for the sandwich option to be used. This value is set as the limit for the assumption $t_c >> t_f$ in ANSYS.

and consequently the SHELL91 element is not used further in this thesis. The SHELL181 element models the transverse shear deflection using an energy equivalence model that makes the need for an sandwich option unnecessary.

6.2.6 Orthotropic material properties

In Section 6.2.5 the facings were assumed to be isotropic. However, the face material of the sandwich plates of consideration are in fact orthotropic. Thus, a more accurate description of the materials are listed in Table 6.5.

The maximum deflections for isotropic and orthotropic facings, when the sandwich plates are subjected to element loads are listed in Table 6.6. The differences are very small since the *in-plane* properties are the same for the isotropic and orthotropic facings, and these properties are decisive in sandwich plate bending (see Section 2.3, Approximations in the Flexural Rigidity). Nevertheless, the orthotropic material properties are used further in this section.

Table 6.5: Orthotropic material properties

Face		
Young‘s modulus	E_x	31500 MPa
	E_y	31500 MPa
	E_z	8230 MPa
Shear modulus	G_{xy}	6000 MPa
	G_{yz}	5140 MPa
	G_{xz}	5140 MPa
Major Poissons‘	PR_{xy}	0.2
Minor Poissons‘	PR_{yz}	0.2
	PR_{xz}	0.2
Core		
Young‘s modulus	E	80 MPa
Major Poissons‘	PR	0.32

Table 6.6: Comparing maximum deflections, isotropic and orthotropic facings.

Element	Degrees of freedom	Isotropic	Orthotropic	Unit
SOLID45	14533	19.93	20.03	mm
SOLID46	2646	21.57	21.63	”
SHELL181	2646	20.19	21.53	”
ANALYTICAL		19.99	24.48	”
(SHELL91)	7686	25.72	25.66	”

The SHELL91 element is not within its working range due to a two low core/face ratio, but the results are used here to compare with our analytical solution since they both uses the same assumptions. As seen are both the analytical deflections within the range from the ANSYS deflections. The full solution with orthotropic facings are very close to the solution from the SHELL91 element. This indicates that our analytical model with orthotropic facings models the sandwich with good accuracy.

The isotropic approximation on the other hand yields poor results for the midpoint deflection. In the next sections, the ANSYS models are implemented using nonlinear material properties. This is not possible to implement in the analytical solutions, and they are therefore not studied any further.

6.2.7 Yield criteria in the core and Solution

A semi-rigid PVC core with high ductility and very nonlinear material properties is used in the sandwich plates. Three compression tests were performed on our core material in a Zwick Z250 test machine and the results are plotted in Fig. 6.8. As seen, all three tests show the same behaviour. At first the compression of the core show a linear behaviour up to about 1.175 MPa, before it suddenly falls down to about 1 MPa. This means that the cell-walls in the core starts to crush, and the curve becomes nearly linear again while the cell-walls in the core continue to crush. At about 12 mm deflection, ie. at almost 50% compression strain, all the cells are compressed.

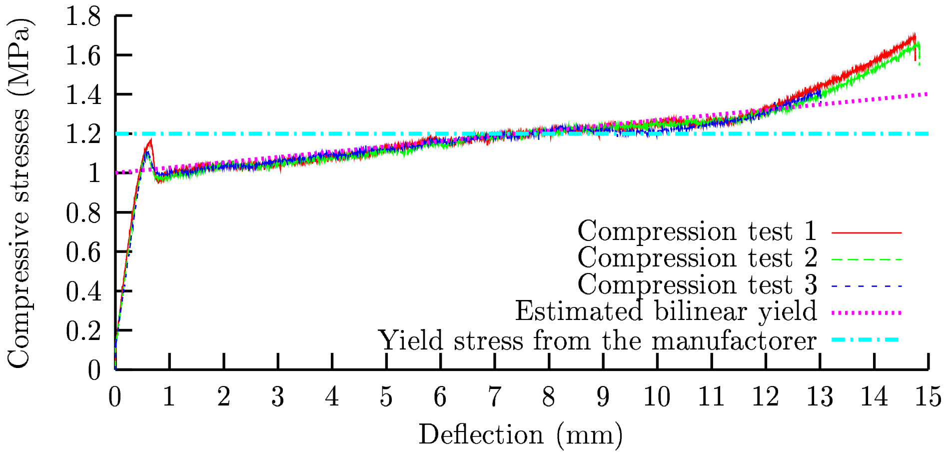

Figure 6.8: Stress-deflection curves from three compression tests of our core material. Bilinear yield criterion estimated from the test results and σ_{cu} from the manufacturer are also plotted.

A straight line at 1.2 MPa is also plotted in Fig. 6.8. This is the yield strength estimated by the manufacturer of the core material and is a bit higher than the ultimate yield stress from our compression tests. From our test data yield stress occurs at 1.0 MPa and the gradient is 0.0268.

Both the yield data from the manufacturer and our estimated yield data are implemented in ANSYS using the BISO option. This option uses the von Mises yield criterion coupled with an isotropic work hardening assumption. The material behaviour is described by a bilinear stress-strain curve starting at the origin with positive stress and strain values. The initial slope of the curve is taken as the elastic modulus of the material. At the specified yield stress, the curve continues along the second slope defined by the tangent modulus (having the same unit as the elastic modulus). The material properties are implemented as:

```
!Yield stress without hardening
TB,BISO,2
TBDATA,1,1.2 !Yield stress
TBDATA,2,0 !No hardening

!Yield stress with hardening
TB,BISO,2
TBDATA,1,1.0 !Yield stress
TBDATA,2,0.0268 !Hardening
```

When implementing the nonlinear material properties above, the solution procedure in ANSYS has to be nonlinear. The simulation is also geometric nonlinear, because the load is now applied in small steps and applied on the deformed solution. Below are the commands used to solve the nonlinear equations:

```
/SOLU            ! Entering the solution processor
ANTYPE,STATIC    ! Static analysis
NLGEOM,ON        ! Include large deformation effects
SOLCONTROL,ON    ! Use optimised nonlinear solution
                 !  defaults. Let ANSYS control most
                 !  of the parameters
NSUBST,10,100,5  ! First load step, max load step,
                 !  minimum load step
KBC,0            ! Ramped loading within a load step
AUTOTS,ON        ! ANSYS control the time step
NEQIT,100        ! Maximum number of equilibrium iterations
                 !  for nonlinear analyses
NCNV,2           ! Terminate the analysis,
                 !  but not the program execution
                 !  if the solution fails to converge
```

Both yield criteria described above are simulated using SOLID45, SOLID46 and SHELL181 elements which uses the same meshes as described in Section 6.2.5. The force-deflection traces from each simulation are plotted in Fig. 6.9. As seen, the layered shell element SHELL181 does not show any significant change in the deflection. Shell elements do not offer the possibility to model indentation and they are therefore less affected by the core compression yield criteria. The layered SOLID46 element has one element and two nodes in the vertical direction and can therefore simulate indentation. However, they are not affected by the change in the core properties. The SOLID45 model, with 10 elements in the through thickness direction show higher deflection when the core becomes softer. Layered elements are therefore less suited to model sandwich plates when local indentation of the core takes place.

6.3 Comparing ANSYS simulations with static deflection of sandwich plate

6.3.1 Introduction

Section 5.5 contains a description of a sandwich plate tested in a Schenk RM100 test machine. An indentator was pressed into the sandwich plate which was lying on a frame. The indentator and frame were the same as used in our impact tests.

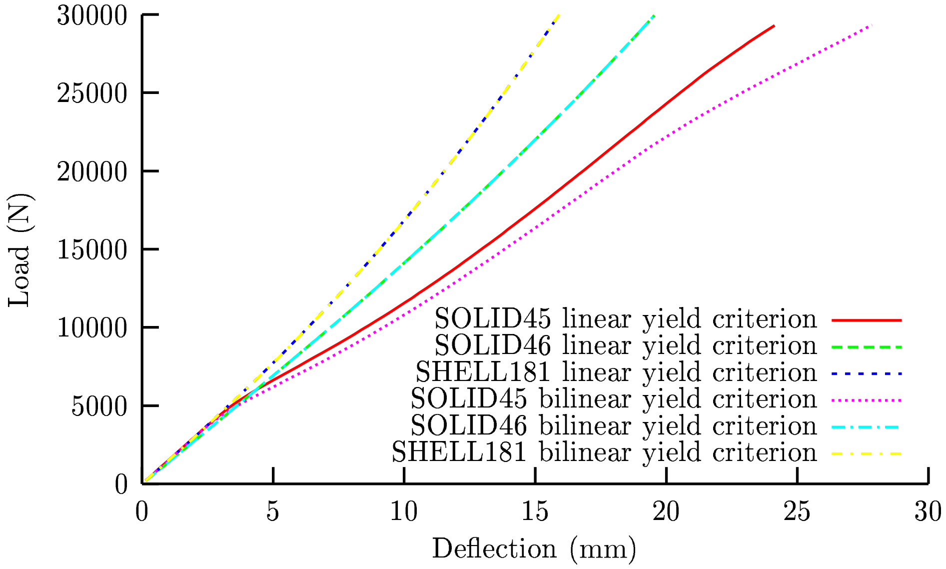

Figure 6.9: Maximum deflection with three different element types using two different yield models. The linear yield model uses a constant yield value 1.2 MPa, while the bilinear yield model uses a yield value 1.0 MPa and includes hardening.

From the static deflection test of the sandwich plate, the load-deflection trace was found along with strain gauge results from the upper and lower facing. The deflection consists of both global deflection of the entire sandwich and local indentation of the core. In the previous subsections, several different element types are shown to model sandwich plates with good results. However, the layered models are not able to simulate local indentation of the top face into the core since they only have one element and one node in the *out-of-plane* direction. The sandwich plate will therefore be simulated using the SOLID45 elements when comparing numerical predictions with the static test results.

6.3.2 Force-deflection traces

Fig. 6.10 shows the force-deflection traces from the static test and the ANSYS simulation with the estimated bilinear yield criterion as shown in Fig. 6.9. As can be seen, the deflections predicted are too small. In particular, the initial slope of the simulated force-deflection curve is too high. One reason for this could be the variation in the contact area between the projectile and plate during the test because of the hemispheric shape of the projectile. The contact area becomes larger when the projectile is pressed into the sandwich as illustrated in Fig. 6.11. This effect may be investigated by applying the load on smaller areas with higher load intensities. Four simulations are conducted with load areas varying as shown in Fig. 6.12. The width of the simulated sandwich plate is defined by Width=570/2=285 mm. The element load intensities is calculated for

$$\sigma = \frac{P}{A}.$$

where A is the contact area between the projectile and sandwich plate and P is the maximum load from the static test. A point load applied on a single node is also

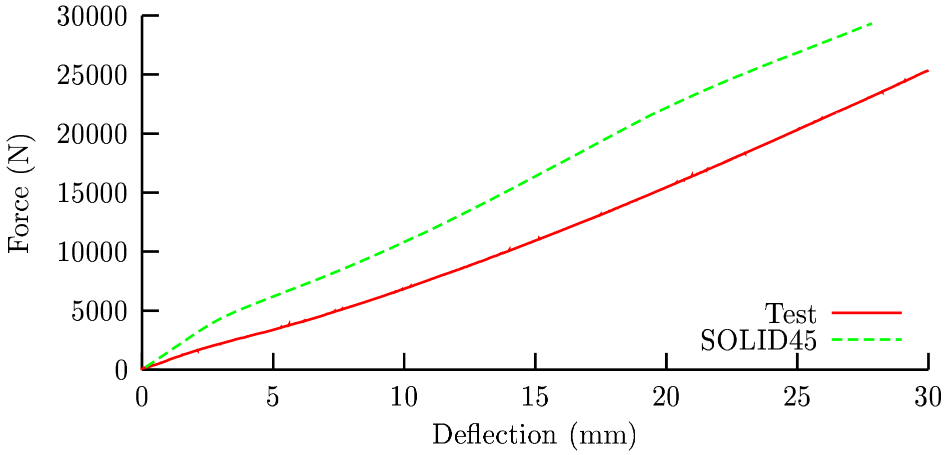

Figure 6.10: Force-deflection traces from test and simulation.

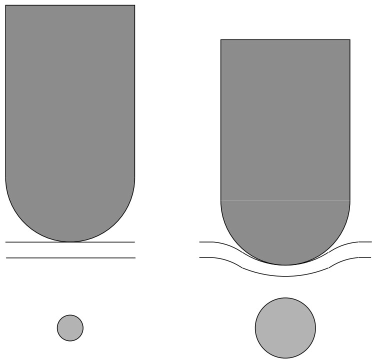

Figure 6.11: The contact area increases during the test.

simulated.

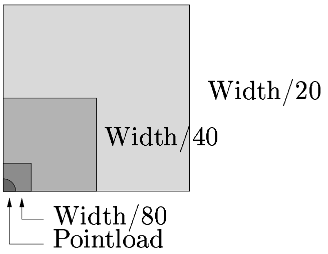

Width/20: $\sigma = 37$ MPa
Width/40: $\sigma = 148$ MPa
Width/80: $\sigma = 591$ MPa
Point load: $P = 30000$ N

Figure 6.12: Load applied over different areas.

The ANSYS models are solved by the nonlinear solution methods described in Section 6.2.7 and the foam core is modelled using the estimated bilinear Yield criterion. Each simulation uses the same grid, shown in Fig. 6.13. The lines at x=0 and y=0 are divided into 80 elements and the lines at x=285 and y=285 are divided into 20 elements. Two elements are used through the thickness of each face, while there are 6 elements in the vertical direction of the core. The lines at x=285 and y=285 are divided using a ratio 4.5, ie. the largest element is 4.5 times larger than the smallest in either the x- or y-direction. The ANSYS input file can be found in Appendix A.2.

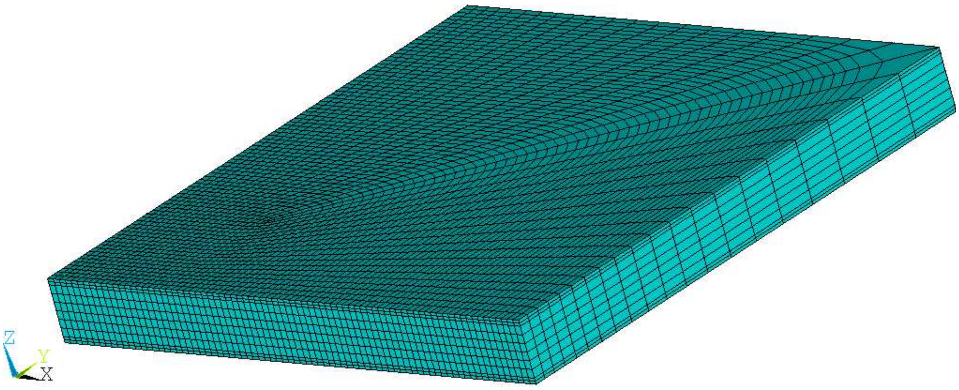

Figure 6.13: Grid used when applying the load over different areas. The coordinate system is also shown.

Fig. 6.14 shows the resulting force-deflection traces. We would expect the deflection of the centre area to increase with decreasing load area. However, this is not reflected by the ANSYS simulations. Nevertheless, the stiffness in the simulations becomes very accurate as the deflection increases. The model using a point load shows slightly higher deflection, but this is mostly due to compression of the face element where the point load is applied. This behaviour is not physical since the face material is too stiff to become compressed, and the point load model is not used further. Using failure criteria on the faces might reduce the stiffness of the simulated problem, but this is not further investigated in this thesis.

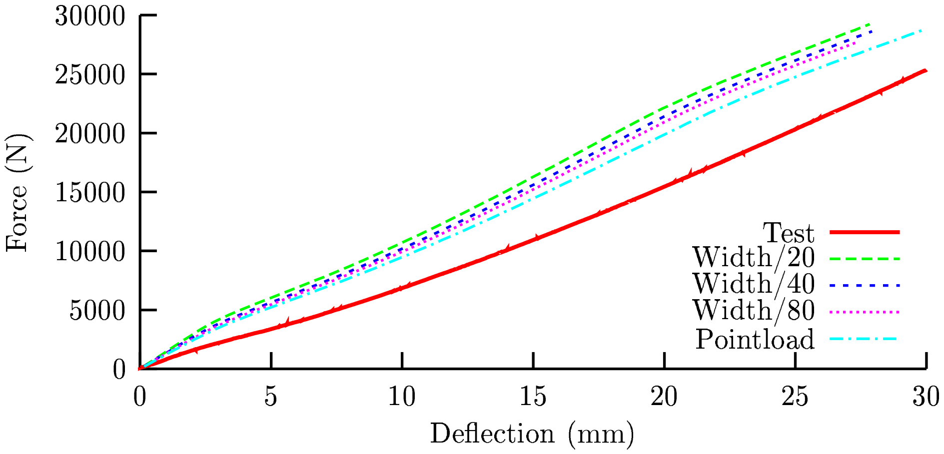

Figure 6.14: Force-deflection traces from simulations with different contact areas.

The upper and lower elements of the facings are plotted in Fig. 6.15. As can be seen the upper face is pressed into the core, and the deflection of the upper face becomes larger than the lower face. Local indentation of the sandwich is estimated by subtracting the deflections from the top and bottom face nodes. The global deflection of the sandwich plate is taken as the deflection of the bottom face. Local deflection is plotted in Fig. 6.16 along with the bottom deflection for each simulation. It is

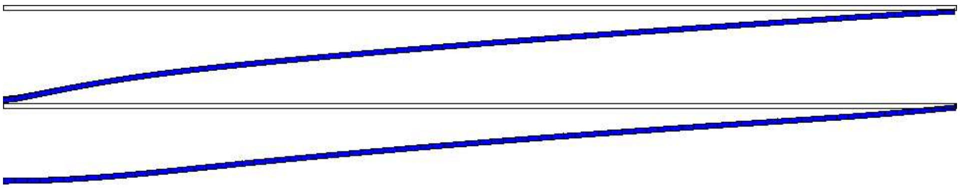

Figure 6.15: ANSYS plot of the elements at top and bottom of the sandwich plate before and after the load is applied.

seen that the bottom deflections are not affected by the load area, while the local deflections on the top face increases slightly as the load area decreases.

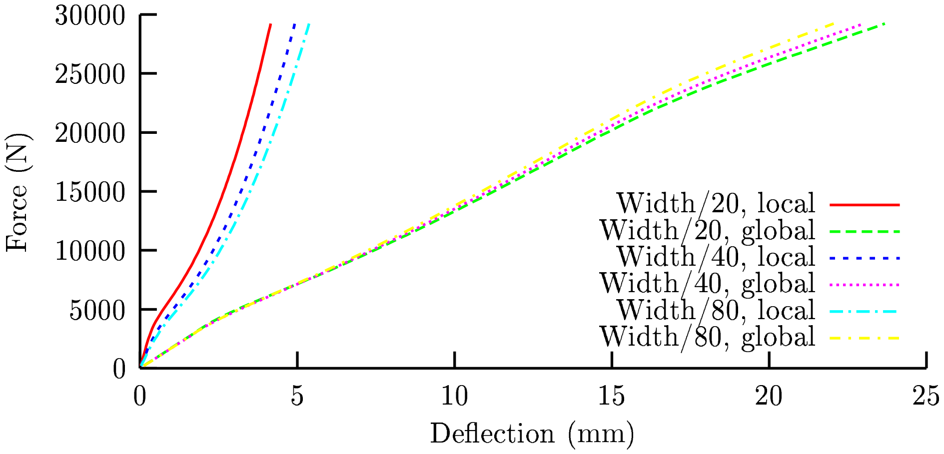

Figure 6.16: Global and local deflection. Local deflection is estimated by subtracting the upper and lower node deflection of the nodes at x=0 and y=0 while global deflection is taken as the bottom node deflection. The bottom deflection is not affected by the load area.

6.3.3 Strain gauge results

The sandwich plate tested in static deflection was instrumented with strain gauges on both faces. These values will now be compared with ANSYS simulations with load area Width/80 conducted in the previous section. The simulated strains are taken from the nodes on the upper and lower facings located at the same places as the strain gauges in the static deflection test. Fig. 6.17 shows where the strain gauges are situated on the facings.

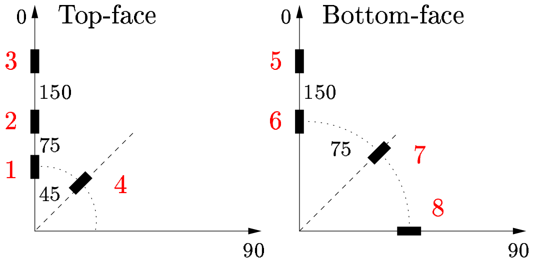

Figure 6.17: Strain gauge placement on the plate.

In the upper facing the strain gauges 1, 2 and 3 are studied. The resulting strain-force traces from the test and simulation are plotted in Fig. 6.18. It is seen that the simulated strain at gauge 1 initially are too small, but follows closely after a while. The strain at gauge 2 is much to low throughout the entire simulation, while the predicted strain at gauge 3 are in good agreement with the corresponding strain from the test.

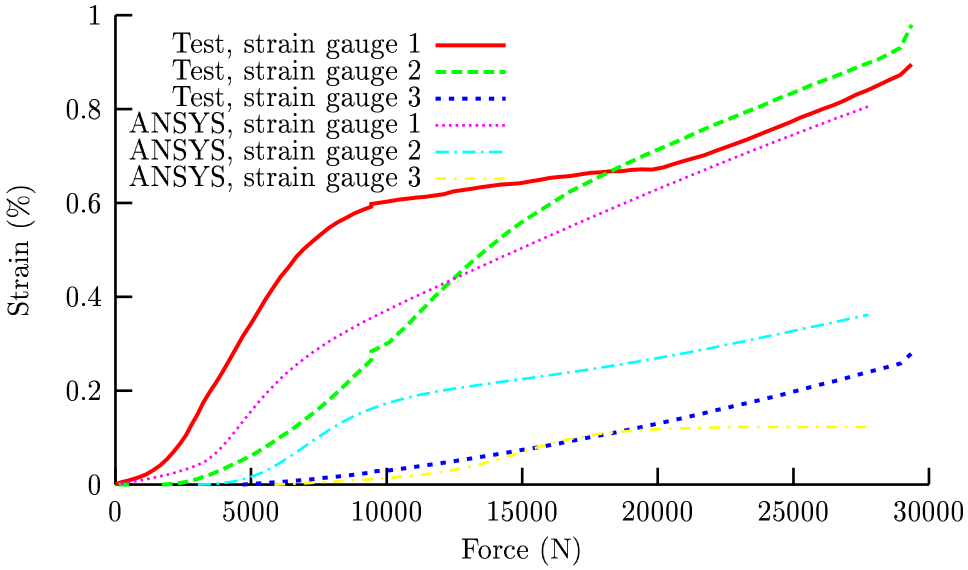

Figure 6.18: Traces of the strains from gauge 1 and 2 in the static compression test and from nodes located at the same place on the upper facing in the ANSYS simulation with load area Width/80 from the previous Section.

For the bottom facing the measured and predicted strains at gauges 5 and 6 are plotted in Fig. 6.19. The strains at the bottom facing seem to be very small, in fact the maximum strain is only about 0.4 %. Now, the simulated strain at gauge 6 is larger than the strain from the test, while the strains at gauge 5 are almost equal.

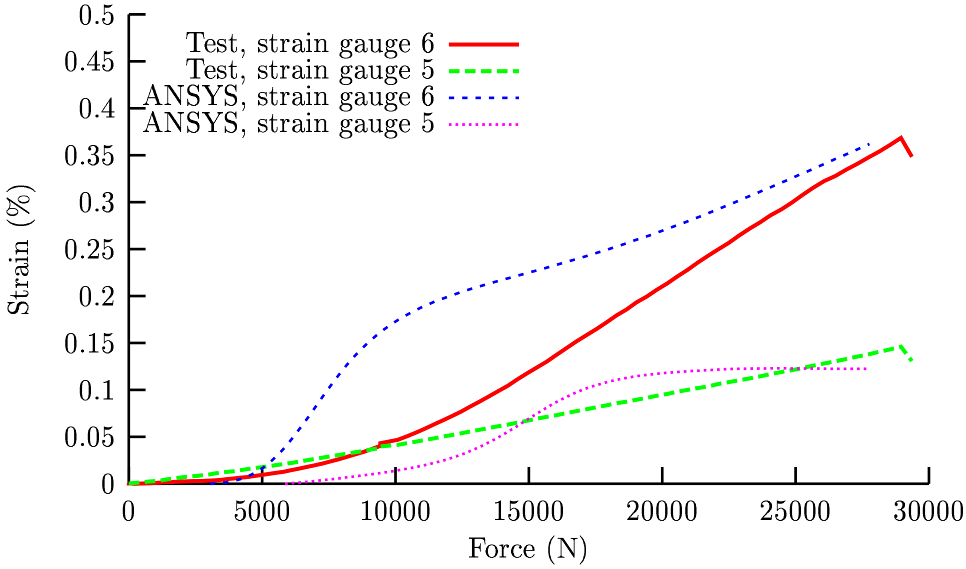

Figure 6.19: Traces of the strains from gauge 1 and 2 in the static compression test and from nodes located at the same place on the upper facing in the ANSYS simulation with load area Width/80 from the previous Section.

The layup of our facings are $[0, 90]_s$, where the subscript s indicates that only one half of the laminate is shown, with the other half symmetric about the middle plane [1]. In standard uniaxial tension tests the facings show the same strength in each material direction. However, in the static test performed in this thesis the response differs as described in Section 5.4.8. This behaviour is not reflected in the simulations and the predicted strains are therefore less accurate.

Chapter 7

Dynamic simulations

7.1 Introduction

The AUTODYN programs are general-purpose engineering software packages that use finite difference, finite volume, and finite element techniques to solve a wide variety of nonlinear problems in solid, fluid and gas dynamics. The phenomena to be studied with such programs can be characterized as highly time dependent with both geometric nonlinearities (eg. large strains and deformations) and material nonlinearities (eg. plasticity, failure, strain-hardening and softening, multiphase equations of state). AUTODYN is therefore an appropriate tool for simulating the impact dynamics of our tests.

A brief introduction to AUTODYN is presented in the next section. The simulation setup and results are studied and compared with the impact tests in Section 7.3.

7.2 AUTODYN theory

The theory presented here are based on the manuals [6] and [7] provided with the AUTODYN software.

7.2.1 Processors

AUTODYN employs a coupled methodology that allows different physical domains of a problem to be modelled with the most appropriate numerical method, and then couples these domains in space and time to provide the solution. Each numerical method are termed "processor", and the various processors are listed below:

- Lagrange (solid structures)
- Euler (gas,fluid)
- ALE (Arbitrary Lagrange Euler for specialized flow models)
- Shell (thin structural elements)
- Layered Composite Shell element in 3D (beta)

- SPH (Smooth Particle Hydrodynamics)

The numerical processors generally use a coupled finite difference/finite volume approach, and allows alternative numerical processors to be selectively used to model different components/regimes of a problem. Individual structured meshes operated on by these different numerical processors can be coupled together in space and time to efficiently compute structural, fluid, or gas dynamics problems including coupled problems (eg. fluid-structure, gas-structure, structure-structure, etc.).

In AUTODYN V4.3, all the above processors use explicit time integration. To ensure a stable and reasonable solution, some restrictions has to be applied on the time-step of integration. The value of this time step depends on several parameters of the numerical method and solution so the local time step ensuring stability is calculated for each mesh point. The minimum value of all these local values is multiplied by a safety factor (currently a default value of 2/3 is built into the code) and this is chosen as the time step for the next update. In a Lagrangian mesh the time step must satisfy

$$\Delta t = \frac{d}{c}$$

where d is a typical length of a zone (defined as the volume of the zone divided by the square of the longest diagonal of the zone and scaled by 2/3) and c is the local sound speed. This ensures that a disturbance does not propagate across a zone in a single time step.

Lagrange Processor A Lagrangian coordinate system, in which the coordinates move with the material, is ideal for following the flow in regions of relatively low distortion, and possibly large displacement, where mesh tangling, if it does occur, will only occur at later times and in regions of low to moderate pressure gradients. The Lagrange coordinate system can accurately follow particle histories, and therefore accurately define material interfaces and also follow stress histories of material in elasticplastic flow. Materials are defined on a structured (I, J, K) numerical mesh of six sided bricktype (hexahedral) elements and the eight vertices or nodes of the mesh move with the material flow velocity. Material remains within its initial element definition with no transport of material from cell to cell.

The partial differential equations to be solved express the conservation of mass, momentum and energy in Lagrangian coordinates. These, together with a material model and a set of initial and boundary conditions, define the complete solution of the problem. Material associated with a Lagrangian zone stays with that zone under any deformation. Thus a Lagrangian grid moves and distorts with the material it models and conservation of mass is automatically satisfied.

The main drawback with Lagrange mesh is that for severe deformations the numerical mesh may become overly distorted with a resulting small timestep and possible loss of accuracy. However, AUTODYN has included some features who deals with this situations. In 2D only, a rezoning utility allow a re-establishment of a "regular" mesh through mapping of the distorted mesh quantities onto a newly zoned mesh. Another feature is the erosion option which allow the user to specify a limit for the strain in an element. When this limiting strain is reached, the element is eroded, ie. transformed from a solid element to a free mass node disconnected from the original mesh thereby avoiding the mesh distortion problem.

Shell Processor For thin structures, the solution may become prohibitively expensive as the timestep due to small elements through the thickness becomes very small. To overcome this problem a shell processor is introduced assuming:

- The normal stress through the thickness is neglectable, thus a biaxial stress distribution exists
- A line initially normal to the of the shell remains straight and normal to the deformed mid surface as the shell deforms (ie. transverse shear is neglected).
- The density of the shell is assumed to remain constant so there is no volume change during deformation of the shell. As a consequence, significant changes in the shell thickness can occur during plastic deformation.

This processor is not suited for modelling sandwich plates, since neglecting transverse shear in the core can not be allowed without loosing accuracy. However, modelling the faces with shell elements and joining them with a core modelled with Lagrange elements might give good results, but are not further examined here.

Layered Composite Shell Element In AUTODYN v4.3 a layered composite shell has been implemented, but for the same reasons as above, it will not be further examined in this thesis.

Interaction AUTODYN has the ability to couple numerical grids across Lagrange-Lagrange and Lagrange-Euler interfaces. When two subgrids are defined to interact (Lagrange-Lagrange interfaces in this thesis), then at each time step all surface nodes of the target are tested to see if they have penetrated any of the impacting faces during the current time step. If any of the target nodes would penetrate, momentum conserving interactions are computed to prohibit penetration. When this is completed the surface nodes of the impacting faces are tested for penetrating the target faces, providing symmetry to the process.

If the pre-defined strain is exceeded, the erosion algorithms allow a Lagrangian cell to be removed from the calculations. When a cell is eroded, the mass of the cell can either be discarded or retained at the corner nodes of the cell. If the mass is retained, conservation of inertia and spatial continuity of inertia are maintained during the erosion process. If the retained inertia option is used and the cells surrounding a particular node are eroded, the node becomes a free node. This node can continue to interact, and load other bodies.

Erosion does not necessarily simulate a physical phenomenon. It is basically a numerical technique introduced to overcome the problems associated with mesh distortions caused by gross motions of a Lagrangian grid. Typical erosion strains are taken to be in excess of 150%. Because of the losses of internal energy, strength and (possibly) mass, care must be taken in using this option and erosion strain limits chosen wisely so that cells are not discarded (eroded) until they are severely deformed and their compressive strength and/or mass are not likely to affect the overall results.

7.2.2 Material properties

Four basic types of information must be specified for each material:

Equation of State: Pressure as function of density and internal energy.

- *Linear:* A bulk modulus and reference density are defined.
- *Orthotropic:* Used to model anisotropic (orthotropic) materials.

Strength model: Strength model which defines the yield surface.

- *None (Hydro):* No yield surface and no shear modulus. Material is a strengthless fluid.
- *Elastic:* No yield surface. A constant shear modulus is defined.
- *Von Mises:* A constant yield surface and shear modulus are defined.
- *Johnson Cook:* Strain hardening model. Strain rate and temperature dependent.
- *Piecewise linear:* Strain hardening model. Modified Johnson-Cook with piecewise linear function of yield stress.

Failure model: Failure model prescribing when the material no longer has strength.

- *None:* The material will never fail.
- *Hydro:* A hydrostatic tensile stress. If this negative pressure is reached failure occurs.
- *Bulk strain:* If the effective plastic strain in the material exceeds the ultimate bulk strain limit, failure occurs.
- *Principal stress:* Failure is initiated if the maximum principal stress, or the maximum shear stress, exceed their respective failure stresses.
- *Principal stress/Principal strain:* Failure is initiated if the maximum principal stress or strain, or the maximum shear strain or stress, exceed their respective failure limits.
- *Material stress:* Principal material stress failure. The principal directions are defined by the principal material directions. This model is useful for materials which fail along predefined material planes, such as where delamination failure

Erosion model: Erosion criteria. When a material is eroded it is transformed from a solid element to a free mass node (Lagrange only).

- *None*
- Instantaneous Geometric Strain: Geometric strain is defined solely by element deformation and is not dependent on material properties. Used in situations where elastic oscillations tend to monotonically inflate the value of the geometric strain.

7.3 AUTODYN impact simulations

7.3.1 Energy law

The projectile used in our dynamic tests weights 6.2 kg and is dropped from 3.0 m and 3.5 m. Neglecting the friction from the tube walls and from the air allows us to use the energy law $E_p = E_k$. This energy law gives us the relation between the velocity, dropheight and kinetic energy of the impactor as follows:

$$\begin{aligned} E_p &= E_k \\ mgh &= \frac{1}{2}mv^2 \\ h &= \frac{E_k}{mg} = \frac{v^2}{2g} \\ v &= \sqrt{2gh} \end{aligned}$$

The velocity and kinetic energy of the projectile as it hits the sandwich plate becomes:

$$\begin{aligned} \mathrm{h} &= 3.0 \text{ m} \Longrightarrow \mathrm{v} = 7.7 \text{ m/s and } E_k = 182.4 \text{ J} \\ \mathrm{h} &= 3.5 \text{ m} \Longrightarrow \mathrm{v} = 8.3 \text{ m/s and } E_k = 212.8 \text{ J.} \end{aligned}$$

7.3.2 Input parameters

Taking advantage of the symmetry, only one quarter of the plate and projectile is modelled. The simulated sandwich plate have dimensions [285x285x31] mm^3 (one quarter of the tested plate).

Projectile and Frame properties The projectile has radius 3.75 cm and height 18.75 cm. AUTODYN takes the density as input and since the modelled projectile must have the same weight as the projectile used in the tests the density is calculated from $\rho = m/V$, where V is the volume and m=6200 g is the mass of the projectile used in the tests. The volume is calculated as

$$V = \pi r^2 h + \frac{1}{2}\frac{4}{3}\pi r^3 = \pi \times 3.75^2 \times 15 + \frac{2}{3} \times \pi \times 3.75^3 = 773.1 \text{ cm}^3$$

and the density becomes

$$\rho = \frac{m}{V} = \frac{6200 \text{ g}}{773.1 \text{ cm}^3} = 8.02 \text{ g/cm}^3.$$

Fig. 7.1(a) shows the mesh used to model the projectile. The frame is modelled as two half cylinders with radius 20 mm. Each node in the frame is clamped, and the mesh is shown in Fig. 7.3.2. The projectile and frame are modelled using material properties for stainless steel and the same grids are used in all the simulations. Table 7.1 lists the properties as they are given in AUTODYN.

Face properties The faces consist of two multiaxial GRP-laminates with symmetric layup and the thickness of each face is 3 mm. The layup of one face is illustrated in Fig. 7.2 and the material properties given by Feuerlein [9] are listed in Table 7.2.

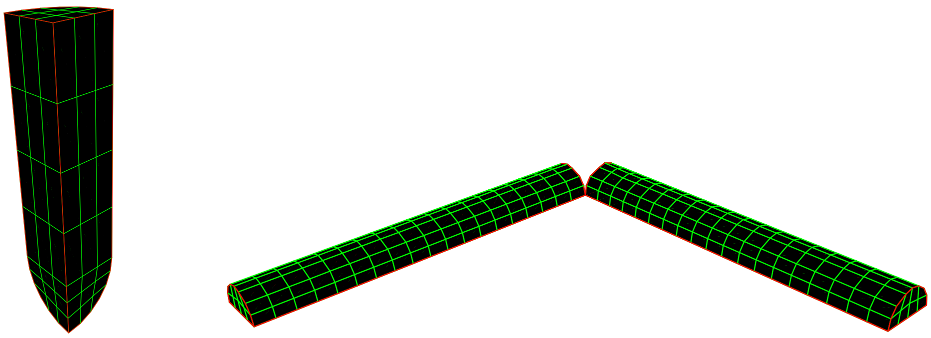

(a) Mesh used to model the projectile.

(b) Mesh used to model the frame.

Figure 7.1: Plot of the meshes used in the projectile and frame.

Table 7.1: Projectile and Frame properties

	Projectile/Frame:	**Unit:**
Equation of state:	Linear	-
Strength Model:	Elastic	-
Failure Model:	None	-
Erosion Model:	None	-
Reference density:	7.90500E+00	g/cm^3
Bulk Modulus:	4.01300E+08	kPa
Ref. Temperature:	0.0	K
Specific Heat:	0.0	J/kgK
Shear modulus:	8.70000E+07	kPa

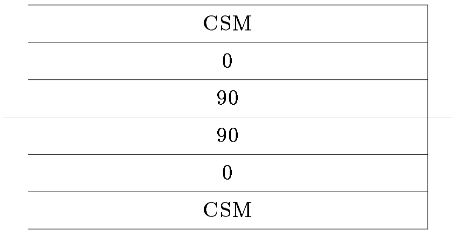

Figure 7.2: Symmetric layup of multiaxial GRP-laminates. A thin layer of CSM (Cutted Straw Mat) are used to protect the load carrying fibres underneath.

Table 7.2: Face properties

Strength Properties			**Failure Properties**		
Young‘s modulus E_x:	31500	MPa	Tensile Failure Stress σ_x:	482.0	MPa
Young‘s modulus E_y:	31500	”	Tensile Failure Stress σ_y:	482.0	”
Young‘s modulus E_z:	8230	”	Tensile Failure Stress σ_z:	65.0	”
Poisson‘s ratio ν_{xy}:	0.2		Shear Failure Stress τ_{xy}:	55.9	”
Poisson‘s ratio ν_{yx}:	0.2		Shear Failure Stress τ_{yz}:	30.0	”
Poisson‘s ratio ν_{zx}:	0.2		Shear Failure Stress τ_{zx}:	30.0	”
Shear Modulus G_{xy}:	6000.0	MPa	Tensile Failure Strain ϵ_x:	2.2	%
Shear Modulus G_{yz}:	5143.6	”	Tensile Failure Strain ϵ_y:	2.2	”
Shear Modulus G_{zx}:	5143.6	”	Tensile Failure Strain ϵ_z:	3.87	”
Density ρ:	1.9785	g/cm^3	Shear Failure Strain γ_{xy}:	4.0	”
			Shear Failure Strain γ_{yz}:	4.0	”
			Shear Failure Strain γ_{zx}:	4.0	”

Core properties Divinicell H80 is an advanced polymer foam used in the construction of high performance cored laminates. It provides the right combination of strength, stiffness, temperature resistance and buoyancy with little weight. The material properties are listed in Table 7.3 and are provided by the manufacturer [10].

Table 7.3: Core properties

Strength and Failure Properties			
	Compression	Tension	
Young‘s modulus E:	85	80	MPa
Failure Stress σ:	1.2	2.2	MPa
Shear Modulus G:	31		MPa
Poisson‘s ratio ν:	0.32		
Density ρ:	0.08		g/cm^3

7.3.3 Face and Core material modelling

The facings are modelled using the orthotropic material properties listed in Table 7.2 and are implemented using the following models:

```
EQUATION OF STATE: Orthotropic
   STRENGTH MODEL: Elastic
    FAILURE MODEL: Material Stress/Strain
    EROSION MODEL: None
```

Since the GRP-facings are very brittle, only an elastic strength model is implemented assuming perfectly elastic behaviour of the facings up to failure. Failure values are found from testing in the material directions of the facings and a Material Stress/Strain failure model is therefore used. The facings have a 0-90 multilayered layup with the material directions corresponding to the global directions of the sandwich. The erosion model is not used since no penetration takes place in the impact tests. Appendix C.1 shows how the facings are implemented in AUTODYN.

The core is made of a isotropic foam with material properties as shown in Table. 7.3 and is implemented in AUTODYN as follows:

```
EQUATION OF STATE: Linear
   STRENGTH MODEL: Vonmises / Johnson-Cook / Piecewise linear
    FAILURE MODEL: Principal stress
    EROSION MODEL: None
```

Three strength models are used to model the core, Von Mises, Johnson-Cook and a piecewise linear version of Johnson-Cook.

The Von Mises yield criteria assumes that the material deforms elastic-perfectly plastic. In a three-dimensional state of stress the Von Mises yield criterion is given by

$$\sigma_e = \frac{1}{\sqrt{2}} \left[(\sigma_1 - \sigma_2)^2 + (\sigma_2 - \sigma_3)^2 + (\sigma_3 - \sigma_1)^2 \right]^{1/2} .$$

When σ_e reaches σ_Y, the yield stress in simple tension, the materials is deemed to have yielded. The compressive failure stress provided by the manufacturer is taken as the yield criteria in this model.

The Johnson-Cook model makes the yield function a function of material properties without excessively complicating the resultant calculations. It also includes hardening effects and the yield stress is given by

$$\sigma_e = \left[A + B\epsilon_p^n \right] \left[1 + C \log \dot{\epsilon}_p \right] \left[1 - T_H^M \right] ,$$

where

ϵ_p = effective plastic strain
$\dot{\epsilon}_p$ = normalised effective plastic strain
T_H = homologous temperature = (T - T$_{room}$)/(T$_{melt}$ - T$_{room}$) = 0 in our case
A = basic yield stress
B = strain hardening.

By approximating the stress-strain curves from the compression tests of the core shown in Fig. 6.8, the following parameters were found:

$$\begin{aligned} A &= 116.40 \text{ MPa} \\ B &= 839.27 \text{ MPa} \\ C &= 0 \\ n &= 0.1453. \end{aligned}$$

The piecewise linear model is a modification of the Johnson-Cook model where the dependence on the effective plastic strain $(A + B\epsilon_p^n)$ is replaced by a piecewise linear function of yield stress Y versus effective plastic strain ϵ_p. Again are the stress-strain curves in Fig. 6.8 approximated, and a line between the points

$$\begin{aligned} \epsilon = \quad 0, \quad \sigma_Y = 1000 \\ \epsilon = \quad 15, \quad \sigma_Y = 1402 \end{aligned}$$

is used to model the yield.

Appendix C.2 shows how the material properties of the core are implemented in AUTODYN.

7.3.4 Strength models in the core

The three core failure models described above is simulated using the grid shown in Fig. 7.3. As seen, a uniform grid with 10 elements in the height and 31 elements in the width is used to model the sandwich. The thickness of the whole sandwich plate is 31 mm and each face is 3 mm. With 10 elements in the height, the thickness of each element becomes 3.1 mm and thus, the elements at top and bottom of the sandwich plate are given face properties and the elements in-between are given core properties. The results are compared with the data from the impact onto the first plate which were conducted from 3.0 m. The velocity and kinetic energy of the projectile as it hits the plate is therefore 7.67 m/s and 182.3 J.

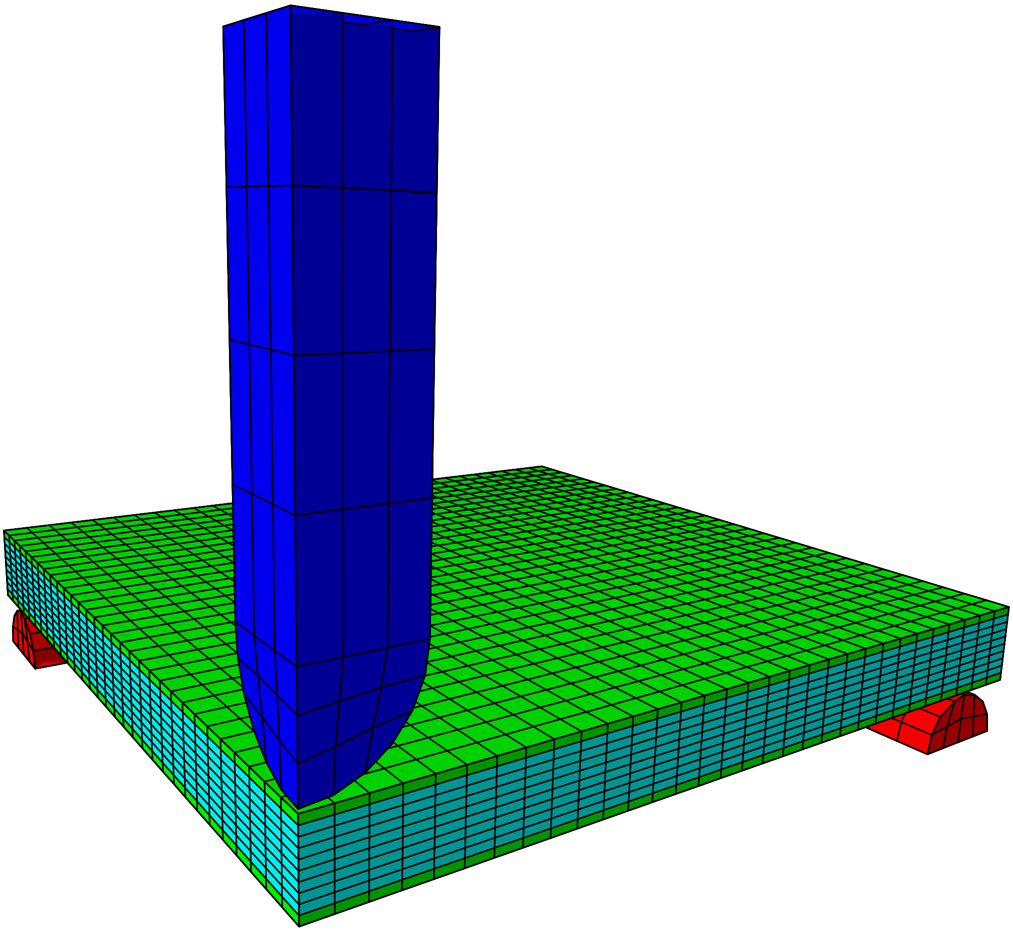

Figure 7.3: Figure of the uniform grid used in the simulations where the traces in Fig. 7.3.4 were calculated. The sandwich has a uniform grid with 10 elements in the height and 31 elements in the width.

The figures 7.4(a) and 7.4(b) shows how the various failure modes for the core compare to the tested values in kinetic energy and deflection. The kinematic energy and deflection from the test were found by integrating the acceleration test data numerically as described in Section 5.4.6.

As seen in the figures the simulations with core models approximated from our

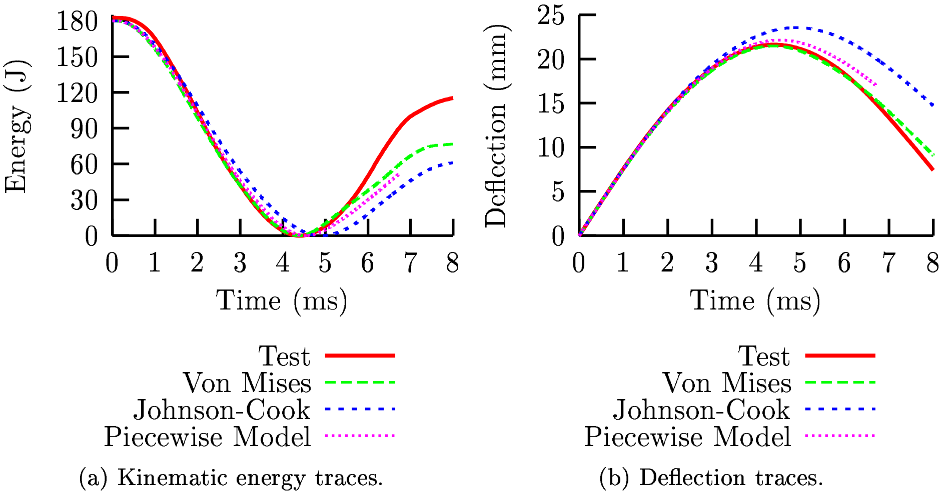

(a) Kinematic energy traces.

(b) Deflection traces.

Figure 7.4: Plots of the kinematic energies and deflections from the test and the simulation with various failure modes in the core. The acceleration data used to find the kinematic energy and deflection are from the impact onto plate one.

compression tests are slightly too soft. Less kinetic energy is returned to the projectile at the end of the impact because more energy is used as plastic work in the sandwich core as shown in Fig. 7.5. The deflection of the projectile also becomes to large.

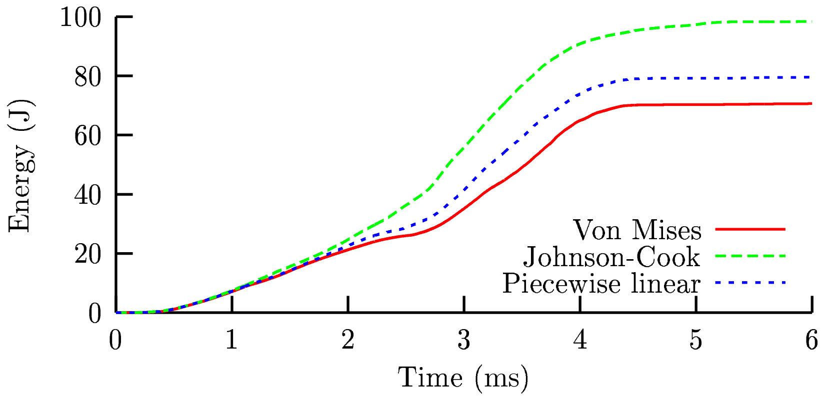

Figure 7.5: Plastic work in the sandwich panel simulated with three different strength models for the core. At about 4.5 ms, when the projectile leaves the sandwich plate, no more plastic work are conducted.

However, the Von Mises yield criteria models the test data very accurate, and this failure model is therefore used further.

7.3.5 Failure models in the facings

The above simulations were conducted with the `Material Stress/Strain` failure model in the facings. To find out how our material failure properties in stress and strain agree with each other, simulations were also conducted with failure models `Material`

Stress and Material Strain. The kinematic energy and deflection of the projectile is plotted in Fig. 7.6(a) and Fig. 7.6(b). It is seen that the difference in the stress and strain failure criteria result in small changes in the results. The curves from the Material Stress/Strain and Material Stress show the exact same results and failure occurs therefore when the stress criterions are reached. However, the Material Stress/Strain failure criteria for the facings is used further.

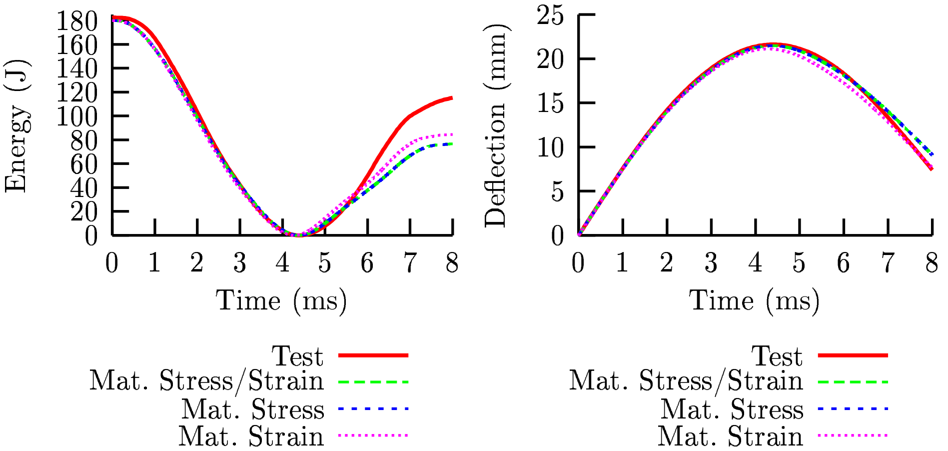

(a) Kinematic energy traces for the failure models used in the face.

(b) Deflection traces for the failure models used in the face.

Figure 7.6: Plot of the kinematic energy and deflection of the projectile from the test and three simulations using failure models Material Stress/Strain, Material Stress and Material Strain.

One large simulation was conducted using the Von Mises yield criteria in the core and the Material Stress/Strain failure criteria in the facings. Now the grid have 20 elements in the height and 62 in the width as shown in Fig. 7.7, and the results are compared with a simulation using the grid in Fig. 7.3 and the same material properties. The kinetic energies and deflections from the simulations and the test are

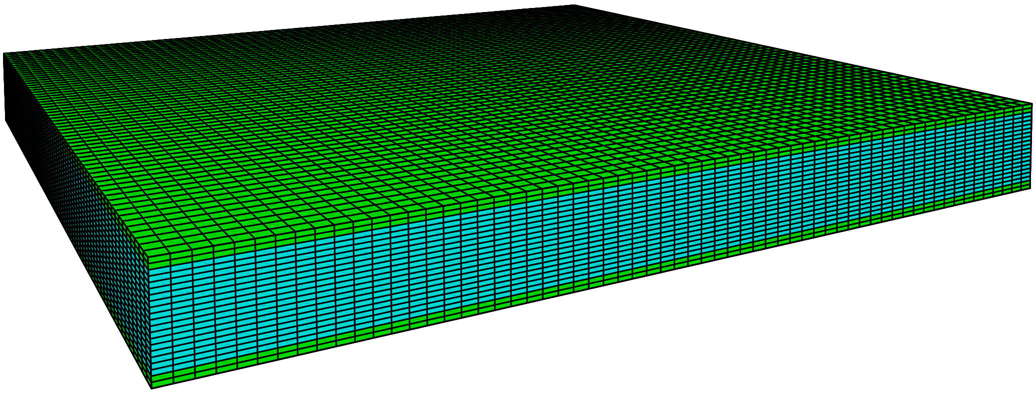

Figure 7.7: Large grid used to simulate sandwich plates. 20 elements in the height and 62 elements in the width.

plotted in Fig. 7.8. It can be seen that the small and large grid simulations show a

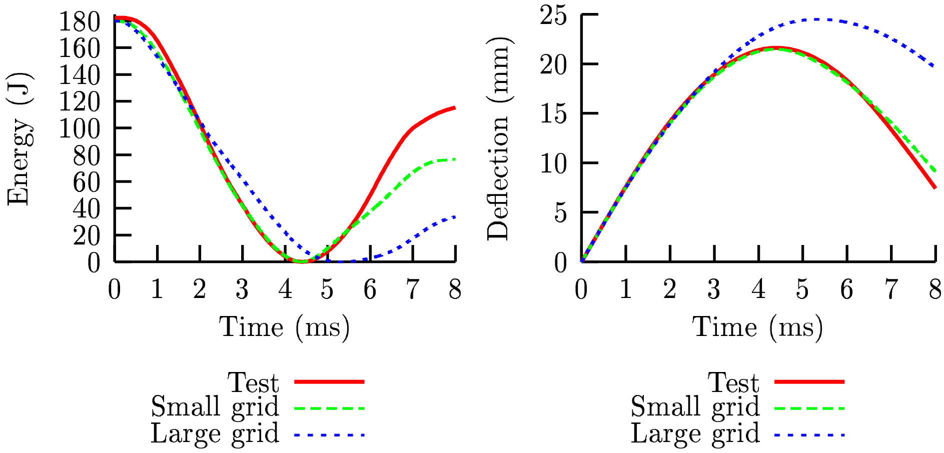

(a) Kinematic energy traces.

(b) Deflection traces.

Figure 7.8: Kinematic energies and deflections from simulations conducted on a small grid with few elements and a large grid with many elements.

varying behaviour. The large model becomes softer, allowing larger deflection and thus a longer lasting impact. This behaviour was not expected, and complicates the modelling of our sandwich plates significantly. To check whether the grid in Fig. 7.7 is too small and therefore too stiff, the two grids are simulated again, but without any failure models in the facings. The results are plotted in Fig. 7.9 and as seen the changes are very small. This means that the difference in our small and large grid simulations is not due to the meshes used.

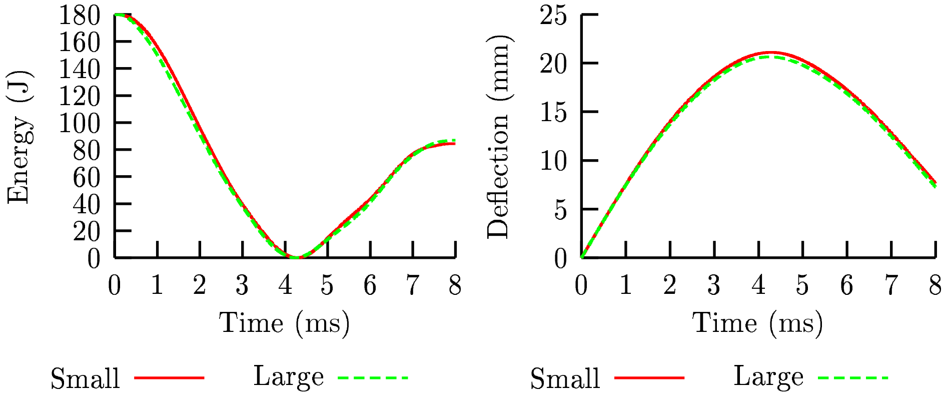

(a) Kinematic energy traces.

(b) Deflection traces.

Figure 7.9: Kinematic energies and deflections from simulations with few and many elements when the failure model is not used in the facings.

The softening in the large simulation must therefore be connected with our failure model in the facings. Fig. 7.10 show the failure in the facings for the small and large element model. When more elements are used more local failure around the projectile takes place. The internal energy in failed elements are lost and not returned to the projectile when the impact is over. Since the local stiffness of the faces under the projectile is reduced due to the failed elements, local indentation of the core also becomes larger.

Fig. 7.10 also show the plastic behaviour in the core. Large parts of the core near the impacted area suffers plastic deformation during the impact. Fig. 7.11 show traces of the internal energies in the facings and the core and for the hole sandwich for both the small and large grid simulation. From about 4.5 ms the internal energy in the small grid simulation is reduced, while less internal energy in the large grid simulation is returned because more is used when failure takes place during the impact. However, the large grid simulation is still in good agreement with our test results despite the fact that the small grid simulation are closer. More elements gives generally more accurate results, and Fig. 7.10(b) show the most realistic failure plot. The visual delamination pattern from the test shown in Fig. 5.23 is very local as in Fig. 7.10(b).

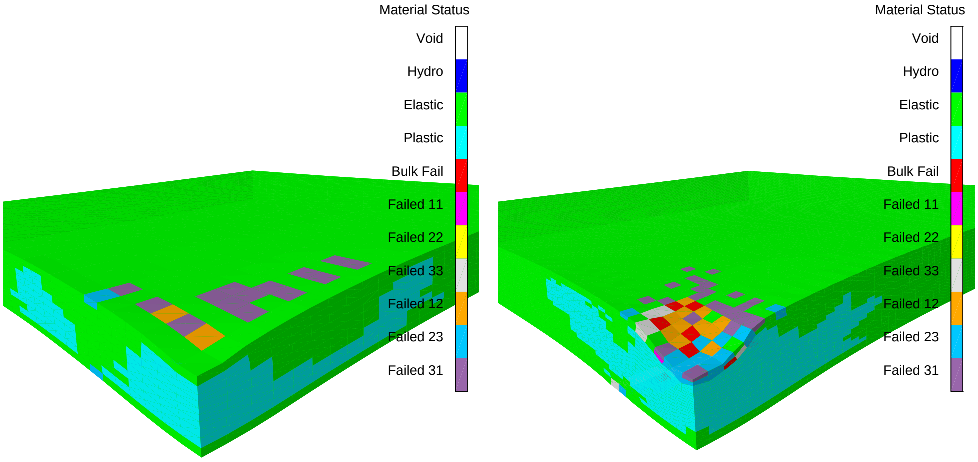

(a) Failure plot, 10 elements in the height and 31 in the width of the plate.

(b) Failure plot, 20 elements in the height and 62 in the width of the plate.

Figure 7.10: Failure plots two simulation with small and large elements at 3.75 ms. The 1, 2 and 3 axes are according to the right hand rule with the 3-direction pointing upwards.

The simulation data are compared with the test data by numerically integrating the acceleration from the projectile. Due to the problems described in Section 5.4.4 the acceleration data is taken from the second impact onto the plate. This might give a somewhat too fast impact, since the work with crushing the face and core are mostly done in the first impact. As the projectile hits the plate the second time most of the internal work is done and the impact becomes more elastic.

Due to these observations the large grid is used further in the next Section.

7.3.6 Strain gauge results

Our impacted sandwich plates were equipped with strain gauges on the top and bottom faces. These gauges measure the strain in the facings during the impact.

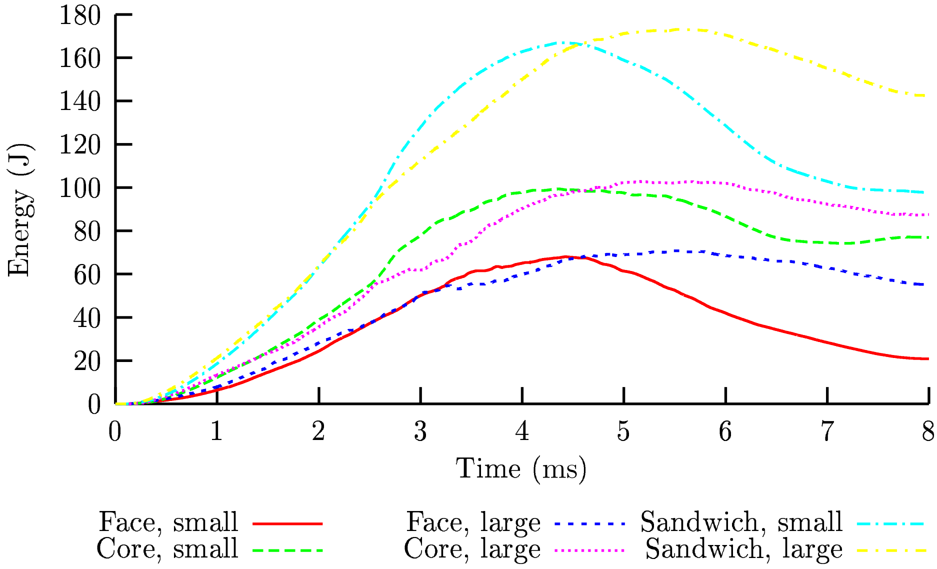

Figure 7.11: Internal energies in the facings, the core and for the hole sandwich compared for simulations with a small and a large grid.

Plate 2, which was impacted from 3.5 m has strain gauges placed as shown in Fig. 5.18. In AUTODYN, it is possible to declare elements as target elements. These target elements logs various parameters during the simulation. Unfortunately, strains are not logged in these elements, but the stress traces can be retrieved. The large mesh described in the previous section was used to model the sandwich, and target points according to the strain gauges in the impact test were defined. Stresses from these target points were found and strains calculated from Hook‘s law in three dimensions defined as

$$\epsilon_x = \frac{\sigma_x}{E} - \frac{\nu}{E}(\sigma_y + \sigma_z).$$

The stresses in the z-direction are small and neglectable compared to σ_x and σ_y. The strain in the x-direction is therefore calculated as

$$\epsilon_x = \frac{\sigma_x}{E} - \nu\frac{\sigma_y}{E},$$

where $E = E_x = E_y = 31500$ MPa and $\nu = 0.2$. Two strain gauges from the top facing, situated at 45 mm and 75 mm from the centre of the plate in the 0-direction are compared with the simulated strains. Fig. 7.12 shows the traces from the test and the simulation. As seen the simulated strains are much to low. At about 1.5 ms reaches the element taken as strain gauge 1 the failure mode limit, and the stress are set to zero. Strain gauge 2 situated further away from the load area show very little strain.

Strain gauge 5 and 6 from the bottom plate are also compared with the simulation and the traces are plotted in Fig. 7.13. According to the figure both test and simulated strain start at about 0.8 ms. Up to about 3 ms are the strains in good agreement with each others, but from there gauge 6 increases too much.

Strains are generally hard to simulate. In our tests, strains in the 0- and 90-direction varies a lot due to the stacking of the facings, and this behaviour is not

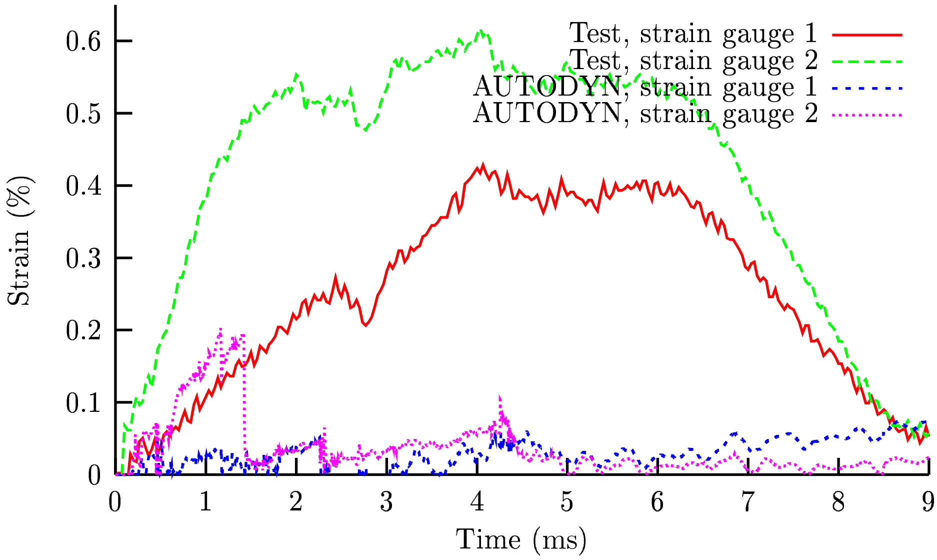

Figure 7.12: Strain plots from test and simulation of two gauges on the top facing. The strain gauges are situated in the 0-direction, at 75 and 45 mm from the centre of the plate, respectively.

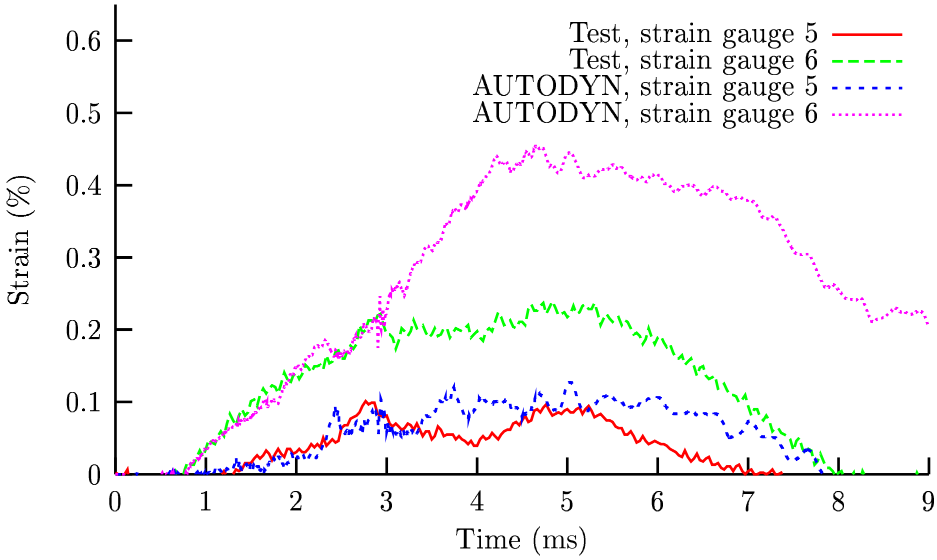

Figure 7.13: Strain plots from test and simulation of two gauges on the bottom facing. The strain gauges are situated in the 0-direction, at 75 and 45 mm from the centre of the plate respectively.

reflected in our simulations. No further attempts are therefore conducted in simulating strains in the facings using AUTODYN.

Chapter 8

Comparing Static and Dynamic tests and simulations

8.1 Introduction

Dynamic impact simulations are generally much more expensive and complicated than static simulations. Finding out whether static simulations can be used to model dynamic tests is therefore of great interest.

In the previous chapters sandwich plates have been tested and simulated for static and dynamic loads. In this chapter some comparisons between the static and dynamic tests and simulations are carried out.

8.2 Force vs. Deflection

The force from a dynamic impact test is found by multiplying the acceleration trace by the weight of the projectile according to Newtons 2nd law, $F = ma$. Numerical integration is performed twice on the acceleration data to retrieve the deflection.

Four force-deflection traces are plotted in Fig. 8.1. The dynamic test data are taken from the impact onto plate 1 described in Section 5.4.6 and the static test data are from the test described in Section 5.5. The AUTODYN impact trace is obtained using the mesh in Fig. 7.3 and the ANSYS static trace is from the simulation conduction in Section 6.3.2 with load area Width/80. Also, the deflection from the analytical solution with orthotropic facings described in Section 4.4 is calculated.

It can be seen that the traces from the static and dynamic tests are in very good agreement with each other. However, the maximum forces calculated in the static and dynamic simulations are slightly too high. The maximum force in the dynamic impact test is approximately 18000 N. This force is applied in the analytical solution with orthotropic facings resulting in a deflection of 14.7 mm. This is a bit less than in the tests and simulations, and is probably due to the lack of nonlinear material properties. These force-deflection curves can be used to measure the plate stiffness K from $F = Kx$, where F is the load applied and x the resulting deflection.

If the frequency of excitation applied to a structure is less than roughly one third of the structure‘s lowest natural frequency, then the effects of inertia can be neglected and the problem is quasi-static [19]. To find out whether the impacts conducted in

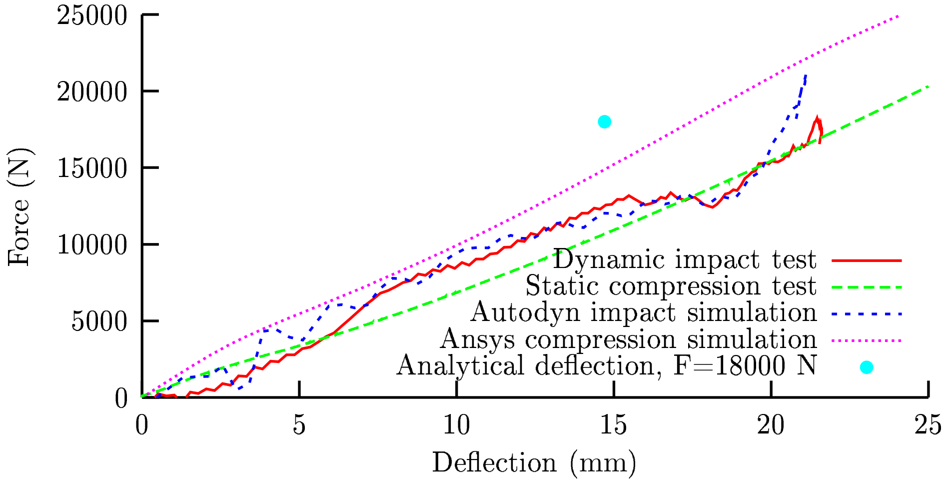

Figure 8.1: Force plotted against deflection.

this thesis behave quasi-static, the natural frequency of the sandwich plates must be found along with the frequency of excitation. However, very little information on how to obtain the natural frequency of sandwich plates is available, but an analytical expression for free vibration in a simply supported sandwich plate with isotropic facings is derived in [24] and is given as

$$w_{mn} = \left[\left(\frac{m\pi}{a}\right)^2 + n^2\right] \sqrt{\frac{\frac{D}{\rho^* b^4 (1-\nu^2)}}{1+\pi^2\theta\left[\left(\frac{m\pi}{a}\right)^2+n^2\right]}}, \text{ with } \theta = \frac{D}{S(1-\nu^2)b^2}.$$

Here, ρ^* is the density of the sandwich plate. This expression is implemented in MAPLE and the lowest natural frequency in the sandwich plates becomes

$$w_{11} = 1735\,\frac{1}{\mathrm{s}}.$$

From the impact tests, the contact between the projectile and the plate is found to last about $T_c = 8$ ms. Estimating the contact duration as half the period for free vibrations [1], the applied frequency becomes

$$w_a = \frac{\pi}{T_c} = \frac{\pi}{0.008\ \mathrm{s}} = 392\,\frac{1}{s}.$$

Therefore,

$$\frac{w_a}{w_{11}} = \frac{392}{1735} \approx \frac{1}{4} < \frac{1}{3},$$

and our impact tests are well within the regime of quasi-static impacts.

In Fig. 8.1, the force-deflection traces for the static and dynamic tests show the same behaviour. Therefore, applying the maximum force from the dynamic impact test in the static compression test gives the same deflection. Thus, the *dynamic increase factor DIF* defined as the ratio of the dynamic to static deflection [16] becomes approximately unity. Often, dynamic loads result in larger deflection than static [16].

The dynamic impact tests are now found to be quasi-static and the dynamic increase factor is found to be approximately unity. This means that the dynamic impact tests can be modelled with good accuracy using static models.

A comparison between the damage due to static loading and dynamic impact can not be performed, since the sandwich plate tested in static compression was loaded up to failure at about 30000 N.

Chapter 9

Summary and Conclusion

This thesis consists of two major parts; a testing part and a simulation part. All tests have been conducted at SINTEF Materials Technologies in cooperation with another student. In the following, the different tests and how they are simulated are presented.

9.1 Summary

Four point bending

Two sandwich beams were tested in four point bending according to the ASTM C393 standard in a Scheke Electro Hydraulic Strain Machine. Unfortunately both of the beams broke under the load bearings and not in the middle as predicted by theory.

An ANSYS simulation was conducted after the test, and the compression stresses in the core were predicted. The stresses in the core beneath the load bearings were higher than the compression yield stress limit provided by the manufacturer. Since the beams broke under the load bearings, ultimate failure stress in the facings and shear stress in the core could not be found. Young´s modulus for the facings and the shear modulus for the core were calculated, but the accuracy was poor.

Static deflection of a sandwich plate

One sandwich plate was tested in static deflection in the Scheke Electro Hydraulic Strain machine. The plate was situated on a quadratic steel frame and a projectile was pressed into the centre of the plate. A load-deflection curve and strain gauge traces were retrieved from the test results.

The plate deflection was simulated in ANSYS, and the deflection became very close to the test results. However, the initial slope of the simulated force-deflection curve became to stiff. This might be due to initially broken cells in the foam and poor contact between the facings and core. The strain gauge results were conciderably different in the 0- and 90-directions due to the layup of the facings. This behaviour was not implemented into our simulation models and the simulated strains were therefore not in very good agreement with the strains observed experimentally.

An analytical model was also developed for static deflection of sandwich plates. This model was implemented and solved using MAPLE. The deflection found was in very good agreement with the deflection from the ANSYS model using SHELL91 elements, which rely on the same assumptions as our analytical model.

Impact on sandwich plates

Three sandwich plates were tested in a drop weight rig. This test rig had been used earlier, but now the projectile was equipped with an accelerometer. In our first attempts, very large non physical oscillations and noise were observed. After a lot of testing, all noise sources were detected and removed, and the final drop tests could take place. Due to a wrong filter setting, the accelerometer data are taken from the second impact onto plate one and two, but the strain data was not inflicted by this problem. The accelerometer data was further processed and the kinematic energy and the deflection of the projectile were found. These data were compared with results from dynamic simulations conducted in AUTODYN. The simulated strains showed the same characteristic behaviour as the strains from the test.

Visual inspections of the sandwich plates after impact revealed that the sandwich plates suffered very little damage. Only a small area were the impact occurred had visual damage. No damage was observed on the bottom of the plates.

Our dynamic simulations were first implemented using only yield models in the core. The simulated kinematic energies and deflections were now in excellent agreement with the test results. When applying failure criteria in the facings, the model became a bit to soft. Also, the failure criteria in the facings were very sensitive to the mesh used. Large strain variations in the 0- and 90-directions were observed in the test data due to the layup ot the facings. This behaviour was not implemented in the simulation models, and comparisons became less accurate and therefore less interesting.

Comparing static and dynamic tests and simulations

Comparisons between the static and dynamic behaviour were conducted in Chapter 8. Force-deflection traces were compared, and it was found that the response of the plates to static and dynamic loads of the same magnitude were almost identical. It was also shown that the dynamic impacts performed in this thesis are within the quasi-static range.

9.2 Conclusion

The deflection of the indentator was measured in the static deflection test. This deflection is a combination of the global bending of the entire plate and the local indentation when pressing the face into the core. When calculating the deflection with the analytical model or using shell elements in a finite element simulation, the distance between the facings are assumed to be constant. Therefore, the deflection found in these models does not account for local indentation of the core. When performing static deflection tests of sandwich plates, both the deflection of the indentator and the deflection of the bottom face should therefore be measured. Then, the deflection from analytical and shell element models can be compared with the bottom face deflection. Also, more data on how the core and face performs together are retrieved. However, finite element solutions using many solid elements through the thickness of the plate model the deflection of the indentator with good agreement. The main drawback of this method is that it is much more time-consuming than simplified shell models.

An impact rig built at SINTEF was used in the dynamic impact tests of the sandwich plates. It consisted mainly of a tube holding the projectile and a steel frame supporting the sandwich. After some adjustments, this rig provided accurate and reprodusable results at a very low price compared to a new rig bought from a manufacturer. AUTODYN was used to model the dynamic impacts. From the dynamic tests, the kinematic energy and the deflection were retrieved and compared with the simulations. Very good agreement between tests and simulations were established with the AUTODYN software. The AUTODYN software can therefore be recommended when simulating impact dynamics on sandwich materials.

9.3 Further Work

During the work with this thesis, several new aspects arised and could make a basis for further studies of sandwich plates:

- Studying smaller sandwich plates which fit in the Rosand impact machine makes it easier to perform more impacts onto the sandwich plates with various impact weights and velocities. Simulate the impacts and study how the different impacts are modelled using the same parameters for each impact. In particular, study how the failure criteria in the facings inflict on the solution. Also, implement the facings so the various strains in the 0- and 90-directions are represented in the models.

- When sandwich plates are used in marine constructions, impacts on sandwiches submerged in water are of special interest. Therefore, full scale tests on sandwich plates submerged in water should be conducted. Study how the various processors in AUTODYN can model this problem using the coupling methodology described in Section 7.2.1.

- Perform impact tests on sandwiches with different core and face thicknesses and study how the results compare with each other. How does a simulation model perform when scaled up to model sandwiches with different geometry? Using this approach, more information on the reliability of the simulations can be retrieved.

References

[1] Serge Abrate. *Impact on Composite Structures.* Cambridge University Press, 1998. 75, 93

[2] H. G. Allen. *Analysis and Design of Structural Sandwich Panels.* Pergamon Press, Oxford, 1966. 3, 6

[3] Alfred Andersen. Gfrp testing. Technical report, SINTEF, 2003. 57

[4] ANSYS Inc., Canonsburg, USA. *ANSYS 6.1 User Manual*, 2002. 60

[5] PP Benhan, RJ Crawford, and CG Armstrong. *Mechanics of Engineering Materials.* Addison Wesley Longman Limited, second edition, 1996. 14

[6] Century Dynamics, Inc. *Autodyn Theory Manual*, 4.3 edition, 2003. 76

[7] Century Dynamics, Inc. *Autodyn User Manual*, 4.3 edition, 2003. 76

[8] Dytran Instruments Inc., www.dytran.com. *Accelerometer Mounting Considerations.* 39

[9] Jens Feuerlein. Numerical simulations of impact behaviour of aluminium and gfrp laminates compared with experiments. Master's thesis, Institute of Structure Technologies, ETH Zurich, 2002. 62, 63, 80

[10] The DIAB Group. Divinycell h-grade pvc foam material properties. www.diabgroup.com. 4, 53, 82

[11] N. J. Hoff. Bending and buckling of rectangular sandwich plates. Technical report, NACA TN 2225, 1950. 3

[12] Hottinger Baldwin Messtechnik GmbH. *Operating Manual. Measuring Amplifier system MGC/IGC.* 38

[13] Charles Libove and S. B. Batdorf. A general small-deflection theory for flat sandwich plates. Technical report, National Advisory Committee for Aeronautics (NACA) TN 1526, http://naca.larc.nasa.gov/, 1958. 3, 20

[14] R. D. Mindlin. The influence of rotary inertia and shear on flexural motions of isotropic elastic plates. *Journal of Applied Mechanics, Transaction of the ASME*, Vol. 18, 1951. 3

[15] National Instruments. *Measuring Strain with Strain Gauges*, April 2003. 29

[16] Per Kr. Larsen Pål G. Bergan and Egil Mollestad. *Svingninger av konstruksjoner.* Tapir Forlag, andre utgave, 1996. 93

[17] F. J. Plantema. *Sandwich Construction.* John Wiley & Sons, New York, 1966. 3, 6

[18] E. Reissner. the effect of transverse shear deformation on the bending of elastic plates. *Journal of Applied Mechanics*, Vol. 12, 1945. 3

[19] David S. Malkus Robert D. Cook and Michael E. Plesha. *Consepts and Applications of Finite Element Analysis.* John Wiley & Sons, third edition, 1989. 92

[20] Roberta A. Storer, editor. *Annual Book of ASTM Standards*, volume 15.03. American Society for Testing and Materials, 1997. 51

[21] Stephen P. Timoshenko and S. Woinowsky-Krieger. *Theory of Plates and Shells.* McGraw Hill College Div, 1959. 20

[22] Y. M. Xu and B. G. Miller. Instrumented impact testing of polymeric materials. Technical report, Materials Group, School of Engineering Sciences, University of Southhampton, 2001. 42

[23] Warren C Young. *Roark's formulas for stress and strain.* McGraw-Hill Book Company, 6th edition, 1989. 62

[24] Dan Zenkert. *An Introduction To Sandwich Construction.* Engineering Materials Advisory Services Ltd., 1995. 3, 6, 14, 26, 27, 93

Appendices

Appendix A

ANSYS input files

A.1 Linear solution using elements SOLID45, SOLID46, SHELL181 and SHELL91

```
/FILNAME,sandelementload
/OUTPUT,sandelementload,txt
/COM,------------RESULTAT COMPARISON-------------------------
/COM,
/COM SOLID45      SOLID46      SHELL181      SHELL91
/OUTPUT

!----- PARAMETERS -----
WIDTH=570/2
T_F=3
T_C=25
EX_FACE=26300
GXY_FACE=5000
PRXY_FACE=0.16
EX_CORE=80
PRXY_CORE=0.32

LOAD=10 ![N]

ELEMENT=20

!-----------------------------------
!-            SOLID45             -
!-----------------------------------

/PREP7
!----------GEOMETRY----------
/VIEW,1,0.7,-0.65,0.35
/ANGLE,1,-57
K,1
K,2,WIDTH
K,3,WIDTH,WIDTH
K,4,,WIDTH
KGEN,2,1,4,1,,,T_F
KGEN,2,1,4,1,,,T_C+T_F
KGEN,2,1,4,1,,,T_C+2*T_F
L,2,1
```

```
L,6,2
L,10,6
L,14,10
L,4,3
L,8,7
L,12,11
L,16,15
V,1,2,3,4,5,6,7,8
V,5,6,7,8,9,10,11,12
V,9,10,11,12,13,14,15,16
VGLUE,1,2,3


!----------MATERIAL PROPERTIES----------
!SOLID ELEMENT
ET,1,SOLID45

!FACE
MP,EX,1,EX_FACE  ![N/mm^2]
MP,EY,1,EX_FACE
MP,EZ,1,EX_FACE
MP,GXY,1,GXY_FACE
MP,GYZ,1,GXY_FACE
MP,GXZ,1,GXY_FACE
MP,PRXY,1,PRXY_FACE
MP,PRYZ,1,PRXY_FACE
MP,PRXZ,1,PRXY_FACE

!CORE
MP,EX,2,EX_CORE
MP,PRXY,2,PRXY_CORE

!----------MESHING----------
LSEL,S,LENGTH,,T_F
LESIZE,ALL,,,2
LSEL,S,LENGTH,,T_C
LESIZE,ALL,,,6
LSEL,S,LENGTH,,WIDTH
LESIZE,ALL,,,ELEMENT

MAT,1
VMESH,1
MAT,2
VMESH,2
MAT,1
VMESH,3

!----------BOUNDARY CONDITIONS----------
NSEL,S,LOC,X,0
DSYM,SYMM,X
NSEL,S,LOC,Y,0
DSYM,SYMM,Y

NSEL,S,LOC,X,WIDTH
NSEL,A,LOC,Y,WIDTH
NSEL,R,LOC,Z,0
D,ALL,UZ,0
```

```
!----------LOAD----------
NSEL,S,LOC,X,0,WIDTH/12
NSEL,R,LOC,Y,0,WIDTH/12
NSEL,R,LOC,Z,T_C+2*T_F
ESLN
SFE,ALL,6,PRES,,-LOAD

!----------SOLUTION----------
ALLSEL
/SOLU
ANTYPE,STATIC
SOLVE
FINISH

!----------ANALYSING RESULTS----------
/POST1
NSORT,U,Z,,1
*GET,DEF45MAX,SORT,,MAX
FSUM,0,ALL
*GET,TOTLOAD45,FSUM,FZ !LOAD
FINISH

PARSAV
/CLEAR, NOSTART
/FILNAME,sandelementload
PARRES


!-----------------------------------
!-            SOLID46            -
!-----------------------------------

/PREP7
!----------GEOMETRY----------
/VIEW,1,0.7,-0.65,0.35
/ANGLE,1,-57
K,1
K,2,WIDTH
K,3,WIDTH,WIDTH
K,4,,WIDTH
KGEN,2,1,4,1,,,2*T_F+T_C
L,2,1
L,6,2
L,4,3
L,8,7
V,1,2,3,4,5,6,7,8

!----------MATERIAL PROPERTIES----------
!SOLID ELEMENT
ET,1,SOLID46
R,1,3,1     !SYMMETRIC STACKING
RMORE
RMORE,1,,T_F,2,,T_C

!FACE
MP,EX,1,EX_FACE  ![N/mm^2]
MP,EY,1,EX_FACE
MP,EZ,1,EX_FACE
```

```
MP,GXY,1,GXY_FACE
MP,GYZ,1,GXY_FACE
MP,GXZ,1,GXY_FACE
MP,PRXY,1,PRXY_FACE
MP,PRYZ,1,PRXY_FACE
MP,PRXZ,1,PRXY_FACE

!CORE
MP,EX,2,EX_CORE
MP,PRXY,2,PRXY_CORE

!----------MESHING----------
LSEL,S,LENGTH,,2*T_F+T_C
LESIZE,ALL,,,1
LSEL,S,LENGTH,,WIDTH
LESIZE,ALL,,,ELEMENT
VMESH,ALL

!----------BOUNDARY CONDITIONS----------
NSEL,S,LOC,X,0
DSYM,SYMM,X
NSEL,S,LOC,Y,0
DSYM,SYMM,Y
NSEL,S,LOC,X,WIDTH
NSEL,A,LOC,Y,WIDTH
NSEL,R,LOC,Z,0
D,ALL,UZ,0

!----------LOAD----------
NSEL,S,LOC,X,0,WIDTH/12
NSEL,R,LOC,Y,0,WIDTH/12
NSEL,R,LOC,Z,T_C+2*T_F
ESLN
SFE,ALL,6,PRES,,-LOAD

!----------SOLUTION----------
ALLSEL
/SOLU
ANTYPE,STATIC
SOLVE
FINISH

!----------ANALYSING RESULTS----------
/POST1
NSORT,U,Z,,1
*GET,DEF46MAX,SORT,,MAX
FSUM,0,ALL
*GET,TOTLOAD46,FSUM,FZ !LOAD
!/ESHAPE,1
!PLDISP
FINISH

PARSAV
/CLEAR, NOSTART
/FILNAME,sandelementload
PARRES
```

```
!-----------------------------------
!-            SHELL181            -
!-----------------------------------

/PREP7
K,1
K,2,WIDTH
K,3,WIDTH,WIDTH
K,4,,WIDTH
L,2,1
L,4,3
A,1,2,3,4

ET,1,SHELL181
!R,1,2*T_F+T_C   !THICKNESS SHELL
sectype,1,shell,,
secdata,T_F,1,,3
secdata,T_C,2,,3
secdata,T_F,1,,3

!FACE
MP,EX,1,EX_FACE  ![N/mm^2]
MP,EY,1,EX_FACE
MP,EZ,1,EX_FACE
MP,GXY,1,GXY_FACE
MP,GYZ,1,GXY_FACE
MP,GXZ,1,GXY_FACE
MP,PRXY,1,PRXY_FACE
MP,PRYZ,1,PRXY_FACE
MP,PRXZ,1,PRXY_FACE

!CORE
MP,EX,2,EX_CORE
MP,PRXY,2,PRXY_CORE

!----------MESHING----------
LSEL,S,LENGTH,,WIDTH
LESIZE,ALL,,,ELEMENT
AMESH,1

!----------BOUNDARY CONDITIONS----------
NSEL,S,LOC,X,0
DSYM,SYMM,X
NSEL,S,LOC,Y,0
DSYM,SYMM,Y

NSEL,S,LOC,X,WIDTH
NSEL,A,LOC,Y,WIDTH
D,ALL,UZ,0

!----------LOAD----------
NSEL,S,LOC,X,0,WIDTH/12
NSEL,R,LOC,Y,0,WIDTH/12
ESLN
SFE,ALL,2,PRES,,-LOAD

!----------SOLUTION----------
ALLSEL
```

```
/SOLU
ANTYPE,STATIC
SOLVE
FINISH

!----------ANALYSING RESULTS----------
/POST1
NSORT,U,Z,,1
*GET,DEF181MAX,SORT,,MAX
FSUM,0,ALL
*GET,TOTLOAD181,FSUM,FZ !LOAD
FINISH

PARSAV
/CLEAR, NOSTART
/FILNAME,sandelementload
PARRES


!-----------------------------------
!-            SHELL91             -
!-----------------------------------

/PREP7
!----------GEOMETRY----------
/VIEW,1,0.7,-0.65,0.35
/ANGLE,1,-57
K,1
K,2,WIDTH
K,3,WIDTH,WIDTH
K,4,,WIDTH
L,2,1
L,4,3
A,1,2,3,4

!----------MATERIAL PROPERTIES----------
ET,1,SHELL91,3,1
KEYOPT,1,8,1   !ALL LAYERS
KEYOPT,1,9,1   !SANDWICH OPTION
R,1,3,1        !SYMMETRIC STACKING
RMORE
RMORE,1,,T_F
RMORE,2,,T_C

!FACE
MP,EX,1,EX_FACE  ![N/mm^2]
MP,EY,1,EX_FACE
MP,EZ,1,EX_FACE
MP,GXY,1,GXY_FACE
MP,GYZ,1,GXY_FACE
MP,GXZ,1,GXY_FACE
MP,PRXY,1,PRXY_FACE
MP,PRYZ,1,PRXY_FACE
MP,PRXZ,1,PRXY_FACE

!CORE
MP,EX,2,EX_CORE
MP,PRXY,2,PRXY_CORE
```

```
!----------MESHING----------
LSEL,S,LENGTH,,WIDTH
LESIZE,ALL,,,ELEMENT
AMESH,1

!----------BOUNDARY CONDITIONS----------
NSEL,S,LOC,X,0
DSYM,SYMM,X
NSEL,S,LOC,Y,0
DSYM,SYMM,Y

NSEL,S,LOC,X,WIDTH
NSEL,A,LOC,Y,WIDTH
D,ALL,UZ,0

!----------LOAD----------
NSEL,S,LOC,X,0,WIDTH/12
NSEL,R,LOC,Y,0,WIDTH/12
ESLN
SFE,ALL,2,PRES,,-LOAD

!----------SOLUTION----------
ALLSEL
/SOLU
ANTYPE,STATIC
SOLVE
FINISH

!----------ANALYSING RESULTS----------
/POST1
NSORT,U,Z,,1
*GET,DEF91MAX,SORT,,MAX
FSUM,0,ALL
*GET,TOTLOAD91,FSUM,FZ !LOAD
FINISH

PARSAV
/CLEAR, NOSTART
/FILNAME,sandelementload
PARRES



!---------------------------------------------------
/OUTPUT,sandelementload,txt,,APPEND
*VWRITE,DEF45MAX,DEF46MAX,DEF181MAX,DEF91MAX,TOTLOAD45,TOTLOAD46,TOTLOAD181,TOTLOAD91
%G  %G  %G  %G   %G   %G   %G   %G
/OUTPUT

*LIST,RESULTAT,TXT

!MAKE TEX-TABLE
/OUTPUT,sandelementload,tex
/COM,\begin{table}\centering
/COM,\begin{tabular}{c|c|c|c}
/COM, SOLID45 & SOLID46 & SHELL99 & SHELL91 \\
/COM,\hline
```

```
*VWRITE,DEF45MAX,DEF46MAX,DEF181MAX,DEF91MAX
%G & %G & %G & %G
/COM,\end{tabular}
/COM,\end{table}
/OUTPUT
```

A.2 Large mesh, SOLID45 element

```
/FILNAME,s45g
/NOPR  !Supress output

!----- PARAMETERS -----
WIDTH=570/2
T_F=3
T_C=25

LOAD=590.95 ! [N/mm^2]

ELEMENT=40

EL=WIDTH/ELEMENT

!-----------------------------------
!-             SOLID45            -
!-----------------------------------

/PREP7
!----------GEOMETRY----------
/VIEW,1,0.7,-0.65,0.35
/ANGLE,1,-57
K,1
K,2,WIDTH
K,3,WIDTH,WIDTH
K,4,,WIDTH
KGEN,2,1,4,1,,,T_F
KGEN,2,1,4,1,,,T_C+T_F
KGEN,2,1,4,1,,,T_C+2*T_F
L,2,1
L,6,2
L,10,6
L,14,10
L,4,3
L,8,7
L,12,11
L,16,15
V,1,2,3,4,5,6,7,8
V,5,6,7,8,9,10,11,12
V,9,10,11,12,13,14,15,16
VGLUE,1,2,3

!----------MATERIAL PROPERTIES----------
!SOLID ELEMENT
ET,1,SOLID45

!FACE
```

```
MP,EX,1,31500  ![N/mm^2]
MP,EY,1,31500
MP,EZ,1,8230
MP,GXY,1,6000
MP,GYZ,1,5140
MP,GXZ,1,5140
MP,PRXY,1,0.2
MP,PRYZ,1,0.2
MP,PRXZ,1,0.2

!CORE
MP,EX,2,80
MP,PRXY,2,0.32

TB,BISO,2
TBDATA,1,1.0   ! Yield stress
TBDATA,2,0.0268   ! Tangent modulus


!----------MESHING----------
LSEL,S,LENGTH,,T_F
LESIZE,ALL,,,2
LSEL,S,LENGTH,,T_C
LESIZE,ALL,,,6
LSEL,S,LOC,X
LSEL,A,LOC,Y
LSEL,R,LENGTH,,WIDTH
LESIZE,ALL,,,80
LSEL,S,LOC,X,WIDTH
LSEL,A,LOC,Y,WIDTH
LSEL,R,LENGTH,,WIDTH
LESIZE,ALL,,,20,4.5

MAT,1
VMESH,1
MAT,2
VMESH,2
MAT,1
VMESH,3

!----------BOUNDARY CONDITIONS----------
NSEL,S,LOC,X,0
DSYM,SYMM,X
NSEL,S,LOC,Y,0
DSYM,SYMM,Y

NSEL,S,LOC,X,WIDTH
NSEL,A,LOC,Y,WIDTH
NSEL,R,LOC,Z,0
D,ALL,UZ,0

!----------LOAD----------
NSEL,S,LOC,X,0
NSEL,R,LOC,Y,0
NSEL,R,LOC,Z,T_C+2*T_F
ESLN
SFE,ALL,6,PRES,,LOAD
```

```
!----------SOLUTION----------
ALLSEL
/SOLU
ANTYPE,STATIC
NLGEOM,ON
SOLCONTROL,ON
NSUBST,NSBSTP,NSBMX,NSBMN
KBC,0
AUTOTS,ON
NEQIT,100
PRED,ON
LNSRCH,ON
NCNV,2

!OUTPR,ALL,ALL
OUTRES,ALL,ALL

SOLVE
FINISH

!----------ANALYSING RESULTS----------
/POST1
/OUTPUT,s45g,txt
/COM,i  Load  DEF45MAX DEF45T DEF45B STR45T STR45B S45T S45B
/OUTPUT
/OUTPUT,s45g_strain,txt
/COM,i  Load  S1  S2  S3  S6  S5
/OUTPUT

*GET,SOLU_STEP,ACTIVE,0,SOLU,NCMSS
*DO,i,1,SOLU_STEP
SET,,,,,,,i
FSUM,0,ALL
*GET,TOTLOAD,FSUM,FZ !LOAD
!Max deformation
NSORT,U,Z,,1
*GET,DEF45MAX,SORT,,MAX
NSEL,ALL
*GET,DEF45T,NODE,NODE(0,0,31),U,Z
*GET,STR45T,NODE,NODE(0,0,31),EPTO,X
*GET,S45T,NODE,NODE(0,0,31),S,X
NSEL,ALL
*GET,DEF45B,NODE,NODE(0,0,0),U,Z
*GET,STR45B,NODE,NODE(0,0,0),EPTO,X
*GET,S45B,NODE,NODE(0,0,0),S,X

NSEL,ALL
*GET,S1,NODE,26169,EPTO,X
*GET,S2,NODE,26158,EPTO,X
*GET,S3,NODE,26137,EPTO,X
*GET,S6,NODE,48,EPTO,X
*GET,S5,NODE,27,EPTO,X

!-----

/OUTPUT,s45g,txt,,APPEND
*VWRITE,i,-4*TOTLOAD,-DEF45MAX,-DEF45T,-DEF45B,STR45T,STR45B,S45T,S45B
%I   %I   %G   %G   %G   %G   %G   %G   %G
```

```
/OUTPUT
/OUTPUT,s45g_strain,txt,,APPEND
*VWRITE,i,-4*TOTLOAD,S1,S2,S3,S6,S5
%I   %I   %G   %G   %G   %G   %G
/OUTPUT
/OUTPUT
*ENDDO
FINISH
```

Appendix B

MAPLE files

B.1 Sandwich beam

```
> restart:
```

Solving the beam equation for bending deflections for the intervals [0,(L2-L1)/2], [(L2-L1)/2,(L2+L1)/2] and [(L2+L1)/2,L2]:

```
> w_b1:=unapply(rhs(subs(_C1=C1,dsolve(
  {diff(w(x),x$2)=-P/2*x/D_,w(0)=0},w(x)))),x);
  w_b2:=unapply(rhs(subs(_C2=D2,dsolve(
  {diff(w(x),x$2)=-P/2*(L2-L1)/(2*D_),D(w)(L2/2)=0},w(x)))),x);
  w_b3:=unapply(rhs(subs(_C2=E2,dsolve(
  {diff(w(x),x$2)=-P/2*(L2-x)/D_,w(L2)=0},w(x)))),x);
```

$$w\_b1 := x \rightarrow -\frac{1}{12}\,\frac{P\,x^3}{D\_} + C1\,x$$

$$w\_b2 := x \rightarrow -\frac{1}{8}\,\frac{P\,(L2 - L1)\,x^2}{D\_} - \frac{1}{8}\,\frac{P\,(-L2 + L1)\,L2\,x}{D\_} + \mathrm{D2}$$

$$w\_b3 := x \rightarrow -\frac{1}{4}\,\frac{P\,x^2\,L2}{D\_} + \frac{\frac{1}{12}\,P\,x^3}{D\_} - \frac{1}{6}\,\frac{(-P\,L2^3 + 6\,E2\,D\_)\,x}{L2\,D\_} + E2$$

Using boundary conditions to find the integration constants:

```
> C1:=solve(D(w_b1)((L2-L1)/2)=D(w_b2)((L2-L1)/2),C1);
  D2:=solve(w_b1((L2-L1)/2)=w_b2((L2-L1)/2),D2);
  E2:=solve(w_b3((L2+L1)/2)=w_b2((L2+L1)/2),E2);
```

$$C1 := -\frac{1}{16}\,\frac{P\,(-L2 + L1)\,(L2 + L1)}{D\_}$$

$$\mathrm{D2} := \frac{1}{96}\,\frac{P\,(-L2 + L1)^3}{D\_}$$

$$E2 := -\frac{1}{48}\,\frac{L2\,(3\,L1^2 + L2^2)\,P}{D\_}$$

Finding the shear deflection:

```
> w_s1:=P/2*x/S;
  w_s2:=P/2*(L2-L1)/(2*S);
  w_s3:=P/2*(L2-x)/S;
```

$$w\_s1 := \frac{1}{2}\,\frac{P\,x}{S}$$

$$w\_s2 := \frac{1}{4}\,\frac{P\,(L2-L1)}{S}$$

$$w\_s3 := \frac{1}{2}\,\frac{P\,(L2-x)}{S}$$

Superimposing the solutions, w=w_v+w_s:

```
> w1:=unapply((w_b1(x)+w_s1),x);
  w2:=unapply((w_b2(x)+w_s2),x);
  w3:=unapply((w_b3(x)+w_s3),x);
```

$$w1 := x \to -\frac{1}{12}\,\frac{P\,x^3}{D\_} - \frac{1}{16}\,\frac{P\,(-L2+L1)\,(L2+L1)\,x}{D\_} + \frac{\frac{1}{2}\,P\,x}{S}$$

$$w2 := x \to -\frac{1}{8}\,\frac{P\,(L2-L1)\,x^2}{D\_} - \frac{1}{8}\,\frac{P\,(-L2+L1)\,L2\,x}{D\_} + \frac{\frac{1}{96}\,P\,(-L2+L1)^3}{D\_} + \frac{\frac{1}{4}\,P\,(L2-L1)}{S}$$

$$w3 := x \to -\frac{1}{4}\,\frac{P\,x^2\,L2}{D\_} + \frac{\frac{1}{12}\,P\,x^3}{D\_} - \frac{1}{6}\,\frac{(-P\,L2^3 - \frac{1}{8}\,L2\,(3\,L1^2 + L2^2)\,P)\,x}{L2\,D\_}$$
$$- \frac{1}{48}\,\frac{L2\,(3\,L1^2+L2^2)\,P}{D\_} + \frac{\frac{1}{2}\,P\,(L2-x)}{S}$$

Solving two equations to find the flexural rigidity D and shear stiffness S, lign1: Quarter point loading, L1=1/2L2 lign2: Third part loading, L1=1/3L2

First, the equations for the deflection at center of the beam is found:

```
> lign1:=delta[1]=subs({P=P[1],L2=L,L1=1/2*L},w2(L2/2));
  lign2:=delta[2]=subs({P=P[2],L2=L,L1=1/3*L},w2(L2/2));
  sols:=(solve({lign1,lign2},{D_,S}));
```

$$lign1 := \delta_1 = \frac{11}{768}\,\frac{P_1\,L^3}{D\_} + \frac{\frac{1}{8}\,P_1\,L}{S}$$

$$lign2 := \delta_2 = \frac{23}{1296}\,\frac{P_2\,L^3}{D\_} + \frac{\frac{1}{6}\,P_2\,L}{S}$$

$$sols := \{S = -\frac{7}{2}\,\frac{P_2\,L\,P_1}{-297\,\delta_2\,P_1 + 368\,P_2\,\delta_1},\ D\_ = \frac{7}{1728}\,\frac{P_2\,L^3\,P_1}{4\,P_2\,\delta_1 - 3\,\delta_2\,P_1}\}$$

The deflection under the load bearings:

```
> lign1:=d[1]=subs({P=P[1],L2=L,L1=1/2*L},w2((L2-L1)/2));
  lign2:=d[2]=subs({P=P[2],L2=L,L1=1/3*L},w2((L2-L1)/2));
  sols:=(solve({lign1,lign2},{D_,S}));
```

$$lign1 := d_1 = \frac{1}{96}\,\frac{P_1\,L^3}{D\_} + \frac{\frac{1}{8}\,P_1\,L}{S}$$

$$lign2 := d_2 = \frac{5}{324}\,\frac{P_2\,L^3}{D\_} + \frac{\frac{1}{6}\,P_2\,L}{S}$$

$$sols := \{S = \frac{1}{2}\,\frac{P_2\,L\,P_1}{-27\,d_2\,P_1 + 40\,P_2\,d_1},\ D\_ = -\frac{1}{216}\,\frac{P_2\,L^3\,P_1}{4\,P_2\,d_1 - 3\,d_2\,P_1}\}$$

B.2 Numerical Integration

```
> restart:with(plots):
```

```
Warning, the name changecoords has been redefined
```

Read acceleration data:

```
> a:=readdata("p:testing/Fallslag/Prover/ordna/gnuplot/p1_300_3_acc.txt
  ",2): # [g]
> n:=nops(a);h:=1/30000:
```

$$n := 241$$

Numerical integration:

```
> v:=array(1..n):
  v[1]:=7.67: # [m/s]
  d:=array(1..n):
  d[1]:=0: # [mm]
  for i from 2 to n do
  v[i]:=v[i-1]-h*9.81*(a[i-1,2]+a[i,2])/2:
  d[i]:=d[i-1]-h*1000*(v[i-1]+v[i])/2:
  end do:
```

Create plottable lists:

```
> v:=[seq([a[i,1],v[i]],i=1..n)]:
  e:=[seq([v[i,1],1/2*6.2*v[i,2]^2],i=1..n)]:
  d:=[seq([v[i,1],d[i]],i=1..n)]:
```

Plots of the solutions:

```
> origdev:=interface(plotdevice):
  plotsetup(
  ‘ps‘,plotoutput=‘numint_ny01.ps‘,plotoptions=‘color,noborder‘);
  listplot(v,legend="Velosity (m/s)",color=green);
  plotsetup(
  ‘ps‘,plotoutput=‘numint_ny02.ps‘,plotoptions=‘color,noborder‘);
  listplot(e,legend="Energy (J)",color=red);
  plotsetup(
  ‘ps‘,plotoutput=‘numint_ny03.ps‘,plotoptions=‘color,noborder‘);
  listplot(d,legend="Deflection (mm)",color=blue);
  plotsetup(origdev);
  listplot(v,legend="Velosity (m/s)",color=green);
  listplot(e,legend="Energy (J)",color=red);
  listplot(d,legend="Deflection (mm)",color=blue);
```

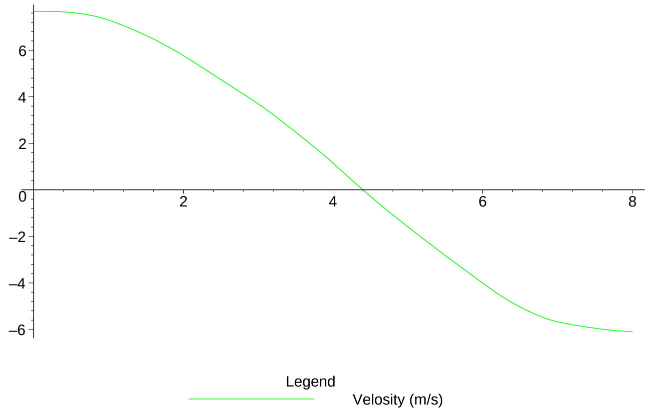
6
4
2
0
–2
–4
–6
2
4
6
8
Legend
Velosity (m/s)

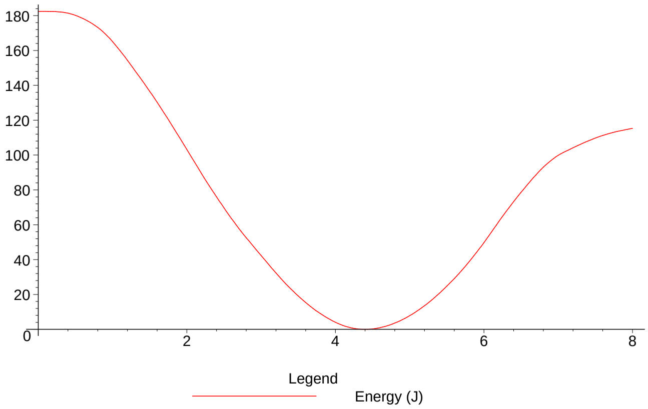
180
160
140
120
100
80
60
40
20
0
2
4
6
8
Legend
Energy (J)

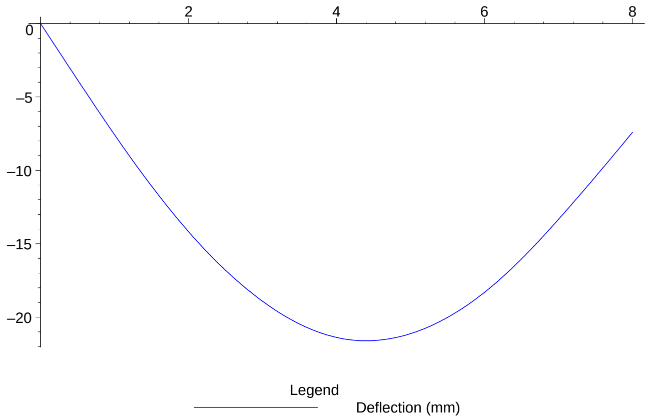
2
4
6
8
0
–5
–10
–15
–20
Legend
Deflection (mm)

B.3 Analytical solution to sandwich plate with orthotropic facing

```
> restart:
```

Assumptions:

- t_f<<t_c, thin faces
- E_c<<E_f, weak core

Plate dimensions :

```
> t_f:=3:
  t_c:=25:
  d:=t_f+t_c:
  a:=570:
  b:=a:
```

Material properties:

```
> E_fx:=31500:
  nu_fxy:=0.2:
  E_fy:=31500:
  nu_fyx:=0.2:
  G_fxy:=6000:
  E_c:=80:
  G_c:=31;
  S_x:=(G_c*d^2)/t_c;
  S_y:=S_x;
```

$$G\_c := 31$$

$$S\_x := \frac{24304}{25}$$

$$S\_y := \frac{24304}{25}$$

Flexural rigidities:

```
> D_x:=(E_fx*t_f*d^2)/2;
  D_y:=(E_fy*t_f*d^2)/2;
  D_xy:=2*(G_fxy*t_f*d^2)/2;
```

$$D\_x := 37044000$$

$$D\_y := 37044000$$

$$D\_xy := 14112000$$

Load:

```
> c:=a/20:
  Q:=30000;
  q_mn:=evalf(4/(a*b)*int(int(Q/(c^2)*sin(m*Pi*x/a)*sin(n*Pi*y/b),y=(b-c
  )/2..(b+c)/2),x=(a-c)/2..(a+c)/2));
```

$$Q := 30000$$

$$q\_mn := 14.96896526(\cos(1.649336143\,n) - 1.\cos(1.492256511\,n))\\ (\cos(1.649336143\,m) - 1.\cos(1.492256511\,m))/(n\,m)$$

Fourier Coefficients:

```
> W_mn:=-1/(S_x*S_y)*(1/2*D_xy*((m*Pi/a)^4*D_x/(1-nu_fxy*nu_fyx)-
  (m*Pi/a)^2*(n*Pi/b)^2*(nu_fxy*D_x+nu_fyx*D_y)/(1-nu_fxy*nu_fyx)+
  (n*Pi/b)^4*D_y/(1-nu_fxy*nu_fyx))+(m*Pi/a)^2*(n*Pi/b)^2*
  (D_x*D_y)/(1-nu_fxy*nu_fyx))-((m*Pi/a)^2*
  D_x/(S_x*(1-nu_fxy*nu_fyx))+(n*Pi/b)^2*D_y/(S_y*(1-nu_fxy*nu_fyx))
  -1/2*D_xy*(1/S_x*(m*Pi/a)^2+1/S_y*(n*Pi/b)^2)-1;
> X_mnS_y:=1/2*(m*Pi/a)^5*D_x*D_xy/(1-nu_fxy*nu_fyx)+(m*Pi/a)^3*
  (n*Pi/b)^2*(D_x*D_y/(1-nu_fxy*nu_fyx)-D_xy*(nu_fxy*D_x+nu_fyx*D_y)/
  (2*(1-nu_fxy*nu_fyx)))-1/2*(m*Pi/a)*(n*Pi/b)^4*D_y*D_xy/
  (1-nu_fxy*nu_fyx)+S_y*(m*Pi/a)*((m*Pi/a)^2*D_x/(1-nu_fxy*nu_fyx)+
  (n*Pi/b)^2*(D_xy+nu_fyx*D_x/(1-nu_fxy*nu_fyx)));
> Y_mnS_x:=-1/2*(n*Pi/b)^5*D_y*D_xy/(1-nu_fxy*nu_fyx)-(m*Pi/a)^2*
  (n*Pi/b)^3*(D_x*D_y/(1-nu_fxy*nu_fyx)-D_xy*(nu_fxy*D_x+nu_fyx*D_y)/
  (2*(1-nu_fxy*nu_fyx)))+1/2*(m*Pi/a)^4*(n*Pi/b)*D_x*D_xy/
  (1-nu_fxy*nu_fyx)-S_x*(n*Pi/b)*((n*Pi/b)^2*D_y/(1-nu_fxy*nu_fyx)+
  (m*Pi/a)^2*(D_xy+nu_fxy*D_y/(1-nu_fxy*nu_fyx)));
> Z_mn:=((m*Pi/a)*X_mnS_y/S_y-(n*Pi/b)*Y_mnS_x/S_x);
```

$$W\_mn := -.002729168161\, m^4\, \pi^4 - .01323646560\, m^2\, \pi^4\, n^2 - .002729168161\, n^4\, \pi^4$$
$$- .1445078635\, m^2\, \pi^2 - .1445078635\, n^2\, \pi^2 - 1$$

$$X\_mnS\_y := 4.525128708\, m^5\, \pi^5 + 21.94687423\, m^3\, \pi^5\, n^2 - 4.525128708\, m\, \pi^5\, n^4$$
$$+ \frac{12152}{7125}\, m\, \pi\, (118.7673130\, m^2\, \pi^2 + 67.18836565\, n^2\, \pi^2)$$

$$Y\_mnS\_x := -4.525128708\, n^5\, \pi^5 - 21.94687423\, m^2\, \pi^5\, n^3 + 4.525128708\, m^4\, \pi^5\, n$$
$$- \frac{12152}{7125}\, n\, \pi\, (118.7673130\, n^2\, \pi^2 + 67.18836565\, m^2\, \pi^2)$$

$$Z\_mn := \frac{5}{2770656} m\, \pi (4.525128708\, m^5\, \pi^5 + 21.94687423\, m^3\, \pi^5\, n^2$$
$$- 4.525128708\, m\, \pi^5\, n^4 + \frac{12152}{7125}\, m\, \pi\, (118.7673130\, m^2\, \pi^2 + 67.18836565\, n^2\, \pi^2))$$
$$- \frac{5}{2770656} n\, \pi (-4.525128708\, n^5\, \pi^5 - 21.94687423\, m^2\, \pi^5\, n^3$$
$$+ 4.525128708\, m^4\, \pi^5\, n - \frac{12152}{7125}\, n\, \pi\, (118.7673130\, n^2\, \pi^2 + 67.18836565\, m^2\, \pi^2))$$

Deflection:

```
> w:=(x,y,k)->(add(add(evalf(-W_mn*q_mn/Z_mn*sin(m*Pi*x/a)*sin(n*Pi*y/a
  )),m=1..k),n=1..k));
  w(a/2,b/2,27);
```

$$w := (x,\, y,\, k) \to \mathrm{add}\left(\mathrm{add}\left(\mathrm{evalf}\left(-\frac{W\_mn\; q\_mn \sin(\frac{m\, \pi\, x}{a}) \sin(\frac{n\, \pi\, y}{a})}{Z\_mn}\right),\ m = 1..k\right),\ n = 1..k\right)$$

$$24.20504183$$

Test convergence:

```
> t:=time():
  wk:=w(a/2,b/2,1):
  kiter:=[[0,0,100],[1,wk,100]]:
  for i from 3 by 2 to 500 while abs(kiter[nops(kiter),3])>0.1 do
  wk_old:=copy(wk):
  wk:=w(a/2,b/2,i):
  kiter:=[op(kiter),[i,wk,(wk-wk_old)/wk*100]]:
  wk_old:=copy(wk):
  end do:
  time()-t;
  k_num:=kiter[nops(kiter),1];max_def:=kiter[nops(kiter),2];
```

$$15.062$$

$$k\_num := 37$$
$$max\_def := 24.49051030$$

Convergence plot:

```
> plots[listplot]([seq([kiter[i,1],kiter[i,2]],i=1..nops(kiter))]);
```

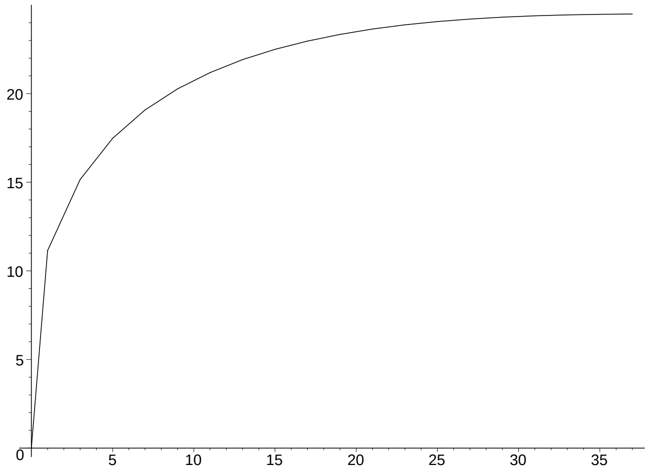

Convergence plot to ps-file:

```
> origdev:=interface(plotdevice):
  plotsetup(
  `ps`,plotoutput=`ortkonvplot.ps`,plotoptions=`color,noborder`);
  plots[listplot]([seq([kiter[i,1],kiter[i,2]],i=1..nops(kiter))]);
  plotsetup(origdev);
```

Plot of solution:

```
> plot3d(w(x,y,27),x=0..a,y=0..a,axes=boxed);
```

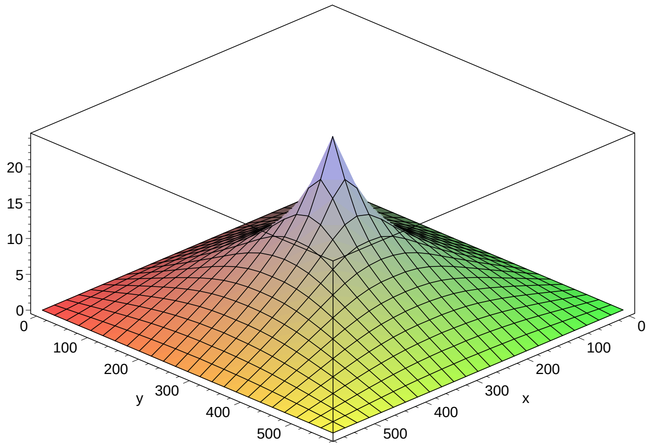

Write plot to psfile:

```
>  origdev:=interface(plotdevice):
   plotsetup(
   `ps`,plotoutput=`anaortplot.ps`,plotoptions=`color,noborder`);
   plot3d(w(x,y,27),x=0..a,y=0..a,axes=boxed);
   plotsetup(origdev);
```

Write data to file:

```
>  wf:=unapply(w(x,b/2,kiter[nops(kiter),1]),x):
   wf_list:=[seq([i,wf(i)],i=1..a)]:
   file:="P:/Mine Dokumenter/maple/anaortdef.txt":
   writeline(file,"x(mm)        w(mm)        w_b(mm)
   w_s(mm)"):fclose(file):
   writedata[APPEND](file,wf_list):fclose(file):
```

Convergence plot:

```
>  efile:="P:/Mine Dokumenter/maple/anaortkonv.txt":
   writeline(efile,"k        Deflection(mm)
   Change(%)"):fclose(efile):
   writedata[APPEND](efile,kiter):fclose(efile):
```

Appendix C

AUTODYN files

C.1 Orthotropic facings implemented in AUTODYN

```
               MATERIAL NAME: FACE

          EQUATION OF STATE: Orthotropic

          Reference density (g/cm3)  :  1.97850E+00
                 Input Type          :  Engineering
     Youngs Modulus 1 / C11 (kPa)    :  3.15000E+07
     Youngs Modulus 2 / C22 (kPa)    :  3.15000E+07
     Youngs Modulus 3 / C33 (kPa)    :  8.23000E+06
    Poissons Ratio 12 / C12          :  2.00000E-01
    Poissons Ratio 23 / C23          :  2.00000E-01
    Poissons Ratio 31 / C31          :  2.00000E-01
           Shear Modulus 12 (kPa)    :  6.00000E+06
           Shear Modulus 23 (kPa)    :  5.14360E+06
           Shear Modulus 31 (kPa)    :  5.14360E+06
       Material Axes Option          :  X-Y-Z space
    Rotation angle about 11          :  0.00000E+00
X-coord. for dirn. 11 (XYZ) (mm)     :  1.00000E+00
Y-coord. for dirn. 11 (XYZ) (mm)     :  0.00000E+00
Z-coord. for dirn. 11 (XYZ) (mm)     :  0.00000E+00
      Reference Temperature (K)      :  0.00000E+00
       Specific Heat (C.V.) (J/kgK)  :  0.00000E+00
                  Solid EOS          :  Linear

             STRENGTH MODEL: Elastic

              FAILURE MODEL: Mat.Stress/Strain

  Tensile Failure Stress 11 (kPa)    :  4.82000E+05
  Tensile Failure Stress 22 (kPa)    :  4.82000E+05
  Tensile Failure Stress 33 (kPa)    :  6.50000E+04
    Maximum Shear Stress 12 (kPa)    :  5.59000E+04
    Maximum Shear Stress 23 (kPa)    :  3.00000E+04
    Maximum Shear Stress 31 (kPa)    :  3.00000E+04
  Tensile Failure Strain 11          :  2.20000E-02
  Tensile Failure Strain 22          :  2.20000E-02
  Tensile Failure Strain 33          :  3.87000E-02
    Maximum Shear Strain 12          :  4.00000E-02
    Maximum Shear Strain 23          :  4.00000E-02
```

```
      Maximum Shear Strain 31          :  4.00000E-02
        Post Failure Response          :  Orthotropic
        Fail 11, Failure Mode          :  11 only
        Fail 22, Failure Mode          :  22 only
        Fail 33, Failure Mode          :  33 only
        Fail 12, Failure Mode          :  12 & 11 only
        Fail 23, Failure Mode          :  23 & 11 only
        Fail 31, Failure Mode          :  31 & 11 only
  Residual Shear Stiff. Frac.          :  2.00000E-01
   Max. Residual Shear Stress (kPa)    :  2.80000E+04
    Decomposition Temperature (K)      :  1.01000E+20
      Matrix Melt Temperature (K)      :  1.01000E+20
     Matrix Melt Failure Mode          :  Bulk

                EROSION MODEL: None
```

C.2 Isotropic core implemented in AUTODYN using Von Mises strength model

```
                MATERIAL NAME: CORE


            EQUATION OF STATE: Linear

            Reference density (g/cm3)  :  8.00000E-02
                 Bulk Modulus (kPa)    :  7.57778E+04
        Reference Temperature (K)      :  0.00000E+00
         Specific Heat (C.V.) (J/kgK)  :  0.00000E+00


               STRENGTH MODEL: Vonmises / Johnson-Cook / Piecewise linear


                FAILURE MODEL: Principal Stress

       Tensile Failure Stress (kPa)    :  2.20000E+03
         Maximum Shear Stress (kPa)    :  1.00000E+03
          Crack Softening, Gf (J/m2)   :  0.00000E+00
                      or, Kc2 (mN2/mm3):  0.00000E+00


                EROSION MODEL: None




               STRENGTH MODEL: Vonmises

                Shear Modulus (kPa)    :  3.10000E+04
                 Yield Stress (kPa)    :  1.20000E+03


               STRENGTH MODEL: Johnson-Cook

                Shear Modulus (kPa)    :  3.10000E+04
                 Yield Stress (kPa)    :  6.00000E+02
```

```
        Hardening Constant (kPa)    :  3.75000E+02
        Hardening Exponent          :  2.50000E-01
      Strain Rate Constant          :  0.00000E+00
Thermal Softening Exponent          :  0.00000E+00
       Melting Temperature (K)      :  4.00000E+02


            STRENGTH MODEL: Piecewise Linear

             Shear Modulus (kPa)    :  3.10000E+04
Yield Stress (zero strain) (kPa)    :  1.00000E+03
          Eff.Pl.Strain #1          :  0.00000E+00
          Eff.Pl.Strain #2          :  1.50000E+01
          Eff.Pl.Strain #3          :  0.00000E+00
          Eff.Pl.Strain #4          :  0.00000E+00
          Eff.Pl.Strain #5          :  0.00000E+00
          Eff.Pl.Strain #6          :  0.00000E+00
          Eff.Pl.Strain #7          :  0.00000E+00
          Eff.Pl.Strain #8          :  0.00000E+00
          Eff.Pl.Strain #9          :  0.00000E+00
         Eff.Pl.Strain #10          :  0.00000E+00
           Yield Stress #1 (kPa)    :  1.00000E+03
           Yield Stress #2 (kPa)    :  1.40200E+03
           Yield Stress #3 (kPa)    :  0.00000E+00
           Yield Stress #4 (kPa)    :  0.00000E+00
           Yield Stress #5 (kPa)    :  0.00000E+00
           Yield Stress #6 (kPa)    :  0.00000E+00
           Yield Stress #7 (kPa)    :  0.00000E+00
           Yield Stress #8 (kPa)    :  0.00000E+00
           Yield Stress #9 (kPa)    :  0.00000E+00
          Yield Stress #10 (kPa)    :  0.00000E+00
      Strain Rate Constant          :  0.00000E+00
Thermal Softening Exponent          :  0.00000E+00
       Melting Temperature (K)      :  4.00000E+02
```